Clemson University
TigerPrints

All Dissertations | Dissertations

5-2012

Highly charged ion interactions with ultrathin dielectric films

Russell Lake
Clemson University, rlake@g.clemson.edu

Follow this and additional works at: https://tigerprints.clemson.edu/all_dissertations

Part of the Condensed Matter Physics Commons

Recommended Citation

Lake, Russell, "Highly charged ion interactions with ultrathin dielectric films" (2012). *All Dissertations*. 951.
https://tigerprints.clemson.edu/all_dissertations/951

This Dissertation is brought to you for free and open access by the Dissertations at TigerPrints. It has been accepted for inclusion in All Dissertations by an authorized administrator of TigerPrints. For more information, please contact kokeefe@clemson.edu.

Interaction of highly charged ions with ultrathin dielectric films

---

A Dissertation
Presented to
the Graduate School of
Clemson University

In Partial Fulfillment
of the Requirements for the Degree
Doctor of Philosophy
Physics

---

by
Russell E. Lake
May 2012

Accepted by:
Dr. Chad E. Sosolik, Committee Chair
Dr. William R. Harrell
Dr. Domnita C. Marinescu
Dr. Joshua M. Pomeroy

Abstract

The excitations occurring at a solid surface due to slow highly charged ion (HCI) impacts are interesting from the perspective of fundamental processes in atomic collisions and materials science. This thesis focuses on two questions: 1) How much HCI potential energy deposition is required to form permanent surface modifications?, 2) How does the presence of a thin dielectric surface film change the classical over-the-barrier picture for neutralization above a clean metal?

I describe a measurement of craters in thin dielectric films formed by Xe^{Q+} $(26 \leq Q \leq 44)$ projectiles. Tunnel junction devices with ion-irradiated barriers were used to amplify the effect of charge-dependent cratering through the exponential dependence of tunneling conductance on barrier thickness. Electrical conductance of a crater $\sigma_c(Q)$ increased by four orders of magnitude (7.9×10^{-4} μS to 6.1 μS) as Q increased, corresponding to crater depths ranging from 2 Å to 11 Å. According to a heated spike model, the energy required to produce the craters spans from 8 keV to 25 keV over the investigated charge states. Considering energy from pre-equilibrium nuclear and electronic stopping as well as neutralization, we find that at least $(27 \pm 2)\%$ of available projectile neutralization energy is deposited into the thin film during impact.

Additionally, an extension of the classical over-barrier model for HCI neu-

tralization above dielectric covered metal surfaces is presented. The model is used to obtain the critical distance for the onset of neutralization above C_{60}/Au(111), Al_2O_3/ Co, and LiF/Au(111) targets. The model predicts that for thin films with low electrical permittivity and positive electron affinity, the onset of neutralization can begin with the electrons in the metal, and at further ion-surface distances than for clean metals. The model describes three distinct over-the-barrier regimes of "vacuum limited" capture from the metal, "thin film" limited capture from the metal, and capture from the insulator. These regimes are detailed in terms of charge state, target material parameters and film thickness.

Acknowledgments

In 2004 Jim McLean introduced me to Chad Sosolik and his emerging research group while I was an undergraduate student at State University of New York at Geneseo. A NSF-REU grant provided a means of working in Clemson that summer. The summer job ultimately led to a 8 year scientific collaboration with Chad, and the work in this thesis. I sincerely appreciate everything Chad has done to help me start my career. I look forward to results from the Clemson EBIT and hope that the work presented here provides some starting point for the future experiments.

Thanks also goes to the current and former members of the Clemson group. In particular I would like to acknowledge the first PhD graduate, Matt Ray, for being an all-around great colleague. I have also really enjoyed working in the lab and having extra-scientific discussions with Jason Puls.

In the middle of my graduate school tenure I uprooted from Clemson and began work with Josh Pomeroy at NIST-Gaithersburg. Upon moving to Maryland I found temporary housing in the windowless basement of a French-speaking family in Bethesda. Needless to say, I experienced an initial culture shock both at home and in the lab. Even though I was Josh's first PhD student (*de facto*), he rose very well to the challenge of being a co-advisor. I am proud of what we have accomplished over the last three years. Josh's work ethic and do-it-yourself

attitude set an excellent example as I move forward to new projects.

I would also like to thank Neil Zimmerman at NIST. His Socratic method of "questioning" during our weekly team meetings taught me important lessons about communicating science, and communicating information clearly in general. I have had good luck to interact with smart and clever people in the Physics Lab (PML) on a daily basis including Sam Brewer, Kevin Dwyer, Panu Koppinen, Stew Stewart and Ted Thorbeck. I look forward to hiking in the forests of Finland with Panu and Niina and will certainly need Panu's expert advice on fabrication and electrical measurements at my postdoctoral position in Helsinki.

I also need to acknowledge my family for emotional support, financial bailouts, and accepting the idea that I needed to move far away to upstate South Carolina for a several years in order to accomplish my educational goals. Clearly, the work in this thesis would not have been possible without their help.

I gratefully acknowledge financial support along the way from NSF, NIST, Clemson University COMSET, and ORAU.

Finally, thank you to my committee members Chad, Josh, Rod and Catalina for careful review of this thesis.

Table of Contents

Title Page i

Abstract ii

Acknowledgments iv

List of Tables viii

List of Figures ix

1 Introduction **1**
1.1 Ion - surface interactions 1
1.2 Objectives 7
1.3 Outline 7

2 Fabricating tunnel junctions in ultra-high vacuum **9**
2.1 Context 9
2.2 Experimental apparatus 12
2.3 Plasma characteristics 27
2.4 Device characteristics 34
2.5 Modeling the tunneling resistance 42
2.6 Chapter summary 54

3 Measuring charge dependent HCI energy deposition with tunnel junctions **57**
3.1 Overview 57
3.2 Experiment 58
3.3 Data 64
3.4 Analysis 72
3.5 Results 78
3.6 Discussion 84
3.7 Chapter Summary 105

4 Classical over-the-barrier model for neutralization of highly charged ions above thin dielectric films . . . 108
4.1 Introduction . . . 108
4.2 Bulk targets . . . 111
4.3 Dielectric thin films on metals . . . 113
4.4 Comparison with experiment . . . 137
4.5 Summary . . . 148

5 Conclusions . . . 151
5.1 Summary of results . . . 151

6 Proposals for future experiments . . . 155
6.1 Calorimetry . . . 155
6.2 Measurement of pre-equilibrium stopping with tunnel junctions . . . 157

Appendices . . . 158
A Plasma Chamber . . . 159
B Measuring light intensity of the discharge with the photodiode . . . 163
C Resistance of a tunnel junction during warm up (77 K to 300 K) . . . 166
D Fitting a micrograph line profile . . . 167
E Data analysis . . . 169
F Potential definitions and algorithms for calculating R_c' . . . 173
G Atomic units . . . 187

References . . . 189

List of Tables

2.1 Electron beam evaporation parameters. 18
2.2 Quartz crystal monitor settings. 18
2.3 Parameters of I-V fits shown in Fig. 2.13 47
2.4 Parameters of I-V fits shown in Fig. 2.15 (Al dusting layer). 54

4.1 Summary of critical distances at $Q = 36$ and $s = 1$ nm for three experimentally studied systems [1, 2, 3, 4]. 149

1 "Negative resistance" correction for 3, 13, 14. Unirradiated control devices are shaded. 170
2 Error propagation for the dose N on chips 3, 13, 14. 171
3 Error propagation for σ_c. 172
4 Relationship between selected atomic units, fundamental constants and SI units from Ref. [5] 188

List of Figures

1.1 Schematic representation of a slow HCI impact on a surface. 3

2.1 Schematic of UHV chamber system. 13
2.2 First generation shadow masks. 21
2.3 Photograph and micrograph of G1 device. 22
2.4 Second generation mask set. 24
2.5 Micrograph of a G2 device 25
2.6 Photovoltage at the beginning and end of a plasma discharge. 29
2.7 Optical emission from three plasmas for current set points 30 mA, 40 mA and 50 mA. 30
2.8 Photovoltage and impedance of the plasma. 31
2.9 Voltage contour plots demonstrating the "negative resistance" artifact 37
2.10 Relative uncorrected four-point resistance error as a function of RA . 39
2.11 Resistance as a function of plasma oxidation time. 41
2.12 The asymmetric barrier tunneling model (from Ref. [6]) 44
2.13 dI/dV as a function of bias voltage. 48
2.14 Thicknesses (a) and barrier heights (b) extracted from fits to dI/dV curves in Fig. 2.13. 50
2.15 Comparison between pristine junction and junctions with a dusting layer. The position of the conductance minimum is indicated on each curve 55

3.1 EBIT beamline schematic (from Ref. [7]) 59
3.2 Beam current as a function of analyzing magnet field. 61
3.3 Schematic of HCI neutralization scenario and $G(N)$ data. 67
3.4 dI/dV curves for both irradiated and unirradiated devices. 68
3.5 Statistical model for the number of distict features. 71
3.6 $\sigma_c(Q)$ increases by four orders of magnitude for charge states between $Q = 26$ and $Q = 44$. 72
3.7 On-chip resistance pattern and correction. 76
3.8 Charge dependent crater depths. 82
3.9 Comparison with sputter yield from Ref. [8] 84
3.10 Ionization and neutralization energies for Xe. Electron shells are indicated. 89

3.11 Exponential model for charge state equilibration. 93
3.12 Total Xe neutralization energy and neutralization energy dissipated within the 14 Å film. 94
3.13 SRIM calculated nuclear (red) and electronic (black) kinetic energy loss rates for Xe^{1+} on Al_2O_3. 95
3.14 Effective charge squared as a function of Q. 98
3.15 Crater formation energies from the heated spike model. 102
3.16 Device conductance as a function of ion dose for samples `111222-4` and `111222-14` (G2 devices). 106

4.1 Two- and one-dimensional profiles for a HCI outside a metal. 114
4.2 Point charge representation of an electron within metal/dielectric/vacuum and the energy profile along z for $R > 50$ nm. 116
4.3 Permittivity dependence of the potential due to the ion and its image (no self image) 119
4.4 Potential profiles in the metal/dielectric/vacuum as the ion approaches the target (regime ii). 125
4.5 Permittivity dependence of the barrier ϕ within the film 128
4.6 $R_c'(\epsilon)$ for $Q = 36$ at thickness $s = 3.2$ nm 129
4.7 (a) $R_c'(s)$ for $Q = 9$, 24, 36 and 54 outside C_{60}/Au(111) and (b) permittivity dependence of $R_c'(s)$ at $Q = 24$. 131
4.8 Potential plots at R_c' for charge states $Q = 9, 24, 54$ in regimes iii, ii, and i respectively. 134
4.9 $R_c'(s)$ dependence on metal work function. 136
4.10 Comparison between the model and experiment in Ref. [4]. 138
4.11 $R_c'(s)$ in regimes i and ii for $Q = 9$, 24, 36 and 54 for a C_{60}/Au(111) target. 140
4.12 $R_c'(s)$ for $Q = 7$ outside LiF/Au(111). 145
4.13 Thickness dependent critical distances for $Q = 44$ interacting with Al_2O_3 films on Co. 147

1 Sideview of the plasma chamber. 159
2 Top cluster flange of the plasma chamber. 160
3 Plasma chamber through the 6″ viewport. 161
4 Schematic drawing of the bottom flange, bottom electrode and sled assembly. 162
5 Specifications for wavelength dependent responsivity of the ThorLabs `SM1PD1B` photodiode (from the datasheet). 164
6 Photograph of an oxygen discharge at I_{set} = 40 mA, 120 mTorr, with negative bias on top electrode. 165
7 Resistance as a function of temperature for a tunnel juntion (sample `090225-14D`) 166
8 Micrograph line profile. 168

Chapter 1

Introduction

1.1 Ion - surface interactions

The interaction of atoms and ions with solids plays an important role in both fundamental science and technology. A wide variety of physical phenomena can be observed when atoms and ions impinge on a surface. These phenomena range from quantum mechanical diffraction effects at thermal energies of a few meV [9], up to track formation via atomic displacements at high energies of MeV [10]. At all energies, ion-surface interactions are inherently complex due to the many-body nature of a solid state target. To model the complexity of ion-surface interactions, a common general approach is to consider the target as being composed of two distinct but coupled systems of *nuclei* and *electrons*.

Ion-surface collisions are almost always accompanied by inelastic processes (*e.g.*, charge exchange or excitation of the target/projectile). These processes occur, in part, due to the potential energy associated with the ionization energy required to strip their electrons. It has been known since the 1920s that this potential energy can manifest itself in inelastic excitations during an ion-surface interaction [11, 12]

including enhanced electron emission (potential emission). Hagstrum's work in the 1950s laid the foundation [13] for the contemporary theoretical description of charge exchange mechanisms that occur via Auger processes [14]. Since then, considerable progress has been made toward quantitative understanding of charge transfer in ion-surface interactions (see reviews in Refs. [15, 16, 17]).

In this thesis, the focus is on highly charged ion (HCI) interactions with solids in the so-called low energy regime where kinetic energies are of order 100 keV. HCIs of these velocities are often referred to as "slow" in the literature where slow is defined as projectile velocities less than a Bohr velocity: $v_p < 2.19 \times 10^6$ m/s (or kinetic energies less than 25 keV/u) [8, 18]. In this velocity regime, the timescale for electron motion is short compared to the timescale for ion motion. This provides time for above-surface electron capture and relaxation processes, and means that the ion will neutralize rapidly near the surface. This is in contrast to swift heavy ions where neutralization occurs over much longer length scales, within a solid [19, 20]. General reviews of slow highly charged ion-surface interactions have been given by Arnau, *et. al.*, [18], Schneider, *et. al.*, [21], Schenkel. *et. al.*, [8], and H. P. Winter, *et. al.*, [22].

A dramatic increase in the initial charge state of an impinging ion opens up many new pathways for inelastic energy transfer. The electronic potential energy is the *neutralization energy* defined as the sum of the binding energies of the electrons removed during ionization. For example, Xe^{44+} releases 51 keV of potential energy upon neutralization at a surface and this energy is available for inducing a variety of inelastic processes at the surface. This includes the formation of irreversible surface modifications even at low kinetic energies. Neutralization energy is deposited into a nanometer-scale area in <100 fs, creating an interaction with power density of order 10^{17} W/m^2.

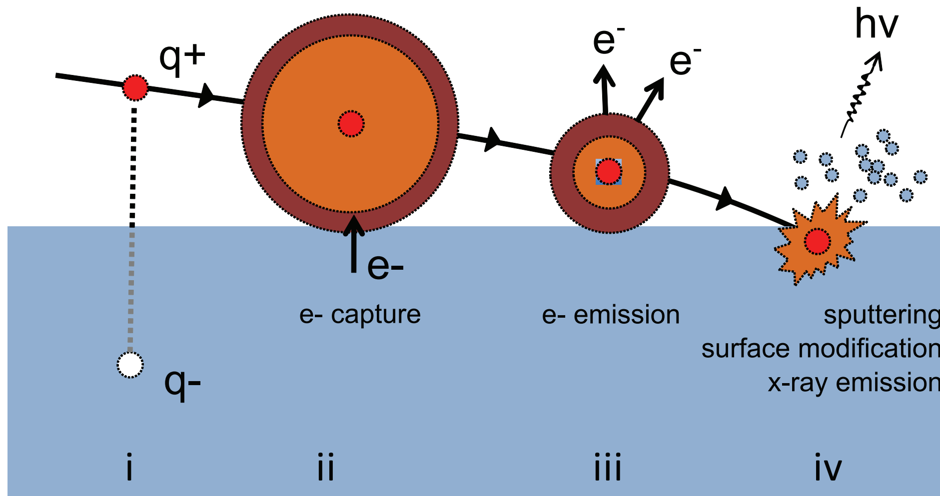

Figure 1.1: Schematic representation of a slow HCI impact on a surface: (i) The HCI induces a dielectric response in the target. (ii) formation of the "hollow atom" by electron capture into excited states, (iii) the hollow atom is screened by the target e^- gas, (iv) below-surface relaxation.

The general neutralization scenario is depicted in Fig. 1.1 and is summarized in Ref. [22]. Stages (i) and (ii) represent the neutralization scenario described by the classical over-the-barrier model [23]. In Fig. 1.1 (i), the ion induces a dielectric response in the target, and gains kinetic energy from image acceleration. At a critical distance for the onset of neutralization, the ion captures multiple electrons resonantly into high-n Rydberg states to form a neutral "hollow atom"(ii) [24]. Above the surface, electrons in Rydberg states electrons relax to fill inner-shell vacancies and emit Auger electrons. As the ion comes in close proximity with the electrons in the target, the remaining excited electrons will be screened and "peeled off"(iii) [23, 25], leading to re-ionization and formation of a sub-surface hollow atom. In the final stage of neutralization, efficiency of the energy relaxation process from photons becomes comparable to that of Auger relaxation (iv)

[24]. For insulator targets, the neutralization process leads to potential energy induced sputtering, and the formation of permanent material defects.

At this point, there is no general picture of the excitation and modification of a material induced by HCIs [26]. An important step toward developing such a picture is to quantify the amount of potential energy deposited into the material as opposed to the amount re-radiated into the vacuum. Schenkel and co-workers have reported that as much as 40 % of the neutralization energy from Xe^{52+} projectiles is delivered into a Si detector target [27], where the remainder is emitted to the vacuum through Auger electrons and photons. The experiments described in this thesis were designed to study the surface modifications that result from HCI impacts, with particular emphasis on a quantitative assessment of the potential energy that goes into surface modification. Within this ≈ 40 % of deposited neutralization energy, there is a smaller fraction that plays a direct role in defect formation [1]. In Ch. 3 we describe an experiment using tunnel junctions with HCI irradiated barriers to measure this quantity.

The amount of energy deposited into a solid during an ion surface interaction is of particular importance in practical applications. Sputter damage from singly charged ions, for example, is governed by kinetic energy loss to target nuclei and electrons along the ion's path [28]. Accurately predicting this loss channel, which can be achieved over a wide incident energy range through semi-empirical models [29], is a key input for many ion-based processing techniques, such as ion milling, ion track formation/etching, lithography, and implantation [28, 30, 31].

For HCIs, there is no such framework with which to predict inelastic energy deposition for a given projectile and material. The role of neutralization energy in surface modification is poorly understood when compared to defect

formation through kinetic energy loss. The ability to harness this pathway in materials processing [32, 33] and mitigate its role in important erosion processes such as in fusion reactors [34] requires charge state dependent measurements of energy deposition into a material. Additionally, (as will be discussed in Ch. 3) increasing the projectile charge state also enhances the kinetic energy loss to the target material during electronic equilibration [35, 36].

A number of systematic investigations of HCI induced nanofeatures have been performed with scanning probe microscopy (SPM). The general approach is to irradiate a sample with HCIs and subsequently measure surface topography with AFM or STM. HCIs induce individual permanent nanoscale surface modifications on materials including Au, HOPG, Si, KBr, CaF_2, BaF_2, TiO_2, PMMA, mica and LiF [37](and references therein). The density of surface features typically corresponds to the flux density of the HCI beam, *i.e.* each ion forms a single nanofeature. A variety of nanofeature geometries emerge in the topographic measurements including raised "hillock" structures and lowered "pits" or "craters".

One challenge while performing a SPM based study of nanofeature sizes is acquiring good statistics. In practice, scanning probe measurements require topographic data to be acquired in a single scan frame at a time. The standard deviation of the mean nanofeature size decreases as $1/\sqrt{n}$ where n is the number of measurements [38]. To establish the standard deviation of the mean nanofeature size within 1 % of the statistical uncertainty of an individual measurement, at least $n \approx 10^4$ measurements are required. This means that hundreds of scanning probe micrographs are needed to locate and measure the sizes of the members in a sufficiently large ensemble of HCI induced nanofeatures. Also, due to the statistical nature of ion irradiation, there is an inherent width to the histogram of nanofeature sizes.

The fact that SPM studies measure nanofeatures one scan frame at a time may also pose a problem when considering time dependent surface relaxation processes. Nanofeatures measured immediately after irradiation will have had less time to undergo coarsening than a nanofeature measured in later scans. In this way, time-dependent surface processes may distort the statistical distribution of measured nanofeature sizes. For Au(111), the timescale for observable surface coarsening of HCI induced nanofeatures can be measured in hours at room temperature, even in ultra high vacuum [39]. For insulators, the timescale for coarsening may be longer. However, the observed defect agglomerations formed by ion impacts [40, 41] are clearly not in their lowest structural energy configuration, and will relax in time due to thermal energy.

Another practical challenge present in scanning probe studies is to measure nanofeature sizes with high accuracy. If the radius of a nanofeature is comparable to the tip radius, sample-tip convolution effects can increase the apparent width of the feature (*e.g.*, [42, 43]). This challenge can be overcome on crystalline targets where the defect size in a scan can be directly compared to periodic lattice structure of an unirradiated region of the sample. Another possibility is to fabricate (and characterize) atomically sharp tips with a higher aspect ratio than the nanofeature of interest.

Our measurements of HCI induced nanofeatures within tunnel junctions were motivated, in part, by the challenges associated with the scanning probe based measurements. As will be described in Ch. 3, tunnel junctions allow the simultaneous measurement of a large number of HCI induced modifications with a single conductance measurement of a tunnel junction. After a tunnel barrier is irradiated with HCIs, depositing the top electrode onto the irradiated interface stops time-dependent surface processes [1]. Within the tunnel junction, all of the

HCI induced modifications experience the same history between irradiation and measurement. In addition to changes in surface topography, tunnel junctions can also detect modifications formed within the barrier. Electrical measurements of tunnel junctions are sensitive to both spatial and electronic properties through the entire thickness of the barrier.

1.2 Objectives

The two primary questions that will be addressed in this thesis can be summarized as follows:

1. What fraction of deposited HCI potential energy goes into the formation of a permanent material defect?
2. What effect does placing a thin dielectric film on a metal target have on the initial charge transfer between the target and ion?

1.3 Outline

- Chapter 2: Fabrication process for tunnel junction devices used to measure HCI induced surface modifications is described with special emphasis on Al_2O_3 barrier formation by plasma oxidation. Measurement techniques and tunneling models are introduced. Tunneling conductance (dI/dV) data are presented and analyzed.
- Chapter 3: Results are presented on a measurement of HCI induced "craters" embedded within tunnel junctions [1]. Charge-dependent crater depths are

extracted and analyzed with a heated spike model. The concepts of potential energy deposition and pre-equilibrium kinetic energy loss are discussed.

- Chapter 4: A model for the onset of neutralization for HCIs above metals covered with thin dielectric films is described. The model is constructed by extending the classical over-the-barrier model for above-surface neutralization, using classical potentials. Comparisons to the experimental systems Al_2O_3/Co, C_{60}/Au(111) and LiF/Au(111) are presented.

- Chapter 5: A summary of the main scientific results is presented.

- Chapter 6: Finally, two experimental proposals are mentioned. These include a high precision calorimetry experiment and a measurement of pre-equilibrium stopping using tunnel junctions.

Chapter 2

Fabricating tunnel junctions in ultra-high vacuum

2.1 Context

A tunnel junction is an electronic device with a non-linear current-voltage characteristic where the dominant transport mechanism through the device is quantum tunneling [44]. One way to realize a tunnel junction device is to sandwich a thin dielectric film between two conducting electrodes. The thin dielectric film introduces a potential barrier between electrons in the "top" and "bottom" electrodes. The measured resistance of this device depends sensitively on both the height and width of the potential barrier formed by the dielectric. These properties are determined by the film thickness and band gap. Small changes in either of these quantities can be detected through electrical measurements of a device. The sensitivity of tunneling resistance to the barrier height and width is used in a wide variety of tunneling spectroscopy techniques, including scanning tunneling microscopy and inelastic electron tunneling spectroscopy [44].

For the experiments described in this thesis, we exploit the fact that dielectric materials are susceptible to potential sputtering and surface modifications during HCI irradiation, due to their low free electron density [32]. This means that the electrical measurements of tunnel junctions with HCI irradiated barriers can probe the surface modifications formed during irradiation. Additionally, because the tunnel barriers are thin compared to the charge equilibration length of a slow HCI, the modifications are formed during the pre-equilibrium stage of HCI relaxation [45].

The application of tunnel junctions as sensors of ion induced surface modifications is relatively new and complements previous measurements of surface modification [1, 46, 47, 48, 49]. Studying material modification induced by HCIs with tunnel junctions presents practical challenges involved with completing microelectronic device fabrication in surface science chambers. One goal of the study was to grow and irradiate tunnel junctions entirely within ultra-high vacuum (UHV) to avoid contamination of the surface. Within the chambers, it is possible to keep a surface "clean" throughout the fabrication steps described here. For example, given a base pressure of 10^{-11} Torr, the time required for a monolayer of air to condense on the surface at room temperature is about 69 hours, based on the Langmuir formula, assuming a unity sticking probability [50]. After the barrier is formed, a tunnel junction can be irradiated and finished within less than 30 hours. Statistically, this means that the majority of defects will never be exposed to any reactive species.

The devices described here have magnetic electrodes where the tunneling occurs through $Co/Al_2O_3/Co$ layers. Details of the unirradiated devices are discussed in this chapter and the fabrication steps can be briefly summarized as follows. Each tunnel junction device was grown on an oxidized silicon substrate

with the layer structure (in nm): bottom contact and antiferromagnet pinned layer [2 Co + Ox / 21 Co], tunnel barrier [1.1 Al + Ox], magnetic free layer and top contact [10 Co / 40 Cu / 3 Au]. Slight variations from this layer structure, will be noted in the text as they occur. All layers were deposited by electron beam evaporation where +Ox indicates exposure to oxygen plasma after growth. Shadow masks were used to define the sizes and positions of the thin film electrodes.

For the tunnel junctions with HCI modified barriers, irradations were performed *in situ* before deposition of the top layer, [10 Co / 40 Cu / 3 Au]. Once devices with irradiated barriers have been completed, by the deposition of a top electrode, they can be removed from the vacuum chamber and measured. The defects are encapsulated in the metal from the top electrode, and are physically and chemically stable on the timescale of years [49]. Details of the HCI irradiation step and measurement of irradiated devices is reserved for Ch. 3.

This chapter gives an overview of the experimental apparatuses and the process for growing tunnel junctions used in this experiment. Here we overview sample preparation, formation of the device layer structure and the resistance measurements. The final resistance of a tunnel junction depends critically on the parameters of the plasma oxidation step. At the end of the chapter dI/dV measurements are shown as a function of oxidation time. Additionally, dI/dV data are fit with a WKB tunneling model, to show how barrier height and width evolve with oxidation time. In the final section, an oxidation scenario consistent with the fits to our dI/dV measurements is proposed.

2.1.1 Constraints

An original purpose for studying HCI modified tunnel junctions was to investigate the possibility of using potential sputtering [32] to trim the resistance-area (RA) product of magnetic tunnel junctions [33]. These studies were motivated by the desire to decrease the RA product within a device demonstrating tunneling magnetoresistance as a path to improve hard drive read head technology.

While the experiments in this thesis focus on measuring ion energy deposition instead of the technological applications, we have maintained the same layer structure of the devices from the previous work. Specifically, the tunnel junctions described here are magnetic tunnel junctions, grown by electron beam evaporation, in crossed-wire geometry. The electrical measurements presented below were taken with no applied magnetic fields.

When fabricating devices for the experiment, reproducibility of device resistance is critical. Random resistance fluctuations from device to device in the unirradiated control devices need to be be smaller than measurable resistance changes due to the HCI impacts. Systematic effects that affect device resistance, such as variation of device area on a single chip, can be corrected.

2.2 Experimental apparatus

Fabricating devices in UHV is incompatible with high-throughput processing techniques that would normally take place in a clean room. Instead, devices need to be grown in an environment compatible with UHV (surface science) chambers. This requires integrating the deposition, oxidation and target chamber

setups into a single system. Samples must be moved between the vacuum chambers by magnetically coupled transfer rods and the sample size is constrained by the diameter of the ports connecting the chambers. This means many of the process steps are completed one chip at a time, as opposed to fabricating many junctions simultaneously on a wafer.

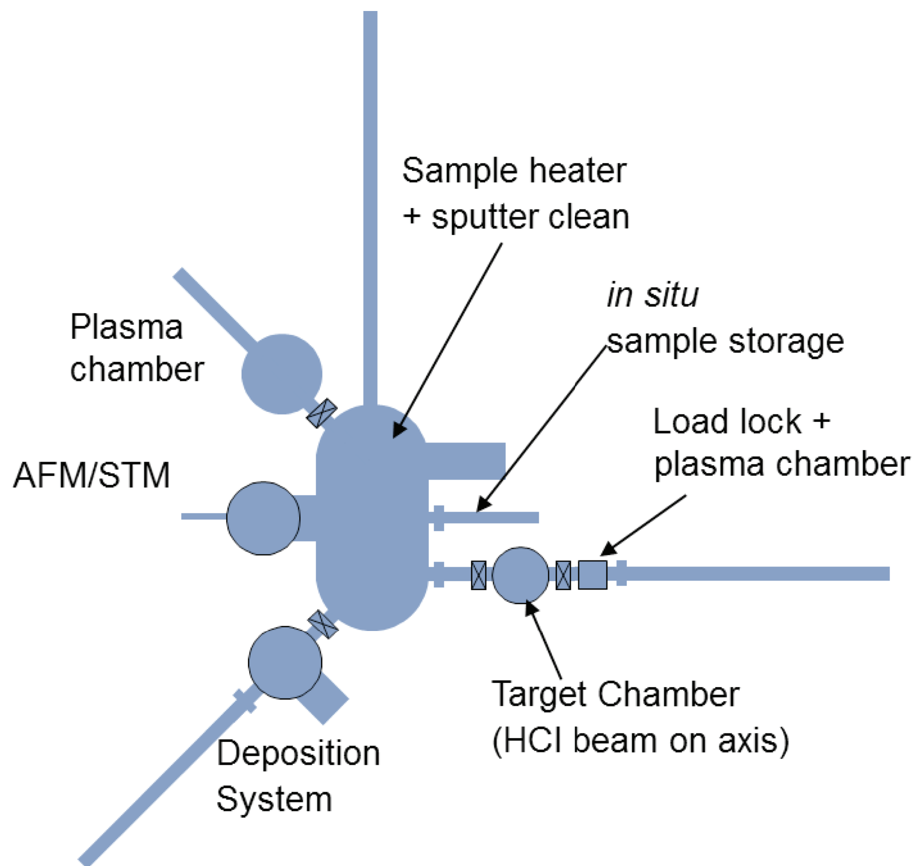

Figure 2.1: Schematic of UHV chamber system

The experiments were conducted within a network of connected UHV chambers, so that materials could be grown and irradiated *in situ* (schematic top view shown in Fig. 2.1). Samples are introduced in the load lock (LL) through a

hatch with a Viton o-ring seal. Once samples are loaded into one of four positions on the sample sled on the magnetic transfer rod in the load lock the chamber can be pumped out via a small turbo pump to a typical base pressure of 10^{-8} Torr. The LL is equipped with an electrical feedthrough and mesh so that one sample at a time can be cleaned with oxygen plasma.

The LL opens directly to the target chamber (TC) where samples can be exposed to beams of highly charged ions from the EBIT beamline. The TC is evacuated with an ion and Ti sublimation pumps. For beam analysis, the TC is equiped with a Faraday cup, and microchannel plate beam viewer. Base pressure of the TC is typically 10^{-10} Torr.

To the left of the TC in Fig. 2.1 is the main chamber. The main chamber houses a STM/AFM (not used in these experiments) as well as a resistive sample heater, sputter gun, residual gas analyzer, e- beam heater, sputter gun and magnetic transfer rod with 12 slots to store samples. The main chamber is kept at base pressure 10^{-10} Torr using a turbo pump (Varian TV551), ion pump and titanium sublimation pump.

The deposition chamber has a 3 kW electron beam evaporator, with 5 pockets for evaporant materials (Thermionics Inc.). The chamber has feedthroughs for liquid nitrogen cooling of a metal shroud above the sources, chilled water for regulating the e- gun hearth temperature, and thermocouples for monitoring temperature of the shroud. A deposition monitor, consisting of a commercial quartz crystal microbalance (QCM) is mounted above the sources. The QCM measures the thickness of material deposited onto the surface of the quartz crystal. A pneumatic shutter (controlled by set points on the QCM controller) opens/shuts the opening in the shroud between the sample and evaporation source. A magnetic transfer rod holds a single chip above the evaporation source for growth of thin

film samples. The distance between the source and chip is about 20 cm. A linear feedthrough for shadow masks enters the deposition chamber at the same height, but parallel to the magnetic transfer rod that holds the samples (not shown in Fig. 2.1).

2.2.1 Sample preparation

The samples consisted of rectangular pieces of oxidized silicon with dimensions 13 mm x 20 mm and total thickness of 0.5 mm. The chips were diced from 100 mm wafers, where one wafer yielded 24 chips (four of the chips have slightly chamfered corners). The samples discussed here were lightly p-doped with approximately 100 nm of thermally grown oxide. The doping level, doping type, and oxide thickness of the substrates are not critical. The primary purpose of the oxidized silicon is to provide a flat and electrically insulating substrate for the device layers. The chips were sonicated in distilled water for at least 10 hours after dicing, to remove dust or dirt from the dicing process. After being removed from the distilled water bath, a chip was dried off with pressurized nitrogen gas and mounted to a 12 mm wide stainless steel rectangular platen (by Omicron GmbH), with colloidal silver (by EBS Inc.). The chips were then baked in an oven at approximately 150°C overnight to allow the solvent in the colloidal silver to evaporate. Typically, four chips were mounted and baked simultaneously. The chips were removed from the oven and immediately (<5 min) loaded into the four sample slots in the LL.

2.2.2 Thin film growth

Thin films were grown in the UHV deposition chamber shown at the bottom of Fig. 2.1. The deposition chamber is kept at 10^{-9} Torr with a Varian (TV301) turbo pump (pumping speed 300 L/s). One sample at a time can be brought into the deposition chamber via a magnetic transfer rod.

UHV is not normally a strict requirement for electron beam evaporation chambers. Though, for better vacuum pressures, fewer impurities will be incorporated into the thin film during growth. At 10^{-6} Torr, a monolayer of impurity atoms can form within one second, assuming a unity sticking probability [50]. This rate also affects the cleanliness of the source materials, which can absorb impurities from residual gas in the deposition chamber. In addition to preventing impurities from being incorporated into the film, the UHV deposition chamber allows us to directly transfer samples to the UHV main chamber.

The deposition chamber was equipped with a five-pocket RCL series electron beam evaporation gun by Thermionics Inc. where the evaporation sources in the hearth are translated linearly [51] . The e- gun hearth is cooled with a continuous flow of chilled (14 °C) water. Typically, the pockets were filled with Au, Cu, Co, Al and Nb metals. Solid metal pellets or shot sit within each of the five pockets in the copper evaporator hearth. Each of the pockets have nominal volume of 2 cm^3. To decrease heat transfer between the evaporant and hearth, crucible liners can be placed within the hearth. Crucible liners can provide improved uniformity and control of the deposition rate.

The power required for evaporation depends on the radiant heat loss, the latent heat of evaporation, and the conductive heat loss to the hearth. Fundamentally, the magnitudes of emission current needed for evaporation (shown in

Table 2.1) are governed by the temperature where evaporation exceeds the radiation and conductive losses. Electron beam power required to meet this level was empirically determined, by monitoring evaporation rate as a function of electron beam power. At a critical temperature, the vapor pressure of the source increases and the source metal evaporates. Table 2.1 includes the temperature at which the evaporant material has a vapor pressure greater than 0.1 mTorr [52, 53].

Cobalt can be evaporated efficiently even without a crucible liner. Typical conditions for evaporation of Co are P = 50 mA $\times$ 5.36 kV (Table 2.1). The power required to evaporate aluminum can be reduced by placing an alumina disk between the evaporant and hearth. The disk reduces conductive heat losses to the hearth, and enhances evaporation rate. Similarly, gold and copper are placed within carbon (FireRite^{TM}) crucible liners, to limit conductive heat losses and reduce the electron beam power needed to achieve the desired evaporation rate. Nb is a refractory metal with a high melting point, and is most easily evaporated in a BN crucible. Characteristics of e- beam evaporation of Au, Cu, Co and Al have been described in detail in the literature [52, 53].

The deposition thicknesses were monitored by an Inficon XTM/2 QCM system [54]. The parameters are shown in Table 2.2. The QCM controller also controls a pneumatic shutter that can block the path between the evaporation source and sample. The primary QCM input parameters are the density of the evaporant material, z-ratio, and tooling factor. Z-ratio depends on both the density and shear modulus of the deposited film. Tooling is a geometric correction. Z-ratio for Co, Au, Al, Cu and Nb sources were set from the values given by Inficon [54]. Tooling was determined by comparing profilometry measurements of the actual film thickness (t_m) on the substrate to the thickness measured by the

Source	T_m C°	$T(p_{vap} > 0.1$ mTorr) C°	crucible liner	nominal rate Å/s @ mA	V_{HV} (kV)
Al	660	1010	Al_2O_3 disk	0.2 @ 175	-4.94
Co	1495	1200	none	0.5 @ 50	-5.36
Cu	1083	1017	C	2.0 @ 60	-5.31
Au	1064	1130	C	0.2 @ 50	-5.37
Nb	2468	2287	BN	0.1 @ 220	-4.8

Table 2.1: Electron beam evaporation parameters for Al, Co, Cu, Au and Nb [52, 53].

Source	**Z-ratio**	**ρ(g/cm^3)**	**Tooling**
Al	1.080	2.7	110%
Co	0.343	8.9	100%
Cu	0.437	8.930	100%
Au	0.381	19.30	100%
Nb	0.492	8.578	100%

Table 2.2: Quartz crystal monitor settings. Further details on Z-ratio, tooling and density are provided in Ref. [54]

QCM (t_x). Tooling is defined as:

$$Tooling(\%) = TF_i \frac{t_m}{t_x}, \tag{2.1}$$

where TF$_i$ is the initial tooling factor at the beginning of the calibration. For Co, Co, Au, and Nb tooling was set at 100 %. For an Al films, tooling was set at 110 %; the QCM is offset radially from the sample by several centimeters.

Power deposited into the evaporation source material is proportional to the current emitted from the filament as $P = I_{fil}\ V_{HV}$. However, V_{HV} from the power supply tends to drop slightly with increasing I_{fil}. The voltage output corresponding to each I_{fil} during a deposition is included as the far right column

in Table 2.1. Generally, recording the electron current emitted from the filament during the evaporation is a good metric for comparing the total power deposited into the source material from one deposition to another.

The distribution of electrons emitted from the e-gun filament determines the width of the electron beam spot size. Therefore, in order to achieve a tightly focused beam the power supply should minimize ripple. The e- gun power supply used was model 150-0040 by Thermionics Inc [51]. Slight modifications were made to the supply in order to decrease the ripple of the high voltage output. The circuit sketched in the manual was modified by replacing the resistor R109 (1 kW; 100W), with a short and by placing a 150 Ω (100 W) resistor in parallel with the control rectifier CR103.

The pneumatic shutter is opened or closed with a switch in the QCM controller that can be actuated by film thickness set points. A typical deposition was performed as follows. With the shutter closed, the e- gun filament current is increased slowly (1 mA s^{-1}) to a value of approximately 50% of the filament current used during evaporation, to warm up the source. The current was then increased to approximately the values in Table 2.1, to achieve the desired evaporation rate for a particular source material. When this evaporation rate is achieved, the shutter is opened manually via the the QCM controller. The final film thickness is set within a predefined QCM program. When the set point is reached, the shutter closes. The electron beam power is never adjusted during deposition on the sample.

The metal shroud in the deposition chamber is cooled with liquid nitrogen to regulate the deposition chamber temperature during prolonged e-beam heating of the source materials. Additionally, the nitrogen cooled shroud acts as a sorption pump for residual gases. A typical deposition chamber pressure of 5×10^{-10}

Torr is reached at shroud temperature -160°C, even when the electron beam is on. Pressure can also decrease during an evaporation, as the evaporated metal particles effectively *getter* residual gas in the chamber. This is observed mostly with the Co source, where the pressure drops by several tenths of nTorr at the onset of evaporation.

2.2.3 Shadow masks

2.2.3.1 Overview

During the course of the experiments, two designs of shadow masks were developed. The first and second generation masks will be referred to as G1 and G2 masks respectively. For both sets of masks, a cut pattern in (2.5×2.5) cm^2 sheet of metal defines the position of the crossed wire electrodes used to form either the top or bottom electrodes of the tunnel junctions. Our fabrication method is in contrast to the method of lithographically patterning devices into a layered wafer: a technique that is often performed in a clean room setting. Here, metals are evaporated through mask slits of a few hundred microns in width, to deposit material on a chip within an ultra high vacuum chamber.

2.2.3.2 First generation masks (G1)

The first generation of shadow masks produced chips with four devices. The mask patterns were electric discharge machined into stainless steel shim stock with thickness 254 μm. The mask patterns are shown in Fig. 2.2(a) and (b). A chip produced with the G1 masks is shown in Fig. 2.3(a). In the figure, the chip has dimensions 13 mm $\times$ 20 mm. The four tunnel junctions on the chip are arranged in a crossed wire geometry. The first mask defines the lead running parallel to

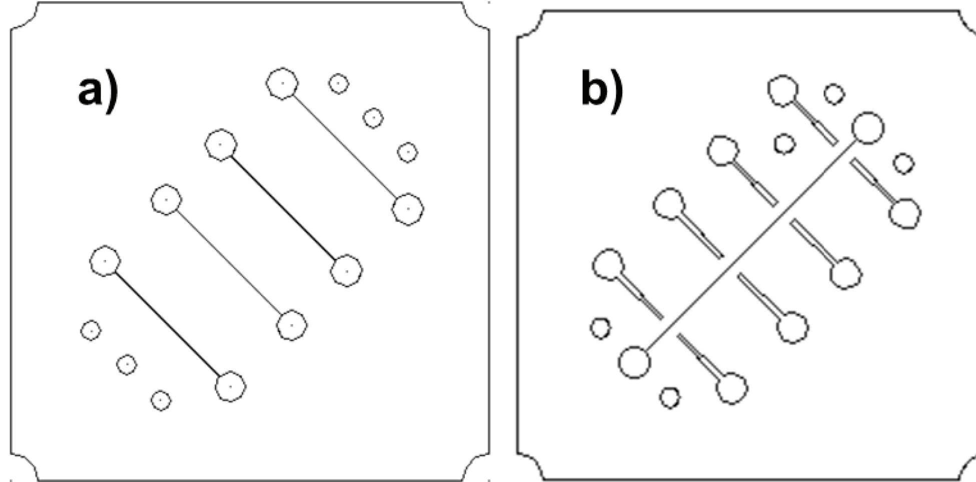

Figure 2.2: G1 mask set. The top cross leads are defined in (a) and bottom long lead is defined in (b). Each square has side length 2.5 cm.

the long side of the rectangular chip (bottom electrode). After deposition of this long lead, an aluminum layer is deposited and plasma oxidized so that the barrier material covers the entire chip area. Subsequently the top electrodes are evaporated through a second mask, running perpendicular to the bottom electrode to define the top cross leads. The barrier material that coats the chip is sandwiched between two electrodes at each of the four intersections in Fig. 2.3.

Each tunnel junction is connected to four electrical leads, so that four point resistance measurements can be performed (to eliminate contact resistance caused by the interface between a measurement probes and device wire). The four resulting crossed wire devices are indexed A through D. In Fig. 2.3, the A device is shaded in red. Figure 2.3(b) shows the micrograph of the A device, where the scale is indicated by the white arrows. These dimensions are representative of a device fabricated with the G1 mask set. Approximate device area is 100 μm^2, where the bottom lead is slightly wider than the top leads. For the typical layer

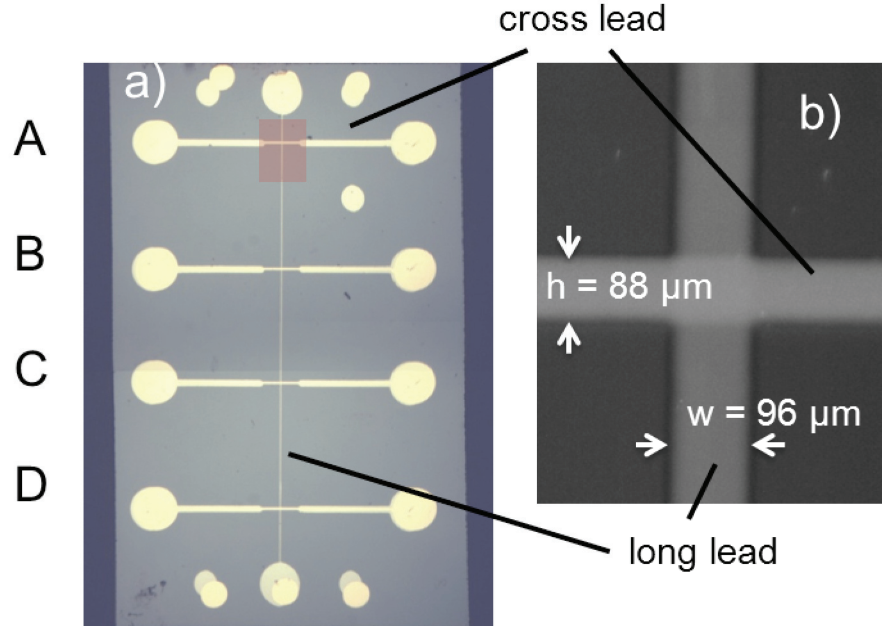

Figure 2.3: Tunnel junction devices fabricated with the G1 mask set. (a) The long lead is the bottom electrode, while the cross leads are top electrodes. Devices are formed at the four intersections. Devices can be probed by contacting the 10 circular contact pads. (b) Micrograph of A, where the scale is indicated by the arrows.

structure, a cross lead resistance (probes placed on opposite contact pads of a single cross lead in Fig. 2.3(a)) is approximately 100 Ω. The resistance of cross leads cannot be measured with four points. A typical long lead resistance is approximately 1500 Ω.

2.2.3.3 Second generation masks (G2)

The second generation (G2) masks were developed to make the following improvements:

- Decrease device area (to increase resistance)
- Increase the number of devices on each chip

- Implement "test patterns" for measuring the sheet resistance $(\Omega/\square)$ of both the top and bottom electrodes with a four point measurement

Devices with higher resistance increase dynamic range in the measurement of HCI modified devices. The second generation of shadow masks were manufactured by Tecan Inc. (`http://www.tecan.co.uk`). During the mask fabrication process, features were etched into hardened nickel with photolithography. The thickness of the nickel medium was 300 μm, and reduced to 50 μm around the features. The width of both the top and bottom feature sizes were specified to be 20 μm with an accuracy of ± 2 μm. A technical drawing of the masks is shown in Fig. 2.4. The masks for the bottom and top electrodes are shown in Fig. 2.4(bottom) and (top) respectively. Patterns for the contact pads on the mask are spaced at 0.1", so that the finished devices are compatible with the spacing of pins on a standard printed circuit board.

G2 masks produce chips with 8 devices, and two test patterns. Test patterns allow independent, four-point measurements of both the top and bottom leads, to extract the resistance per square $(R/\square)$ for the electrode materials. The test patterns are shown in Fig. 2.4 on the right side of both the top and bottom masks. Three magnified views of the masks are shown at the right in Fig. 2.4.

A device fabricated with the G2 mask set is shown in Fig. 2.5 along with four-point resistance measurement setup. The numbers on the leads correspond to the pin index marks on the printed circuit measurement board.

2.2.4 Plasma chamber

The final resistance of a tunnel junction is determined, largely, by the oxidation step. Design of a new plasma chamber was motivated by two primary

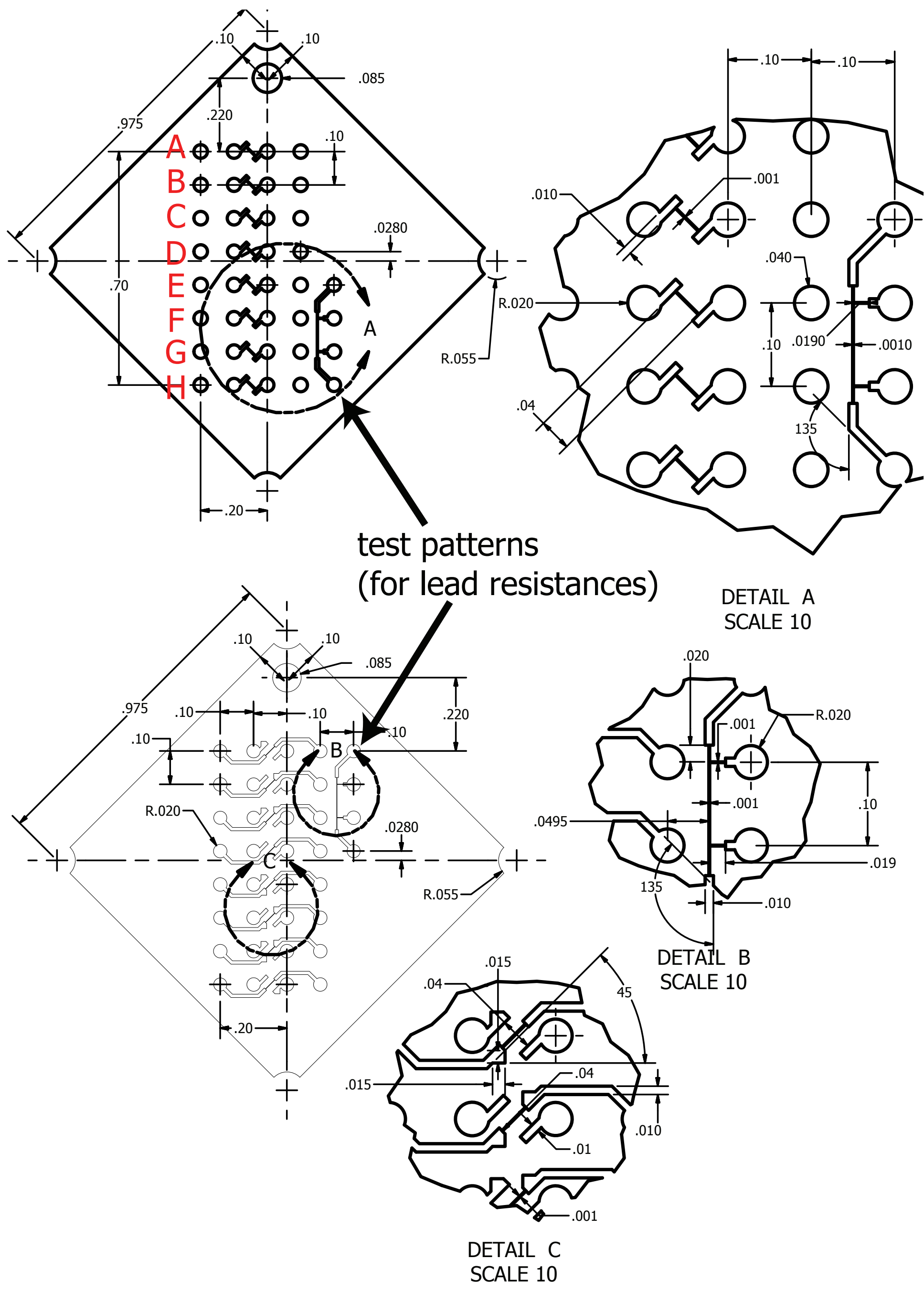

Figure 2.4: 2nd generation mask set.

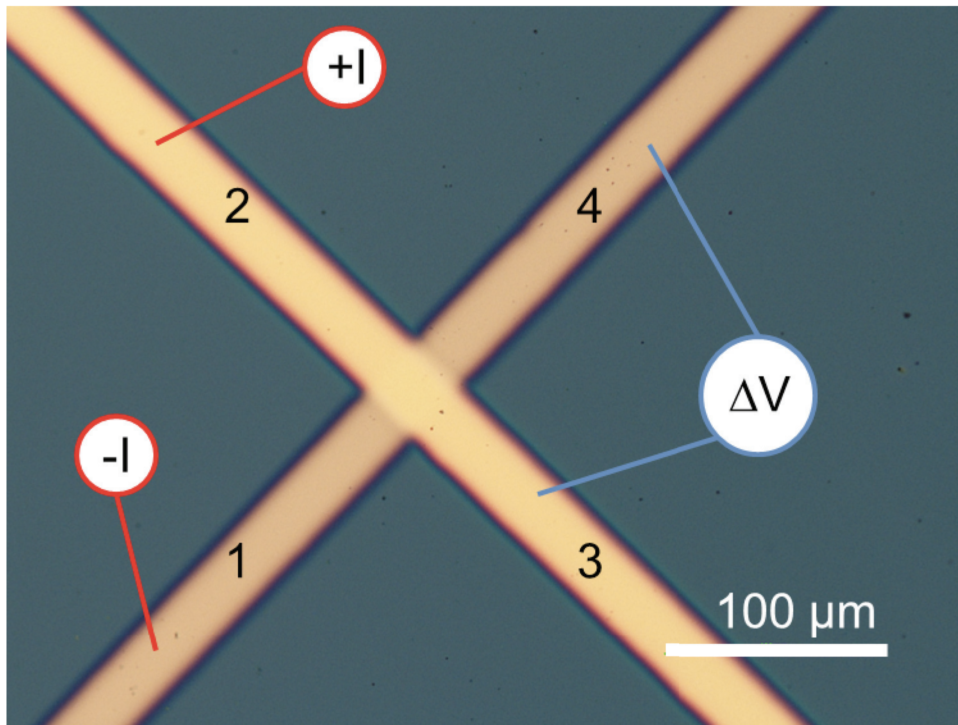

Figure 2.5: Tunnel junction micrograph with R_{4pt} measurement schematic. The four-point resistance is obtained $R_{4pt} = \Delta V / I$.

concerns:

- Remove instabilities in the electrostatic environment surrounding the chip.
- Minimize the total time required for oxidation.

The normal chamber pressure is 5×10^{-9} Torr when not in use. The plasma chamber is evacuated by a Pfeiffer-Balzers TMU 260 turbo pump (260 L/s), backed by a Agilent SH110 scroll pump. The plasma chamber is a cylindrical stainless steel chamber with a volume of approximately 5 L. Annotated photos of the plasma chamber are presented in Appendix A. A 24″ magnetic transfer rod, with a sample sled attached to the end, is used to bring chips to and from the main chamber. The sled has three sample positions and docks into a cut-out that runs along the diameter of the bottom plasma electrode ring (Appendix A; Fig. 4). In normal operation, the sled is in direct electrical contact with the grounded plasma electrode. A negative DC bias is applied to the top electrode to start a plasma discharge.

2.2.4.1 Pumping

The pumping system on the plasma chamber was designed for quickly introducing and evacuating O_2 gas, for fast oxidation and pump out after oxidation. A gate valve separates the turbo pump and chamber so that the port to the turbo pump can be closed and O_2 gas can be leaked into the chamber for plasma oxidation through a valve on the top flange. Closing the gate valve allows O_2 gas to be introduced without having to spin down the turbo pump. A stainless steel tube connects the (99.99% pure) oxygen tank to the leak valve. After an oxidation, a backing valve is opened between the chamber and backing scroll pump. The

scroll pump reduces the pressure in the chamber to around 50 mTorr. At this point, the backing valve can be closed, and the gate valve can be opened, to bring the chamber back to its base pressure (10^{-9}) Torr. The pressure of the O_2 gas during oxidation is low (100 mTorr), so that the turbo pump remains at full speed when pumping out the plasma chamber after oxidation.

2.2.4.2 Plasma electrodes

The plasma setup consists of parallel circular electrodes. The top and bottom electrodes are concentric with radii of approximately $r = 10$ cm and 14 cm respectively with a separation distance $d = 9.6$ mm. A DC glow discharge can be ignited by applying negative bias to the top (cathode) ring in a background of oxygen gas [55]. Kapton coated wire connects the vacuum side of a feedthrough on the top cluster flange of the chamber, to the cathode. A high voltage supply (Kepco BWK-1000, 1 kV, 200 mA) provides a timed, negative output bias, in constant current mode. The power supply is operated in fast mode and has built-in control over the time duration of the plasmas. Rise time of the bias output, to reach the current set point is less than 1 ms.

2.3 Plasma characteristics

2.3.1 Pressure, power, and optical emission

The primary plasma probe during oxidation for the experiment was a photodiode (ThorLabs `SM1PD1B`) mounted to a glass viewport and directed at the space between the anode and cathode. The distance between the photodiode and center of the plasma electrodes was approximatly 13 cm. Voltage signal from the

photodiode is proportional to the incident light power from the plasma. Voltage readout (V_{ph}) from the photodiode (in passive, unbiased mode) was recorded with a Tektronix Oscilloscope (TDS2000). The photodiode can measure incident light with wavelengths between approximately 300 nm and 1100 nm with a maximum responsivity peak of 0.65 A/W at 950 nm (Appendix B). By choosing a photodiode with a spectral response peaked in the low infrared, the detector is sensitive to the manifold of strong emission lines at 777 nm line in oxygen that produces O* radicals, which are considered to be the most important species in the plasma oxidation of aluminum [56]. Therefore, intensity of photovoltage signal (V_{ph}) gives a qualitative indicator of oxidation rate for samples in our experiments. The intensity of the light plasma is proportional to the number of excited O* species.

A representative photovoltage signal is shown in Fig. 2.6. The power supply (in constant current mode) was set at 40 mA for a programmed time t_{ox} = 3.3 s. Pressure in the chamber was initially 120 mTorr. In Fig. 2.6(a), at $t < 0$ s, the background photovoltage V_{ph} = 50 mV is due to ambient light in the laboratory incident on the photodiode through plasma chamber viewports. As the power supply turns on to ignite the discharge, the scope is triggered at $t = 0$ s, by the rise in photovoltage from plasma optical emission. When the discharge is on (0 s < t < 3.29 s), the measured photovoltage remains nearly constant at an average value V_{ph} = 239.9 mV with standard deviation 0.8 mV. Scope traces in Fig. 2.6 were taken at sampling frequency 0.5 kHz. As the power supply turns off, photovoltage signal drops exponentially with a e^{-1} decay time $\tau = 1.74 \pm 0.02$ ms. After the oxidation, the pressure measured on the Convectron gauge drops to 119 mTorr.

We use the photovoltage signal to compare plasma discharges created with different pressures and powers. Plasma discharges created at given pressures and

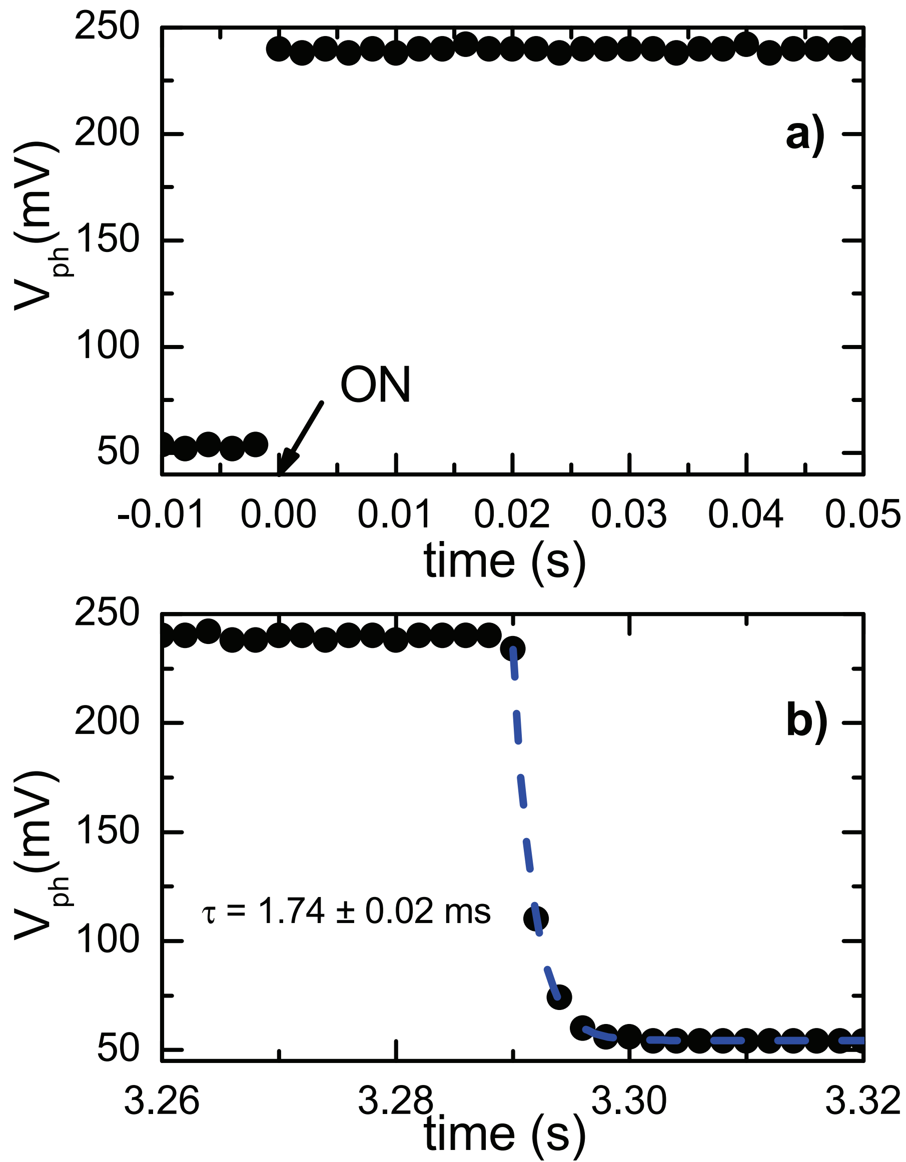

Figure 2.6: Photovoltage at the (a) beginning and (b) end of a plasma discharge.

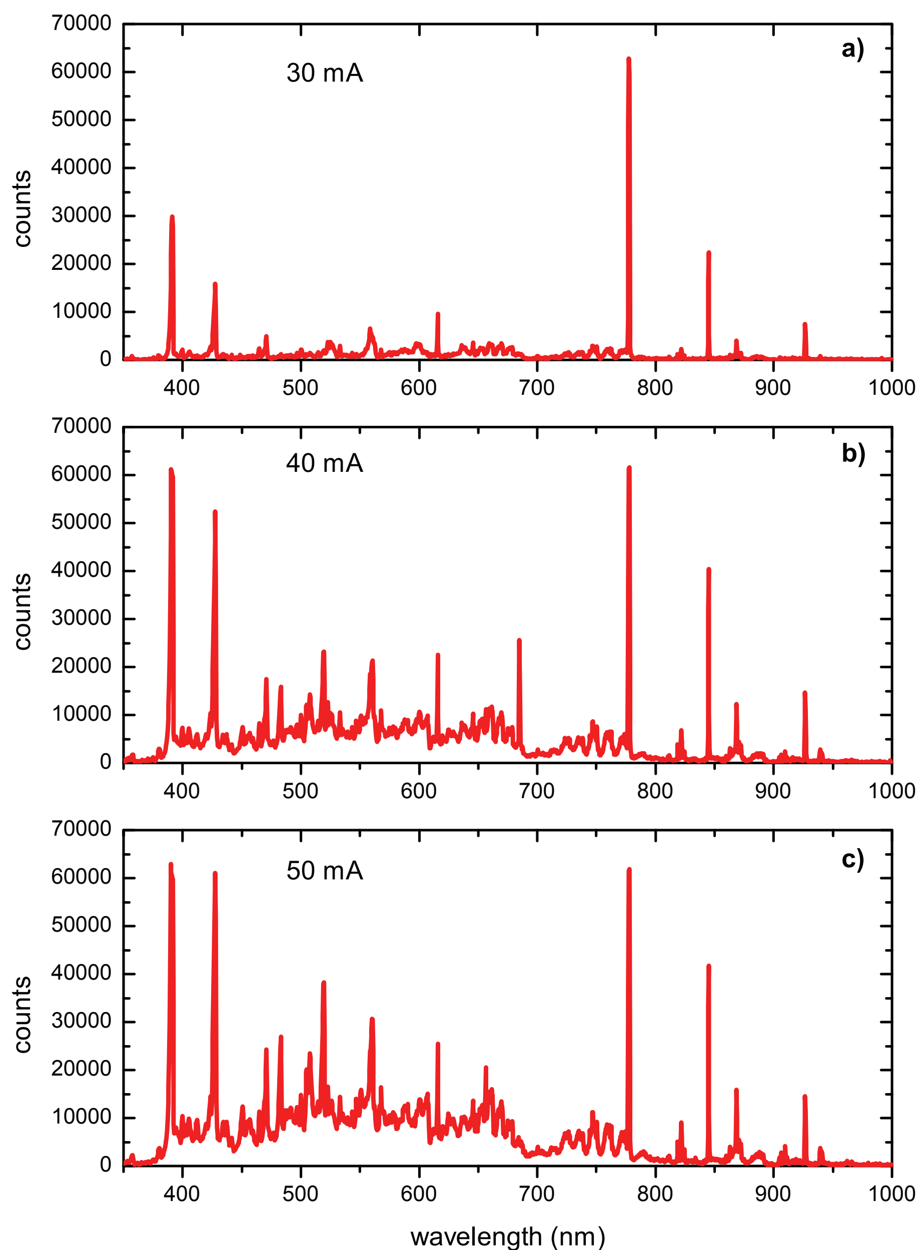

Figure 2.7: Optical emission from three plasmas obtained with the power supply in constant current mode for set points (a) 30 mA, (b) 40 mA and (c) 50 mA. Spectra were obtained with integration times 23.5 s, 13.2 s and 23.3 s respectively.

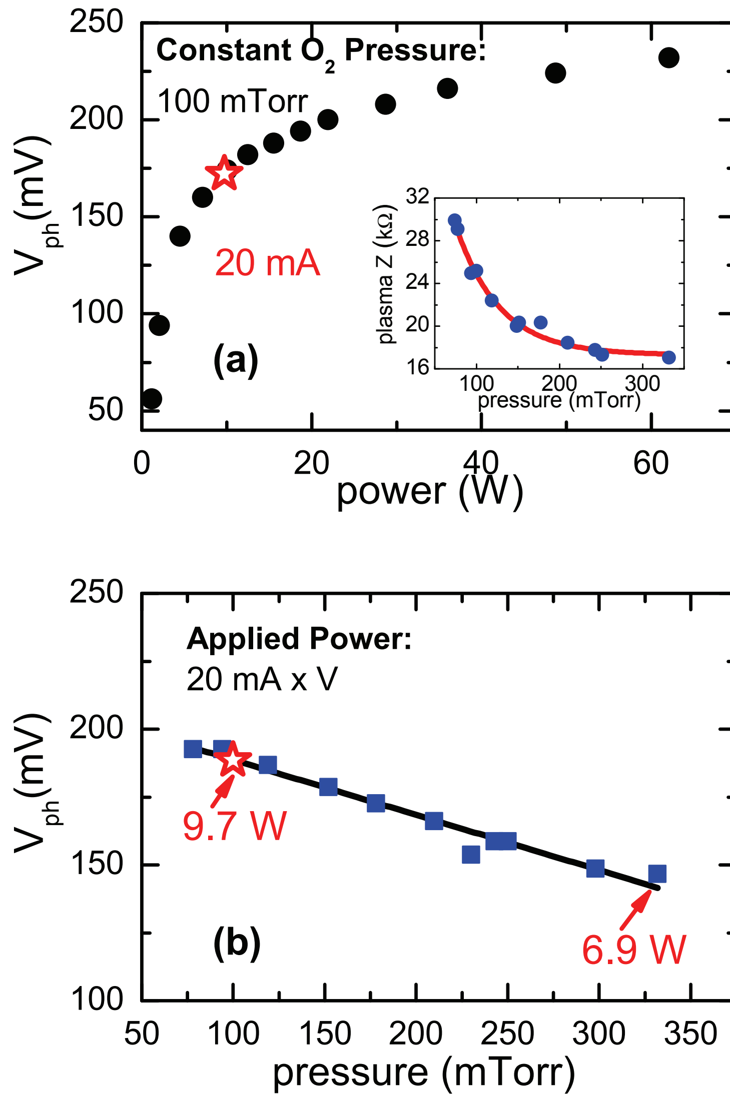

Figure 2.8: Brightness of a DC oxygen discharge as a function of (a) applied electrical power and (b) pressure. The inset in (a) shows plasma impedance falling exponentially with increasing pressure. Spacing between the parallel electrodes is 9.6 mm.

powers give very reproducible V_{ph} signals from run-to-run, even when the runs are performed on different days.

The plasma itself is charge neutral, but contains both positive and negative atomic and molecular ions, and free electrons [56]. Additionally, the plasma contains neutral excited oxygen species (O*) that are highly reactive, and critical in the oxidation process. At higher pressure, O* have a shorter mean free path, collide and thermalize with background constituents of the plasma, before reaching the sample. On the other hand, at low pressures excited oxygen radicals have a longer mean free path and are more likely to collide with the substrate before colliding with other gas particles. Kuiper and co-workers observed no change in the oxidation rate when reversing the bias between the sample and opposite electrode. This indicates that O* are the main species in the oxidation process [56]. The transition in oxygen that produces O* radicals emits lines at 777 nm. Therefore the overall population of O* species is proportional to the V_{ph} signal during the discharge.

Representative spectra from plasmas at three different powers are shown in Fig. 2.7. The scans (a), (b) and (c) in Fig. 2.7 were acquired with different integration times 23.5 s, 13.2 s and 23.3 s respectively using the BWTEK model BRC112P-V spectrometer. Oxygen pressure was constant at 120 mTorr. During these measurements, the plasma chamber was shielded from ambient light. We find that the photoemission spectra from the DC discharges are similar to those in Ref. [56]. Specifically, most of the light intensity originates from the lines at 777 nm. We observe that the ratio of the intensities between the 555 nm (molecular ions) line and the 777 nm (radicals) line decreases with increasing plasma power. Therefore, increasing the plasma power has a similar effect on the optical emission spectra as decreasing the pressure [56].

The Kepco BWK-1000 can dynamically change voltages to maintain constant current for loads that have time-varying resistance. This is important for igniting and maintaining a DC plasma. Impedance between the two plasma electrodes is the largest before breakdown occurs. Once enough bias has been applied between the plates to start breakdown, Z drops. To maintain constant current, the applied bias must drop accordingly. This process happens at the microsecond timescale at $t < 0$ s in Fig. 2.6(a). Thus, one requirement for the power supply driving the plasma, is that it can handle dynamic loads. Details on the hysteretic behavior of I-V characteristics are given in Ref. [55]. In practice, DC power supplies should have faster than millisecond rise times for resistive loads of greater than 30 kΩ. After overcoming the initial high impedance between the electrodes, the resistance drops to a nearly constant value V during the discharge. Between 0 s < t < 3.29 s, in Fig. 2.6, the voltage applied to the top electrode was V = -528 V in order to maintain the constant current set point of 40 mA. This means that the average applied power during the discharge was 21 W.

To demonstrate how pressure and applied power affect the intensity of the light power of the plasma, Fig. 2.8 plots the photovoltage V_{ph} signal (after subtracting the contribution from ambient light) as a function of pressure and power. The inset in Fig. 2.8(a) plots the the average plasma impedance, Z during the discharge. In Fig. 2.8(a) the photovoltage-power relationship is shown for plasmas at constant pressure (100 mTorr). Here, each V_{ph} point is the average value of the photovoltage step height during a programmed 30 s discharge. Each point corresponds to a single I_{set} value. Current set points were varied from 3 mA to 90 mA in Fig. 2.8(a). As power increases, the total light intensity of the plasma increases.

The inset of Fig. 2.8(a) shows the impedance of the plasma $[Z(t)]$, dur-

ing times $t > 0$ s. As pressure increases, plasma impedance drops exponentially. Here, the impedance is defined as $Z = V/I_{set}$. The plasma becomes more conductive as the amount of oxygen between the electrodes increases. An exponential decay model empirically describes the decrease [$Z = Z_0 + Z_1 \exp(p/p_0)$], with fit parameters $Z_0 = 17k\Omega$, $Z_1 = 50k\Omega$, and a characteristic pressure p_0 = 17.3 mTorr. This fit allows extrapolation of plasma electrical characteristics to different pressures and powers. For example, the inset and fit parameters allows one to predict the maximum power supply voltage setting needed for a given I_{set} and oxygen pressure. For the plasmas in Fig. 2.8(a), impedance was $Z = 25$ kΩ.

Fig. 2.8(b) plots V_{ph} as a function of pressure. As the pressure increases, the plasma impedance Z decreases according to the trend shown in the inset of (a). As Z decreases with increasing pressure, the voltage drop required to maintain a given I_{set} drops as well. The star is plotted at 100 mTorr to show where the data in (a) fall, within the pressure trend shown in (b). Plasma light intensity decreases linearly with increasing pressure. The line in Fig. 2.8(b) plots this measured linear decrease in photovoltage with increasing pressure, with slope -0.20 mV / mTorr.

2.4 Device characteristics

2.4.1 Resistance measurements

For each measurement, chips were held in a custom jig where spring pins electrically contacted the on-chip pads. Typical resistance measurements were done at small bias voltages. A HP 3468B multimeter was setup in four-point resistance measurement mode. The multimeter sourced a constant DC current (1 mA or less) through the devices by applying positive bias to the top electrode. A

Keithley 2000 multimeter, connected in series, monitors the source current flowing through the device. Then, the voltage difference induced by the source current can be sensed across the other device electrodes that are connected to the sense terminals of the multimeter. Placement of the leads for sourcing current and sensing voltage is depicted in Fig. 2.5, where I is the source current, and ΔV is the voltage drop measured across the sense terminals.

The differential conductance (dI/dV) measurements were obtained similarly, using a Keithley 2612 system source meter interfaced via GPIB to a computer with Labview. In this case, the bias between the source and drain was modulated to change the current flowing through device, while simultaneously the voltage drop across the device at each source current value was measured. First current-voltage data were recorded. These data were then numerically smoothed, and differentiated to obtain dI/dV as a function of bias voltage.

2.4.2 Negative resistance artifacts and measurements limits

Four point resistance measurements avoid the problem of contact resistance that is present in a two-point measurement. However, there is a "negative resistance" artifact that causes the measured four-point resistance (R_{4pt}) to be smaller than the actual device resistance (R_{dev}) [57, 58]. For devices with small resistance compared to the measurement leads, this effect can result in a large relative error in the resistance measurement [57]. The "negative resistance" error is non-linear, *i.e.*, it affects low resistance devices, more than it affects high resistance devices. However, it is systematic and can be corrected for based on measurements of device geometry and lead resistances. Figure 2.9 shows voltage contour plots during four point resistance measurements, taken from Ref. [57]. On

the top of Fig. 2.9, ($R_{dev} = 100\ \Omega$), and the equipotential lines (spaced at $1/100$ of the difference between the source and drain voltage) are perpendicular to the electrodes. The four point measurement principle is to apply a voltage between leads V_s and V_d, causing a current I_t to flow from V_s on the top lead, through the device, and to V_d on the bottom lead as shown in Fig. 2.9. The four-point resistance of the device can be obtained by measuring the voltage drop $(V_H - V_L)$ that I_t induces, so that $R_{4pt} = (V_H - V_L)/I_t$.

For high resistance devices, most of the voltage drop caused by I_t occurs over the device itself, and so the measurement of $(V_H - V_L)$ is hardly affected by the current flowing through the device (top of Fig. 2.9). However, for devices with resistances that are much less than the leads, a significant portion of the voltage drop can occur in the regions surrounding the device, causing the voltage profile around the device to become distorted as can be seen from the equipotential lines in Fig 2.9 (bottom). This causes $V_h \approx V_s$ and the voltage measurement is no longer independent of the source-drain current. For the parameters shown in Fig. 2.9 and discussed in Ref. [57] (rectangular leads $W > H$, with resistances of $100\ \Omega$), this effect causes the $0.1\ \Omega$ resistor to be measured as $R_{4pt} = -0.13\ \Omega$. The effect is also present for higher resistance devices, but results in a much smaller relative error.

The correction procedure requires the following set of equations [57],

$$\Delta R_\infty = \frac{1}{6}\left(R_{\square t}\frac{W}{H} + R_{\square b}\frac{H}{W}\right) \tag{2.2}$$

$$R_{4pt} = \frac{\sqrt{6(\Delta R_\infty + \Delta R_0)R_{dev}}}{\sinh(\sqrt{6(\Delta R_\infty + \Delta R_0)/R_{dev}})} + \Delta R_0. \tag{2.3}$$

Here, ΔR_0 is the resistance of a device with no barrier, ΔR_∞ is an upper

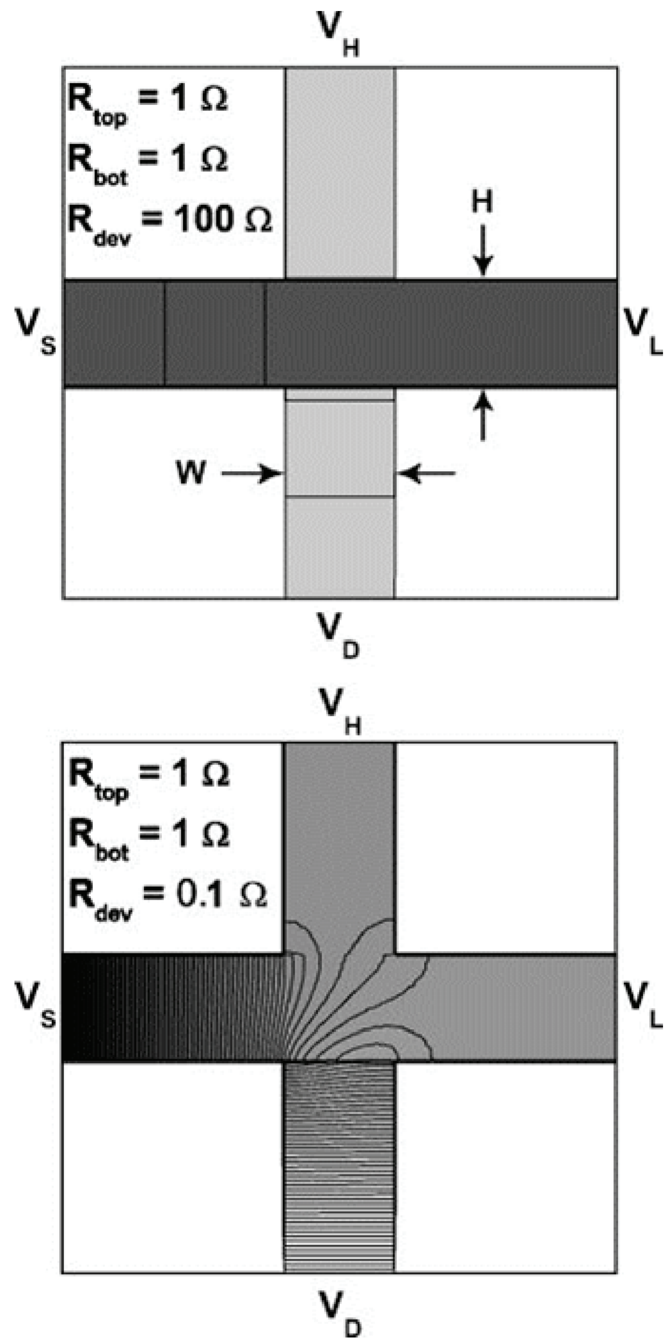

Figure 2.9: Voltage contour plots for the measurement of (top) R_{dev} = 100 Ω and (bottom) 0.1 Ω devices (from Ref. [57])

limit on the error, and R_{dev} is the actual device resistance. In order to perform the correction, the resistance per square $R_{\Box i}$ for leads must be known, where i corresponds to either the top or bottom electrode. This quantity is determined by measuring the resistance of top and bottom leads, and dividing the resistance by the number of squares in the length of the wire. Then, with a measurement of R_{4pt}, one can solve for the root R_{dev} which is the corrected resistance in Eq. 2.3. The difference between R_{4pt} and R_{dev} changes with the actual RA product of the device.

One motivation for developing the G2 mask set was that the smaller device areas provide higher resistances. Therefore, the "negative resistance" artifact constitutes less relative error in the measurement of R_{4pt} than for a low resistance device. Figure 2.10 shows relative error due to the negative resistance as a function of $R_{dev}A$. The red and black lines plot (as a percentage) $-|R_{4pt} - R_{dev}|/R_{dev}$, against the actual RA product of the device for the G1 and G2 devices respectively.

In both the red and black lines, material properties of the leads is assumed to be exactly the same. The square resistance of the top electrode is approximately $R_{\Box t}$ = 1.77 $\Omega/\Box$ and the bottom electrode is approximately $R_{\Box b} = 15.4\Omega/\Box$. The G1 device has an area $\approx$ 11 times larger than the G2 device, meaning that its resistance is reduced by the same factor. Both devices have a slightly rectangular shape $(H \neq W)$, where (H x W) = 88 $\mu m \times$ 96 μm for G1 and (H x W) = 33 $\mu m \times$ 28 μm for G2.

The smaller area of devices fabricated with the G2 cause these devices to suffer relatively less "negative resistance" error at a given RA than the G1 devices. In other words, the smaller mask set allows measurement of devices with lower RA products, with less relative error due to the artifact. The dashed line in Fig 2.10 shows where the relative error of the R_{4pt} measurement is 10 %

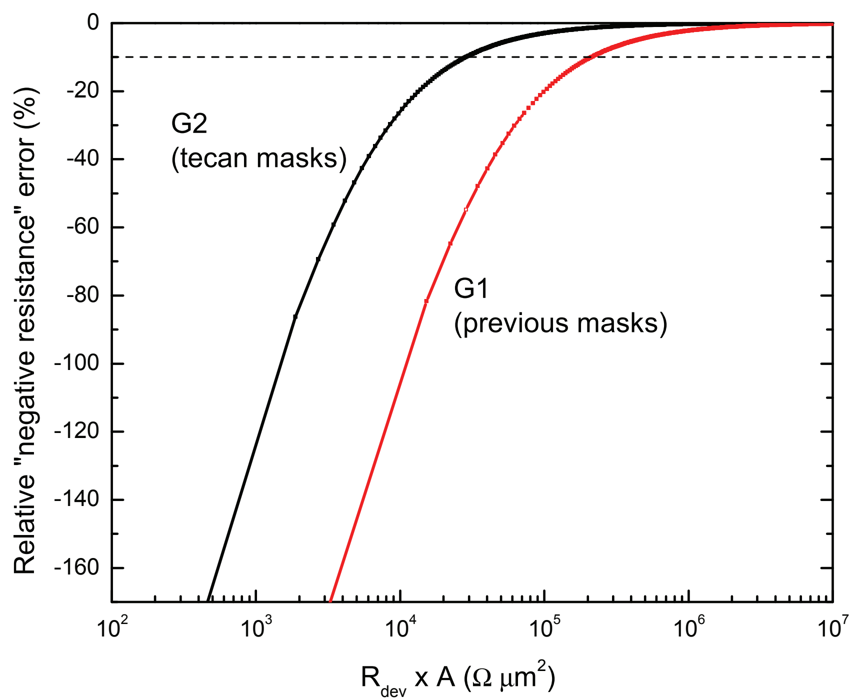

Figure 2.10: Relative four-point resistance error $-|R_{4pt} - R_{dev}|/R_{dev}$ as a function of the actual device RA from two different mask sets.

of the actual device resistance. For the G2 device, this line intersects with the relative error plot at $3.03 \times 10^6\ \Omega\ \mu m^2$. Devices with RA products greater than $2.95 \times 10^4\ \Omega\ \mu m^2$ have less than 10 % error due to the negative resistance. On the other hand, with the G1 devices, RA products greater than $2.22 \times 10^5\ \Omega\ \mu m^2$ meet this condition. The relative magnitude of negative resistance errors is reduced (at constant RA), when using a smaller mask set.

The percent relative error plotted in Fig. 2.10 is the error in R_{4pt} *before* applying the correction outlined in Eqs. 2.2. For the devices with less than -10 % error in Fig. 2.10, the correction procedure can be used to establish R_{dev} within about $\pm 0.1\ \Omega$ accuracy.

2.4.3 Oxidation time

Fig. 2.11 shows resistance of tunnel junctions as a function of oxidation time for three different applied powers. All devices shown here were deposited using the G2 mask set, making each device area approximately $(30\ \mu m)^2$. The different applied powers during oxidation 15 W, 21 W, 27 W correspond to I_{set} values of 30 mA, 40 mA and 50 mA respectively. All oxidations were completed in 120 mTorr of oxygen pressure. For the 21 W oxidation, device resistance follows an exponential increase with time. The time constant extracted from an exponential growth (the solid line), was $\tau = 0.28 \pm 0.02$ s, where the uncertainty is the standard error of the fit.

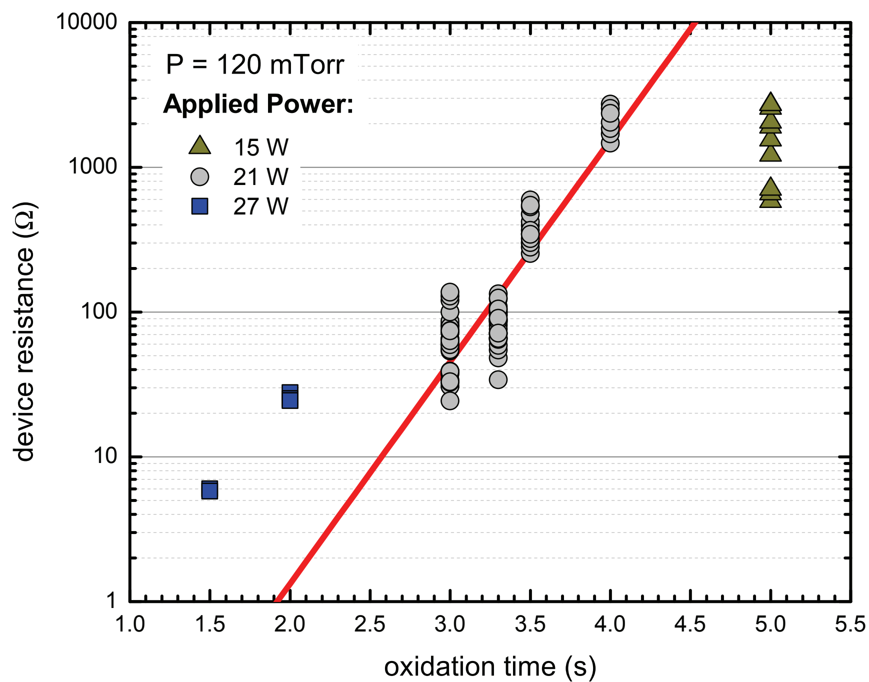

Figure 2.11: Resistance as a function of oxidation time. The red line is an exponential fit to the 21 W data where $R(t) = A_1 \exp[t/\tau]$. The fit yields the parameters $\tau = 0.28$ s and $A_1 = 1.32$ mΩ.

2.5 Modeling the tunneling resistance

Rowell describes three basic characteristics of good tunnel junctions [59]: 1) resistance is exponentially dependent on thickness, 2) differential conductance curves have a parabolic shape, and 3) the junctions have an insulator-like temperature dependence. If all three criteria are satisfied, it is reasonable to assume that tunneling is the dominant transport mechanism. The most rigorous test is probably (3) because devices with pinholes can demonstrate (1) and (2). In the following section, we focus on the current-voltage characteristics of our junctions. Regarding Rowell's third criterion, an insulator-like resistance-temperature dependence for a G1 device is shown in Appendix C.

The current density (current per device area) can be expressed by the integral [6],

$$J(V) = \frac{4\pi me}{h^3} \int_0^{E_m} \rho(E_x, V) D(E_x) dE_x. \tag{2.4}$$

In this expression, m is the mass of the electron, e is the elementary charge, h is the Planck constant, E_m is the maximum energy of an electron in an electrode, E_x is the energy associated with the momentum of an electron perpendicular to the barrier and D is the tunneling probability. The total current flowing through the device depends on the device area, $I(V) = A[J(V)]$. The supply function ρ is derived from the Fermi-Dirac distribution [60]:

$$\rho(E, V) = \rho_1(E)\rho_2(E - eV)[f(E) - f(E - eV)] \tag{2.5}$$

where ρ_1 and ρ_2 are the density of states in each electrode. For the Co/Al_2O_3/Co tunnel junctions at low bias, we assume that the densities of states at the Fermi energies are identical on each side of the barrier ($\rho_1(E) = \rho_2(E) \equiv \bar{\rho}$) . In the

absence of external magnetic fields, the magnetizations of the electrodes will be parallel due to exchange interaction between the electrodes. Therefore, at low bias voltages, the density of states on each side of the barrier is approximately equal. This assumption would break down at high bias voltages or if the magnetizations of the electrodes were anti-parallel [61].

The WKB approximation gives the following expression for the tunneling probability [6, 44, 62]:

$$D(E_x) = \exp\left\{-\frac{4\pi(2m)^{1/2}}{h}\left(\int_{x_1}^{x_2}[\phi(x)+E_F-E_x]^{\frac{1}{2}}\,dx\right)\right\}. \tag{2.6}$$

Here E_F is the Fermi level of the negatively biased electrode. The potential barrier between the two electrodes is produced by the energy band gap within the dielectric barrier material. The height of the barrier is approximately equal to the difference between the Fermi level in the metal electrodes, and the bottom of the conduction band within the dielectric (shown schematically in Fig. 2.12). The exact barrier height and shape [$\phi(x)$] is a complex function that depends on work functions of the metal electrodes, electron affinity of the insulator, image forces, dielectric constant, and applied bias [6]. There are a number of physical reasons for deviation of the actual barrier shape, from rectangular (discussed below).

An energy diagram for this system is shown in Fig. 2.12. When a bias is applied between the two layers, electrons pass from one electrode to the other via quantum mechanical tunneling processes, through the barrier formed by the energy gap within the dielectric material. Electron transmission probability depends exponentially on the barrier thickness. Therefore, resistance depends exponentially on the width or thickness of the barrier. Angstrom-scale decreases in barrier thickness results in a large reduction in device resistance. Tunneling can

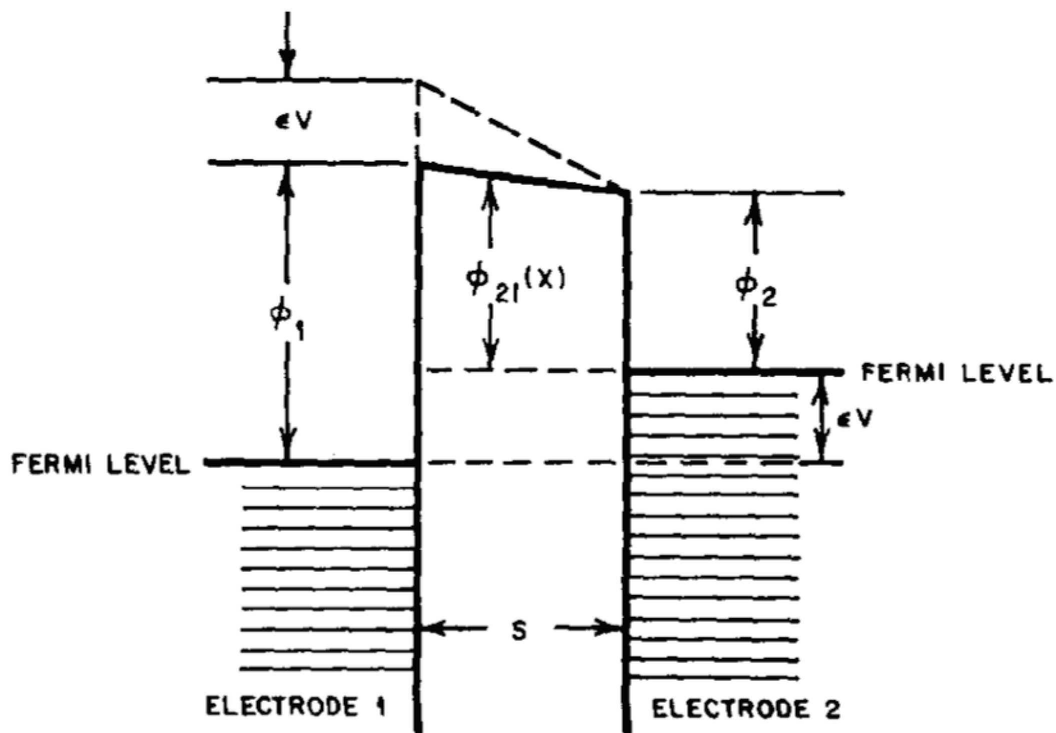

Figure 2.12: The asymmetric barrier tunneling model (from Ref. [6])

be used as a mechanism to electrically detect small changes in length.

The points x_1 and x_2 define the barrier width and are the limits of the integral in Eq. 2.6. These are the classical turning points, within the formalism of WKB. One should note that the WKB expressions for calculating tunneling probability are only valid in the limit that the classical turning points (x_1, x_2), are not too close together compared to the tunneling electron's wavelength. Another criterion for validity is that the energy of the electron is not too close to a maximum of the potential in the tunneling region. This means that the WKB approximation is valid for relatively thick and high barriers. These mathematical criteria of WKB are discussed in detail in Ref. [62].

In general, the integral in Eq. 2.6 has no closed form solution. Therefore, a common approach is to rewrite $\phi(x)$ as a rectangular or trapezoidal barrier in order to arrive at a tractable expression for modeling experimental I-V data [6, 44, 60, 63]. These models express the actual barrier as having and effective height ϕ_r and width $\Delta x = x_2 - x_1$. The fits to I-V data in this thesis use the trapezoidal barrier model from Ref. [6]. The primary advantage to using this model is that fitting the data with $\phi_1 \neq \phi_2$ captures the asymmetry of the I-V curve about zero bias. Assuming that $\phi(x)$ has a trapezoidal form, the integral:

$$\phi_{r21} = \frac{1}{\Delta x}\left\{\int_{x_1}^{x_2} [\phi(x)]^{\frac{1}{2}}\, dx\right\} \tag{2.7}$$

can be solved to yield an analytical solution for the barrier height. The ϕ_{r21} expression used in the fits in thesis dissertation comes from Eq. (16) in Ref. [6]:

$$\phi_{r21} = \frac{4\left[\phi_2^{1/2} - (\phi_1 - eV)^{3/2}\right]^2}{9(\phi_2 - \phi_1 + eV)}. \tag{2.8}$$

Equation 2.8 defines ϕ_1 and ϕ_2 such that the positive bias is applied to the left electrode, as can be seen in Fig. 2.12. The "21" notation means that electrons tunnel from electrode 2 through the trapezoidal barrier to electrode 1, during positive bias on electrode 1 (Fig. 2.12). This expression is valid for the low bias regime where, $0 \leq V_{21} \leq \phi_{r21}/e$. At higher bias values, the Fermi level on electrode 1 can drop below ϕ_1 causing Fowler-Nordheim tunneling (not discussed here).

Substituting Eq. 2.8 as the barrier height expression $\phi(x)$ in Eq. 2.6 and inputting the resulting tunneling probability expression into Eq. 2.4 gives [6],

$$J = \frac{3e(2m)^{1/2}}{\beta(h\Delta x)^2} \left\{ \phi_r \exp\left[-\beta \Delta x \phi_r^{1/2}\right] - (\phi_r + eV) \exp\left[-\beta \Delta x (\phi_r + eV)^{1/2}\right] \right\}. \tag{2.9}$$

In the previous expression, it is convenient to group some of the fundamental constants together, in units of eV and Å:

$$\beta = \frac{4\pi(2m)^{1/2}}{h} \approx 1.025 \text{ eV}^{-1/2}\text{Å}^{-1}. \tag{2.10}$$

The partial derivative of J with respect to bias voltage defines the areal conductance density g (with dimensions of $[\Omega^{-1}\text{m}^{-2}]$). For the most part, devices discussed in this thesis are operated in the low bias limit $(V \to 0)$. The derivative of Eq. 2.9 as $V \to 0$ is the low bias areal conductance

$$g = \frac{3G_0}{8\pi(\Delta x)^2} \left(\frac{\beta s \sqrt{\phi_r}}{2} - 1 \right) \exp(\beta \sqrt{\phi_r} \Delta x). \tag{2.11}$$

The conductance quantum is defined as $G_0 = 2e^2/h = 77.4809\ldots\,\mu\text{S}$. The conductance of a device $\partial I(V)/\partial V$ is then,

$$\frac{\partial I(V)}{\partial V} = G(V) = A(\partial_V J). \tag{2.12}$$

Sample name	t_{ox} (s)	s (Å)	ϕ_1 (eV)	ϕ_2 (eV)	R_0 (Ω)	A (μm^2)
111209-14B	3.0	14.54 ± 0.06	0.722 ± 0.007	0.94 ± 0.01	37.4	840
111213-02B	3.3	15.30 ± 0.06	0.739 ± 0.007	0.91 ± 0.01	77.5	840
111024-05B	3.5	15.59 ± 0.05	1.12 ± 0.01	0.876 ± 0.007	397.9	840
110908-03F	4.0	17.0 ± 0.2	1.08 ± 0.04	1.07 ± 0.04	3170.6	1090

Table 2.3: Parameters of I-V fits shown in Fig. 2.13

The total conductance of the device $G(V)$ scales linearly with the device area A. For this reason, resistance-area is a useful concept for comparing different devices. Two tunnel junctions composed of identical materials, but with different areas will have the same RA product. From the previous equation, the corrected four-point resistance discussed in the previous section, is simply $[G(V \to 0)]^{-1}$ and the resistance-area product can be modeled as $A/G(V \to 0)$.

Figure 2.13 displays conductance $(\partial I(V)/\partial V)$ as a function of bias voltage for four different oxidation times (t=3.0 s, 3.3 s, 3.5 s, 4.0 s). The barriers were formed by plasma oxidation (21 W, 120 mTorr) of 1.1 nm of aluminum. In these plots, for $V > 0$, positive bias is applied to the top electrode, *i.e.*, electrons tunnel from the bottom electrode to the top. As described in the literature, the conductance is flat at very low biases around $V = 0$ and has an approximate V^2 dependence at higher voltages (below the Fowler-Nordheim regime). Each $\partial I(V)/\partial V$ spectrum was fit using Chow's model, to extract barrier heights ϕ_1, ϕ_2 and thickness s. Results of the fit are shown in Table 2.3.

Two identical electrodes separated by an ideal square and uniform barrier would yield $\phi_1 = \phi_2$, when fitting with Chow's model. Additionally, the barrier height would be equal to the difference in energy between E_F and the conduction band minimum of the barrier material (neglecting the image force). However, in real systems, some degree of asymmetry in the barrier heights is always observed.

The minima of the parabolas are offset from $V = 0$ due to asymmetry in the

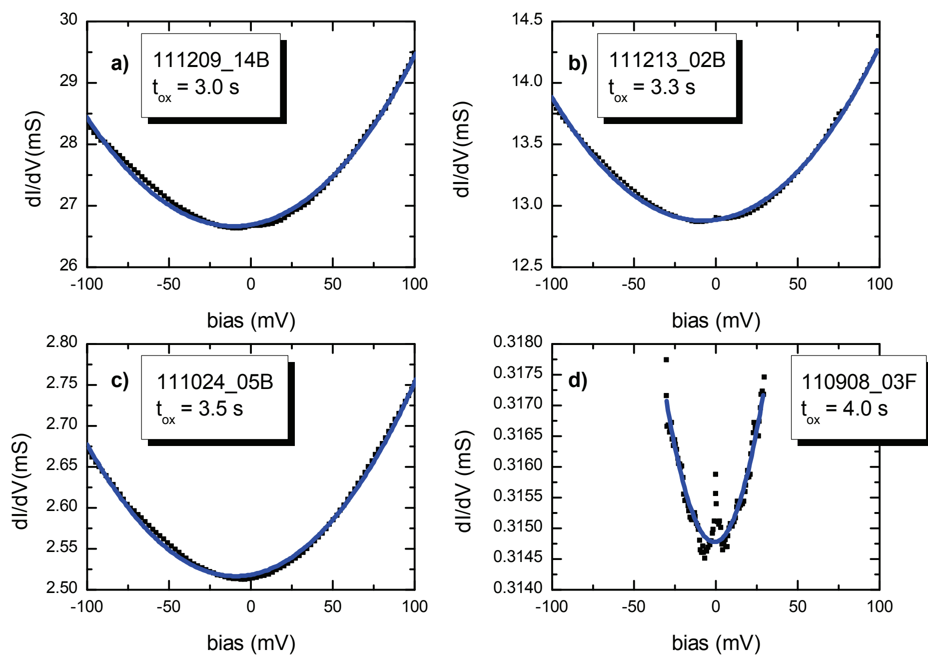

Figure 2.13: dI/dV as a function of bias voltage.

barrier height at each metal-insulator interface. Two main factors can contribute to barrier asymmetry. These inculde work function differences between the two electrodes, and non-uniformity of the chemical composition of the barrier. The values of ϕ_1 and ϕ_2 yielded from a fit are likely a convolution of both barrier parameters and relative alignments of the Fermi energies in the electrodes.

Figure 2.14 plots the fit parameters (s, ϕ_1 and ϕ_2) from Chow's model, as a function of oxidation time. Four devices were measured to make this plot. Multiple values of the fit parameters at single oxidation times, represent fits from different $dI(V)/dV$ measurements performed on the same device.

In Fig. 2.14(a) the extracted barrier thickness increases linearly from about 14 Å to 17 Å as oxidation time increases from 3.0 s to 4.0 s. A linear fit describes the data well, with a growth rate of 2.6 Å s^{-1} (blue line). Assuming a bulk atomic density for crystalline Al_2O_3 of 11.7×10^{22} cm^{-3} [56], a 11 Å thick Al film would expand to 14 Å. Thicknesses larger than 14 Å can be interpreted as either super-stoichiometric concentration of oxygen in the barrier material, oxidation of the Co electrode underneath the barrier, or uncertainty in the thickness of the intially deposited Al film.

For tunneling magnetoresistance (TMR) measurements, it has been shown that a nearly stoichiometric concentration of oxygen in the aluminum oxide, results in the optimum %TMR [56]. In our experiment, growing devices at this optimum oxidation state is not critical. The most important factor is the reproducibility of the barrier thickness, over many different chips. Devices with higher initial resistance (R_0) allow a greater dynamic range of HCI dose. Of the devices shown in Fig. 2.14, the $t_{ox} = 3.3$ s samples were selected for use in the experiments with HCIs.

Fig. 2.14(b) plots the fitted barrier heights on each side of the barrier (mod-

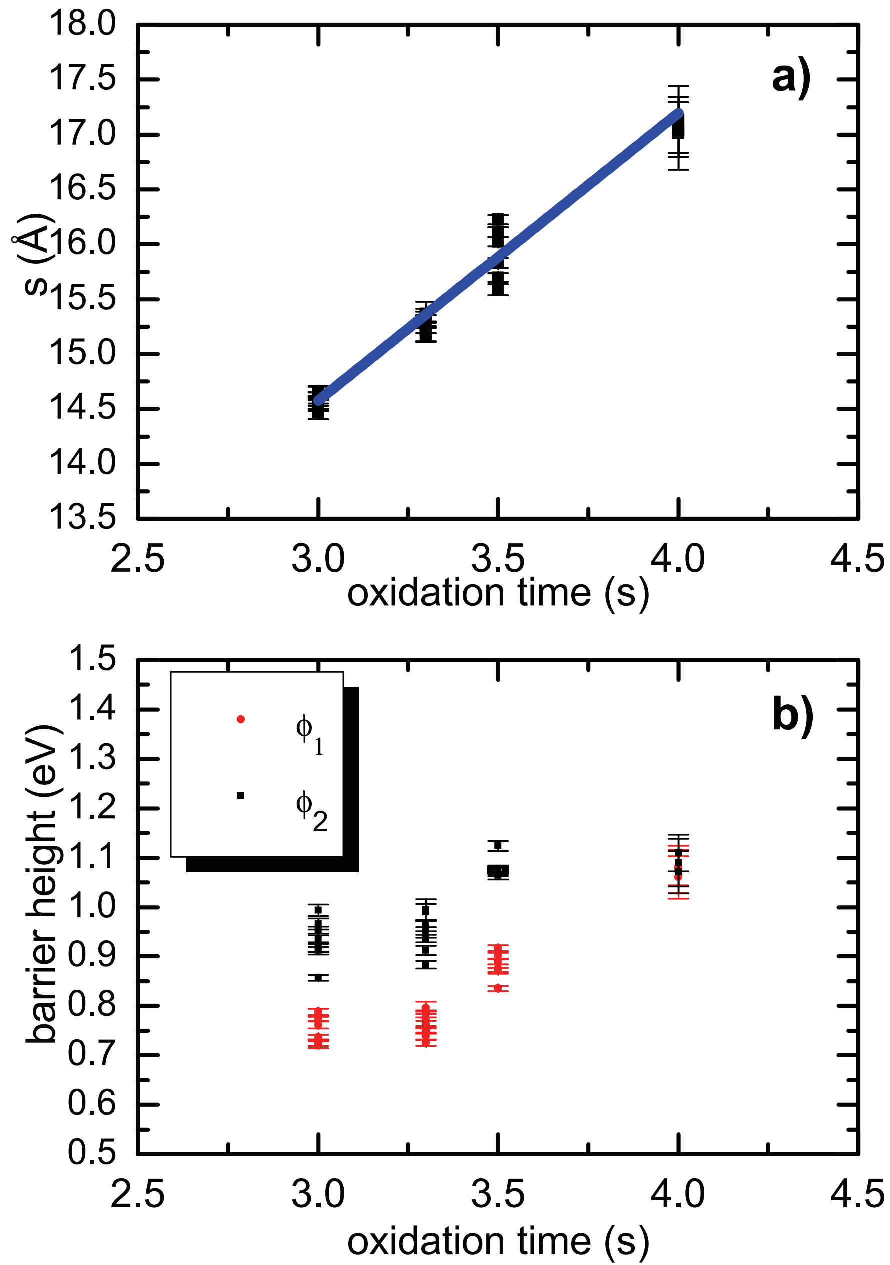

Figure 2.14: Thicknesses (a) and barrier heights (b) extracted from fits to dI/dV curves in Fig. 2.13.

eled as trapezoidal). As described above, when $V > 0$ the applied positive bias pulls electrons to the top electrode. Within the formalism of Fig. 2.12, the top electrode is on the left, meaning that ϕ_1 and ϕ_2 refer to the barrier heights at the top and bottom interface of the tunnel junction, respectively. When the bias is reversed ($V < 0$), electrons tunnel to the bottom electrode. However the expression that defines the trapezoidal barrier remains Eq. 2.8.

For the data shown in Fig. 2.14, ϕ_1 is less than ϕ_2 for oxidation times less than 4.0 s. For $t = 3.0$ s and $t = 3.3$ s, both barrier heights remain relatively constant, and asymmetric. As oxidation time increases beyond 3.3 s, both ϕ_1 and ϕ_2 increase, as the barrier asymmetry decreases. At t = 4.0 s, the barrier is nearly square. The barrier heights ϕ_1 and ϕ_2 converge at a value of approximately 1.1 eV.

The two heights extracted from the I-V fits (ϕ_1 and ϕ_2) represent a convolution of inhomogeneity in the barrier chemical profile and the difference in the Fermi energies between the right and left electrodes.

2.5.0.1 Oxidation process

The data shown in Fig. 2.13 are consistent with the following scenario for oxidation. Initially, as $\approx$100 mTorr oxygen is introduced into the plasma chamber, a small amount of oxygen is immediately incorporated into the aluminum film, to start thermal oxidation. Within seconds, the bias is applied between the plasma electrodes to form an oxygen discharge. The discharge is composed primarily of oxygen ions (O^+,O_2^+) and excited radicals (O*). Positive ions are accelerated away from the sample, toward the negatively biased top electrode. The bias direction during oxidation rules out ions as being the dominant species in the oxidation process. At pressures around 100 mTorr, the mean free path for O* atoms ($\approx$ 1 cm) is of the same order as the spacing between the plasma electrodes. O* particles

can transit, without undergoing collisions, to the aluminum surface.

Previous studies of both plasma and thermal oxidation point to aluminum as the moving species during oxidation [56, 64]. Aluminum in the film diffuses to the surface to react with the O* continuously supplied by the discharge. During this phase, oxide film thickness increases with increasing oxidation time. Eventually, all of the aluminum is consumed and oxygen atoms diffuse into the aluminum oxide matrix film [56]. The resulting amorphous aluminum oxide barrier is comprised of Al-O clusters where three- and four-coordinated aluminum atoms are the most energetically favorable structure [65, 66].

The oxide barriers shown in Fig. 2.11 were most likely created during the initial phase of plasma oxidation where the aluminum oxide thickness increases with increasing oxidation time. This leads to the exponential increase in device resistance with oxidation time shown in Fig. 2.11.

In Fig. 2.13 and Table 2.3, we observe that the barrier height at the bottom interface (ϕ_2) is greater than the top barrier height at the top interface (ϕ_1) for the shortest oxidation times. Increasing the oxidation time leads to more symmetric junctions, by increasing both ϕ_2 and ϕ_1. This behavior is in apparent contradiction to the assertion that Al as the moving species during plasma oxidation. Specifically, if the top of the barrier is oxidized first, one would expect the top of the barrier (ϕ_1) to be higher than bottom of the barrier (ϕ_2) for the shortest oxidation times.

This inconsistency can be resolved if we consider excess oxygen clusters to remain on the surface after oxidation. In this case, the excess oxygen clusters are absorbed by Co after deposition of the top electrode. The result is that an oxidized cobalt layer diminishes the barrier height at the top interface (ϕ_1) with respect to ϕ_2. Empirically, we have measured cobalt oxide to have a much smaller

tunnel barrier height than aluminum oxide. Another possibility is that O* diffuses through grain boundaries in the Al film and stops at the Al/Co interface, to efficiently oxidize the bottom of the barrier at early oxidation times.

2.5.0.2 Dusting layer

To gain more information about junction barrier height asymmetries, samples were prepared with a very thin "dusting" layer of aluminum deposited onto the aluminum oxide, immediately after plasma oxidation. If excess oxygen clusters were present on the surface, we expect these to react with the excess aluminum from the dusting layer causing a dramatic change in the fit parameters yielded by Chow's model. Nominal layer structure was chosen for these devices, with barriers formed in a 120 mTorr DC plasma (15 W), for an oxidation time of 5.0 s. The results are shown in Fig. 2.15 and fit parameters are shown in Table 2.4. Two different thicknesses of dusting layers were applied 2 Å (b) and 4 Å (c). At the top, in Fig. 2.15(a) is, the dI/dV with no dusting layer. In (a), as expected, the minimum of the conductance parabola occurs at a negative bias. This corresponds to the same direction and magnitude ($\phi_1 < \phi_2$) of asymmetry as previously discussed (positive bias must be applied the bottom electrode in order to measure at the conductance minimum).

In Fig. 2.15, the minimum conductance value is indicated in (a), (b) and (c). As the dusting layer thickness increases, the position of the conductance minimum shifts to more positive bias voltages, *i.e.*, the barrier heights become more symmetric. Both barrier heights decrease after deposition of a dusting layer. However, the fits shown in Table 2.4 for the devices with 2 and 4 Å dusting layers yield unphysical parameters. In particular, both the 2 and 4 Å dusting layers nearly double the extracted barrier thickness. The uncertainties expressed

Sample name	t_{ox} (s)	s (Å)	ϕ_1 (eV)	ϕ_2 (eV)	R_0 (Ω)	A (μm^2)	dusting layer (Å)
110824-06B	5.0	17.03 ± 0.03	0.841 ± 0.003	0.938 ± 0.004	673.5	938	none
110824-11A	5.0	33.6 ± 0.3	0.184 ± 0.004	0.224 ± 0.004	913	870	2
110824-13C	5.0	27.0 ± 0.2	0.159 ± 0.003	0.190 ± 0.004	16.4	1044	4

Table 2.4: Parameters of I-V fits shown in Fig. 2.15 (Al dusting layer).

in Table 2.4 represent the standard errors of the fits.

Qualitatively, the dramatic change in extracted barrier thickness suggests that there are excess oxygen clusters at the surface, that react with aluminum in the dusting layer upon deposition. Excess aluminum at the top of the barrier provides a diffusion pathway for weakly bound oxygens in the film. Diffusion of oxygen out of the film and into the dusting layer would form a thicker barrier with a more uniform concentration of oxygen. However, the Chow model likely breaks down in this case because there is no abrupt interface between the top electrode and barrier. Thus, adding excess aluminum at the top of the barrier decreases both ϕ_1 and ϕ_2 and increases s, though the numerical values in Table 2.4 are questionable.

In a $Al/Al_2O_3/Co$ junction with sharp interfaces, one would expect to observe the asymmetry ($\phi_1 < \phi_2$), because the vacuum work function of Al is approximately 1 eV smaller than for cobalt. Floyd and Walmsley present an interesting study of asymmetry in barrier heights for the case of metal-insulator-metal tunneling structures with dissimilar electrodes [67, 68].

2.6 Chapter summary

In summary, this chapter presents an overview of the experimental apparatuses needed to grow tunnel junctions in UHV for the experiment with HCIs.

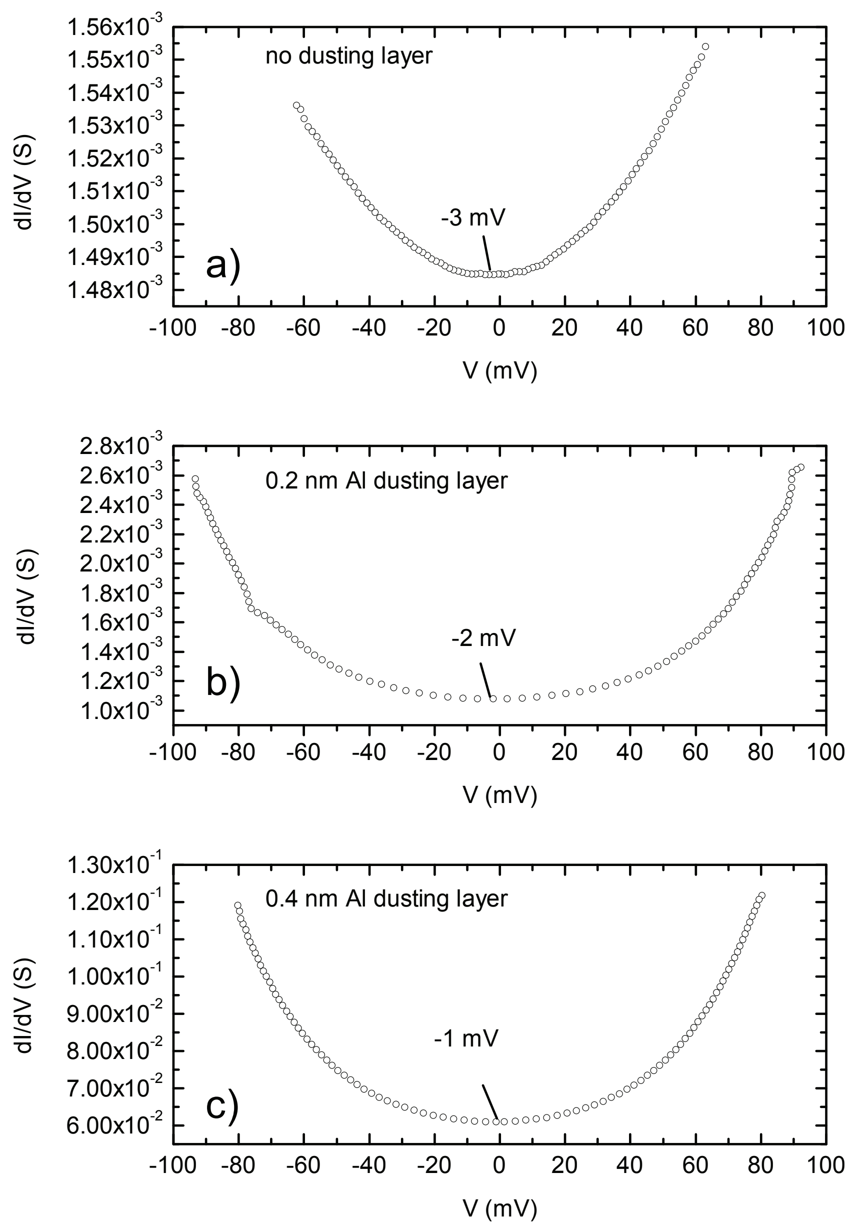

Figure 2.15: Comparison between pristine junction and junctions with a dusting layer. The position of the conductance minimum is indicated on each curve

The smaller G2 shadow masks allow measurement of lower RA devices, with a less initial error contribution from "negative resistance". Differential conductance measurements show the characteristics of good tunnel junctions as described by Rowell [59], with asymmetries about zero bias of a few mV about zero bias. The asymmetry ($\phi_1 > \phi_2$) present in almost all of the junctions can be fit with Chow's model. Increasing oxidation time, or adding a dusting layer, makes more symmetric barriers. An oxidation process consistent with the conductance data was described, where oxygen is the moving species. We found that oxidation time is the most critical parameter, in determining the final resistance of a tunnel junction. In fact, for the pressure-power parameters we used, barrier thickness increases linearly with plasma oxidation time. This leads to an exponential increase in device resistance.

Chapter 3

Measuring charge dependent HCI energy deposition with tunnel junctions

3.1 Overview

Data discussed in this chapter have previously been published in Refs. [1, 69]. The primary set of data discussed is composed of G1 devices (Fig. 2.3) dosed with Xe^{Q+} ($26 \leq Q \leq 44$). The objective of the experiment was to investigate charge state dependent surface modifications by HCI impacts. Ions were extracted at kinetic energies (KE) of approximately $(8 \times Q)$ keV.

At the end of the chapter, we present some measurements of G2 devices (Fig. 2.5) irradiated at a slightly lower extraction bias of 5 kV, giving projectiles KE of $(5 \times Q)$ keV. The primary purpose of lowering the kinetic energy was to investigate the stopping power enhancement predicted in Ref. [35]. Data analysis in Appendix E is shown for three of these devices.

In section 3.2, the beamline apparatus and experimental procedure is described. In section 3.3 tunnel junction conductance data as a function of dose and charge state are shown. Section 3.4 outlines the analysis used to determine the average conductance per ion impact [σ_c(Q)]. Sections 3.5 and 3.6 discuss the extraction of crater depths as well as extraction of crater formation energies. Finally, crater formation energy is partitioned into kinetic and potential contributions. Experimental data for G2 devices irradiated at < 8 kV extraction voltage are also shown. Section 3.7 provides a brief summary.

Throughout the chapter, "charge state" expresses the integer number of electrons Q stripped from the neutral atom, *i.e.*, the ionization state of the projectile. Therefore, the magnitude of charge (in SI units) that this quantity corresponds to would be Qe, where e is the elementary charge in Coulombs. Throughout the chapter, kinetic energy is expressed in terms of the EBIT extraction voltage and the charge of the ion as $KE = UQe$. Multiplying the charge of the ion Qe (in units of e) by the potential drop during ion extraction (in units of kV) gives the kinetic energy. For example, if an ion of charge state Q were extracted from the EBIT at electric potential U = 8 kV, it has kinetic energy $KE = (8 \times Q)$ keV.

3.2 Experiment

3.2.1 EBIT beam line

The NIST EBIT beam line is detailed in Refs. [7, 70]. A beam line schematic is shown in Fig. 3.1. The ions leave the EBIT vertically, extracted at an electric potential U toward the ceiling of the EBIT laboratory. One of the first elements in the beam line is an electrostatic bender that redirects the beam by 90° (first

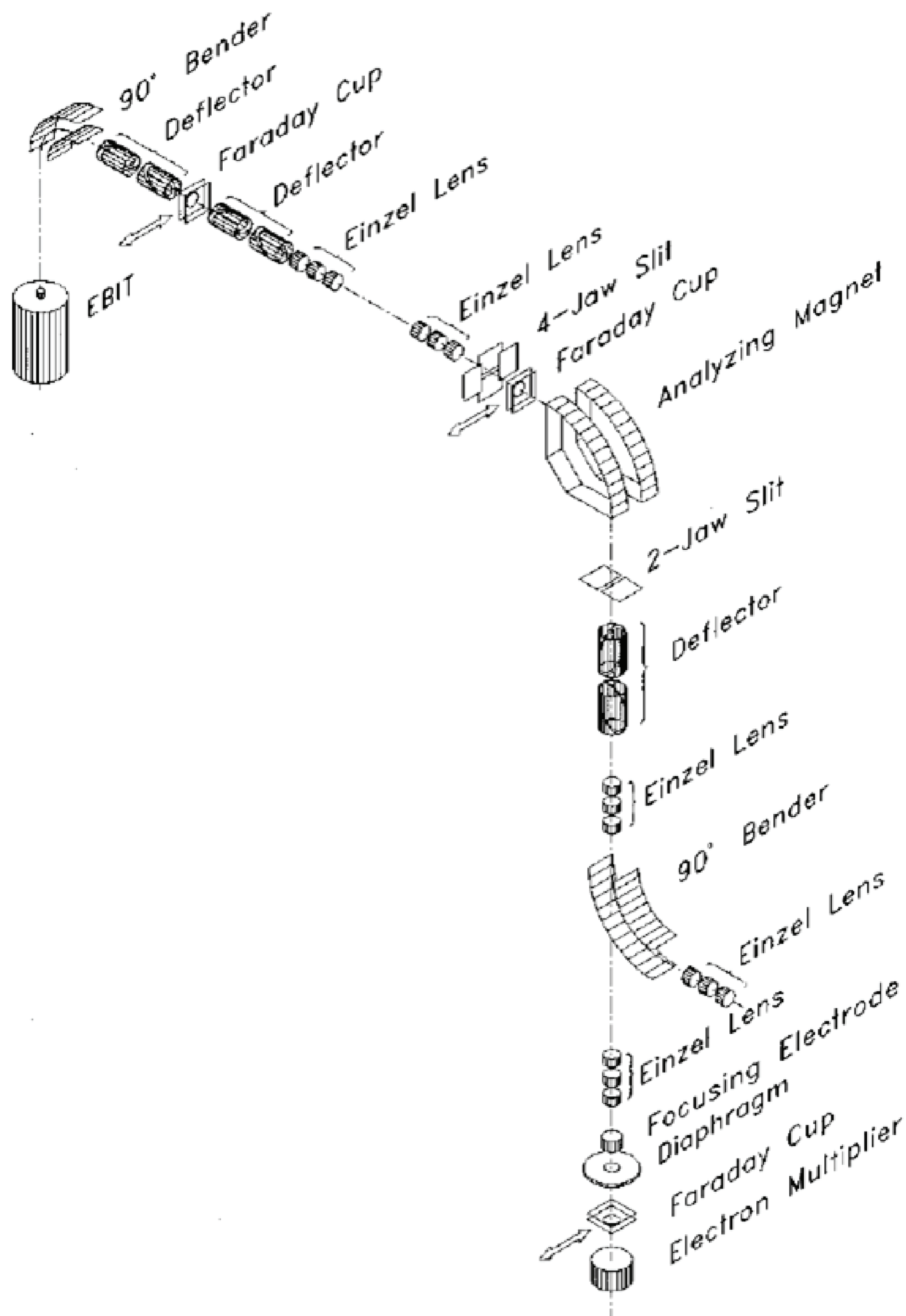

Figure 3.1: EBIT beamline schematic (from Ref. [7])

element after the EBIT in Fig. 3.1). Past the bender, two sets of electrostatic deflectors align and steer the beam. Einzel lenses focus the beam into a 4 jaw slit that defines the entrance of the analyzing magnet. Along the path of the beam Faraday cups (FC) can be inserted to monitor beam current. When the ions reach the analyzing magnet they are bent again into the 2-jaw slit, bringing the beam into the target chamber. Below the analyzing magnet, the beam is charge filtered. After passing through the analyzing magnet, the beam goes through an electrostatic deflector, and is focued by two sets of einzel lenses, before it impinges on the sample. A final FC measures beam current in the region where samples are irradiated. The final FC can be manually translated out of the way, so that a sample can be positioned in its place, during an exposure.

Ions of all charge states produced within the EBIT are extracted at a potential U, so that kinetic energy of the particles increases with charge state as $Qe \times U$. The fields within electrostatic lenses exert stronger forces on particles with higher charge state. However, the constant acceleration voltage means that the higher charge state projectiles have commensurately higher velocities as they enter these electrostatic elements. The result is that all charges are affected equally by the electric fields, and there can be no charge selection by deflectors or einzel lenses. This means that the various charge states in the beam are lensed equally by the electrostatic elements. As described above, the result is that upstream from the analyzing magnet, all charge states produced within the EBIT are present in the beam.

Unlike the electrostatic lens elements, the analyzing magnet can select particles by Q/m ratio. The magnetic field required to deflect an ion with a given

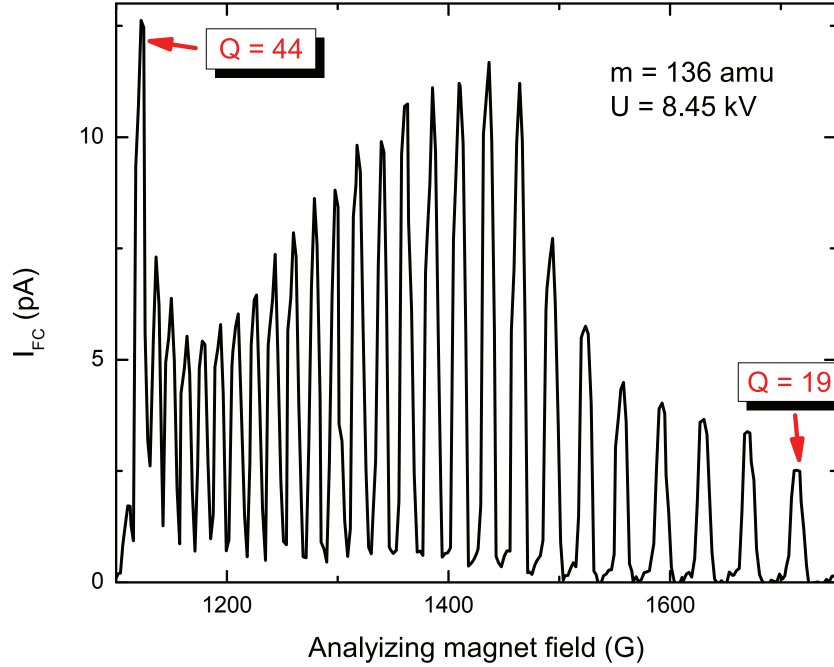

Figure 3.2: Current on Faraday cup while sweeping the analyzing magnet field. Peaks correspond to charge states of Xe^{Q+} for $Q = 44$ to $Q = 19$.

charge to mass ratio by 90° is

$$B \propto \frac{1}{R}\sqrt{\frac{2Um}{Qe}} \tag{3.1}$$

where, where R is the radius of the analyzing magnet (approximately 20 cm). Ions with the desired Q/m can be selected by changing B. Ions with a higher Q/m than the desired ratio will be over-steered $>90°$ into the walls of the beam line, and ions with lower charge to mass ratio will not make the 90° bend. Note that when changing the EBIT extraction voltage, the magnetic field must be scaled by $\sqrt{U}$, to obtain the same Q/m ratio after the analyzing magnet. Due to isotopic

(mass) variation of the ions in the beam, the Q/m ratio does not uniquely define the charge state. For example, $^{132}Xe^{44+}$ and $^{129}Xe^{43+}$ both have $Q/m = 1/3$. To increase selectivity of a particular charge state, a source gas enriched with a rare isotope (^{136}Xe) is used, *e.g.*, the ratio $Q/m < 1/3$ for $^{136}Xe^{44+}$ is distinguishable from the previous isotopes [7].

Figure 3.2 shows the current measured on the FC downstream from the analyzing magnet. As the magnetic field is swept, distinct peaks in the beam current appear. These correspond to the individual Q/m values within the beam. The magnet scan shows peaks corresponding to $^{136}Xe^{Q+}$ for the range $Q = 44$ to $Q = 19$. During an experiment, the magnet is set to a fixed value, *i.e.*, B = 1168 G for Xe^{44+}.

Below the final Faraday cup and sample position, a microchannel plate beam viewer (Colutron Research, model: BIS-1) is mounted at the bottom of the target chamber. The illumination area of the beam viewer is monitored by a camera directed toward the fiber optic vacuum feedthrough output of the beam viewer. This illumination area can be used to determine the shape of the beam incident on the sample, and is needed for a measurement of the transverse beam dimension. A measurement of the beam flux requires both the FC and beam viewer (discussed below).

3.2.2 Exposing samples to HCIs

3.2.2.1 Alignment

A camera mounted at the top of the target chamber (TC), looks down onto the sample. A halogen fiber light illuminates the sample through a viewport nearly parallel with the sample in the target chamber. The TC camera outputs

to a monitor that can also be toggled to display the beam viewer output signal. After the beam enters the target chamber, the display is set to the beam viewer output signal. A mark is drawn on the screen of the monitor at the center of the beam spot. The mark on the screen then provides a reference point between the beam viewer signal and TC camera outputs. After the mark is set, the TC camera view can be used to align individual devices on a chip with the center of the beam spot. The beam can be turned on or off (to start or stop a HCI exposure in the TC) by inserting or removing the pneumatic Faraday cup directly above the bending magnet, from the path of the beam (Fig. 3.1).

3.2.2.2 Determining the ion dose

Ion dose is calculated as follows. The total beam current (I_{FC}) is measured on the final FC. The beam viewer system is used to measure the shape of the beam, within the target chamber. The magnetic transfer rod in the LL is attached to an XYZ manipulator. The sample sled has two bored holes (approximately 1 cm in diameter) centered at the sample positions. Small elliptical pieces of stainless steel shim stock with drilled apertures (diameters $d = 0.689$ mm) are fit into each hole in the sample sled. HCIs emit a high yield of secondary electrons within the FC. This necessitates a negatively biased (-10 V) suppressor plate at the FC entrance, to improve the accuracy of the beam current measurement.

During the measurement procedure, the sample sled is translated so that the beam spot is visible in the beam viewer through the aperture. Then, the sample sled is translated in the X and Y directions (in the plane of the sample), to find the positions in the transverse beam direction where the beam is blocked. These positions correspond to x_1, x_2, y_1 and y_2.

Accounting for the diameter of the aperture itself, the transverse dimen-

sions of the beam are $r_1 = \Delta x - d$ and $r_2 = \Delta y - d$. The area of the approximately elliptical beam spot is $A_{spot} = \pi r_1 r_2$. If we assume that the charged particles in the beam are uniformly distributed within the radius of the beam (due to space charge interactions), the flux of incident ions is

$$F = \frac{I_{FC}}{QeA_{spot}}, \tag{3.2}$$

where Q is the charge state of an ion and e is an elementary charge. The total ion dose on each sample, N, depends linearly on the sample size A and dosing time t,

$$N = \frac{I_{FC}}{Qe}\frac{A}{A_{spot}}t. \tag{3.3}$$

A is determined from micrographs of the finished devices. In the exeriment $A/A_{spot} \approx 10^{-3}$ (for the G2 devices). Numerical values in Eq. 3.3 depend on EBIT parameters, beam tuning and charge state. However in normal operation for Xe^{44+}, $I \approx 5$ pA, $A_{spot} \approx 1$ mm^2, $A \approx 10^3 \mu m^2$ (for the G2 mask set). Within one minute of exposure, a dose of order 10^5 HCIs impacts the sample.

3.3 Data

Tunnel junctions were prepared with the G1 mask set (4 devices on each chip) as described in Ch. 2. The bottom electrodes [2 Co+Ox/21 Co] and tunnel barrier [1.1 Al+Ox] were formed first, for eight chips. HCI irradiation typically occurred >24 hours after oxidation of the Al layer. The tunnel junction devices were prepared and irradiated entirely *in situ* with base vacuum pressure 10^{-10} Torr. Each tunnel junction device was grown on a Si oxide substrate with the layer

structure (in nm): bottom contact and anti-ferromagnet pinned layer [2 Co+Ox/21 Co], tunnel barrier [1.1 Al+Ox], magnetic free layer and top contact [10 Co/40 Cu/3 Au]. All layers were deposited by electron beam evaporation where +Ox indicates exposure to oxygen plasma after growth. Shadow masks were used to define the sizes and positions of the thin film electrodes so that each Si oxide chip had 4 devices arranged in crossed wire geometry. After plasma oxidation the Al expands to thickness $s_0 = (14 \pm 1)$ Å [47, 56].

As a control, one device per chip was left unirradiated. Charge filtered Xe^{Q+} were extracted for $26 \leq Q \leq 44$ with kinetic energy $E = 8$ keV $\times$ Q onto the Al_2O_3 barriers near normal incidence. Subsequently the magnetic free layer and top contact were deposited onto the irradiated surface. When devices were completed, the area ($\approx 10^4 \mu m^2$) of each was measured with optical microscopy. Four-point probe differential resistance measurements were obtained at low bias and corrected for the negative resistance artifacts [57]. The inverse of the corrected resistance measurement is then device conductance $G = R_{dev}^{-1}$.

The time between irradiation and deposition of the top electrode does not critically influence either the control or irradiated devices, as long as the devices are kept in ultrahigh vacuum. For capping times between 15 min and 70 hr at 1×10^{-10} Torr, we found no systemic change in the irradiated or unirradiated device conductance. However, exposure of a chip to air will increase the resistance of both the control and irradiated devices by approximately an order of magnitude and make the influence of the highly charged ions unmeasurable.

Figure 3.3(a) depicts a schematic representation of the experiment. In Fig. 3.3(b) we show the conductance of many devices as a function of ion dose for representative charge states $Q = 34, 40, 44$. These chips were grown with the G1 mask set. The devices in Fig. 3.3(b) were dosed with ions extracted at 8 kV,

(kinetic energy: 8 keV $\times Q$). Each point is the conductance of one tunnel junction modified by N discrete ion impact sites. G increases linearly as a function of ion dose and each ion creates an individual feature in the barrier during irradiation. We model the increase in conductance, for a particular charge state, due to individual ion impacts with the equation,

$$G(N) = G_i + \sigma_c N \tag{3.4}$$

where G is the conductance of an irradiated device, G_i is the conductance of the device with a pristine barrier as determined from the unirradiated control device, σ_c is the slope of the conductance increase, and N is the ion dose. In the low dose regime, σ_c is expected to be independent of N and represents a statistical average for the conductance through each defect formed by a HCI. Ion impact sites increase the conductance of the tunnel junctions and the goodness of the linear fits to $G(N)$ is noteworthy. Linearity in $G(N)$ implies an approximate one-to-one mapping between ion dose and the formation of localized surface modifications.

Figure 3.4 shows dI/dV data for an irradiated and unirradiated device. Parameters of the HCI dose are given in the caption. Note that the polarity of the leads has been switched, with respect to the plots in the previous Chapter. In Fig. 3.4, positive bias causes electrons to tunnel to the bottom electrode. Therefore, the asymmetry of barrier heights has the same behavior as previously discussed, but appears reversed from Fig. 2.13. For HCI irradiated tunnel junctions, The fit parameters for the unirradiated device was, $s = 16.0$, $\phi_1 = 0.97$ eV, $\phi_2 = 0.76$ eV. For the device dosed with Q = 32 ions, $s = 14.7$, $\phi_1 = 1.02$ eV, $\phi_2 = 0.83$ eV. Further discussion of dI/dV spectra of irradiated junctions can be found in Ref. [48].

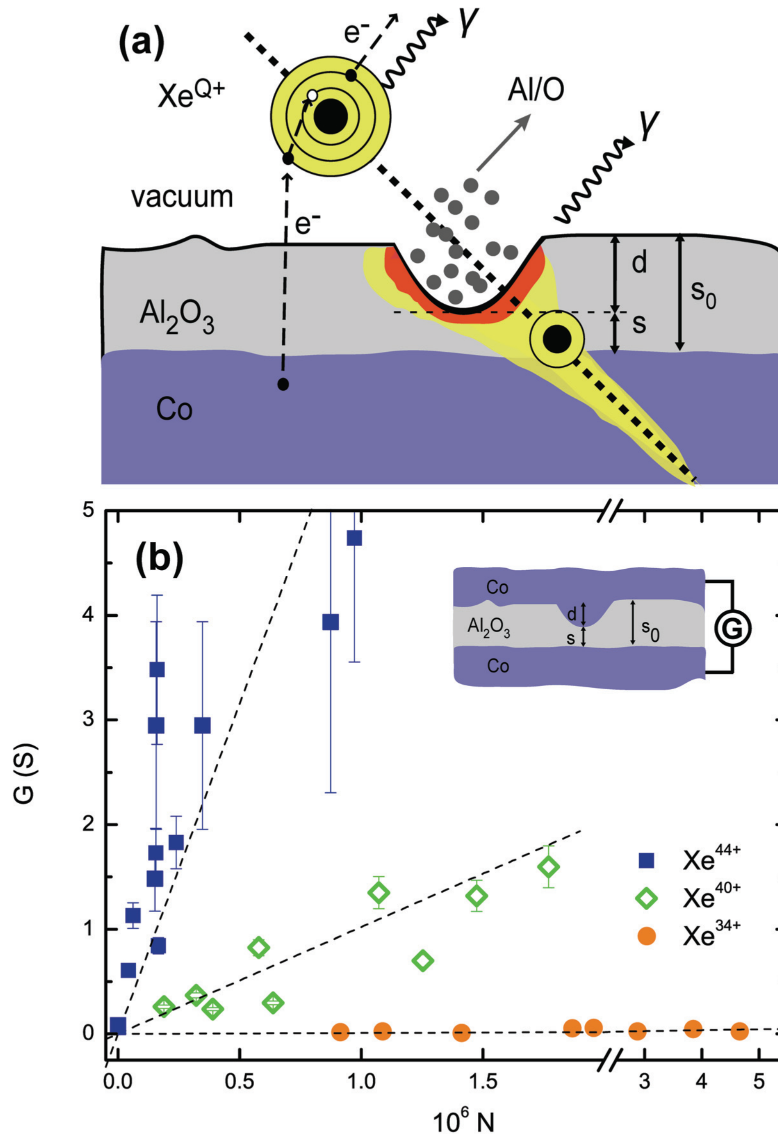

Figure 3.3: (a) Schematic representation of neutralization and heated spike formation scenario for relaxation of a HCI above a metal surface covered with a thin dielectric film [23, 71]. The heated spike leading to crater formation occurs during sub-surface neutralization. (b) Electrical conductance of a tunnel junction increases linearly with the number of ion impacts. The slope of each line (σ_c) increases with increasing Q [1].

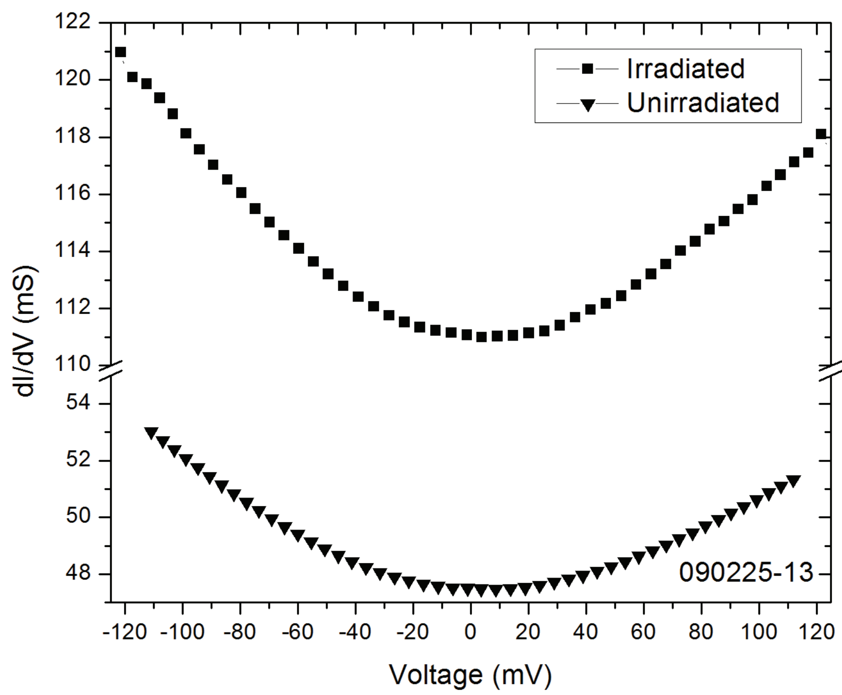

Figure 3.4: dI/dV curves for both irradiated and unirradiated devices. For the irradiated device: G1 masks, Xe^{32+}, $N \approx 10^7$ ions [69].

The data in Fig. 3.4 are typical for a device that has been irradiated. We find that dI/dV measurements of irradiated devices indicate that impacts do not cause a significant decrease in barrier height ϕ [44]. Qualitatively, the conductance maintains the same parabolic shape, before and after irradiation. Tunneling remains the dominant transport mechanism, within the irradiated junctions in Fig. 3.4. Irradiated junctions also maintain insulator-like resistance dependence on temperature [33].

The unirradiated barrier thickness $s_0 = 1.4$ nm agrees with the expected value for the stoichiometric expansion of a 1.1 nm aluminum film (Al $\rightarrow$ Al_2O_3). The assigned uncertainty in s_0 of ± 0.1 nm reflects the measurement accuracy of the initial thickness of the Al film, as measured by the QCM. To confirm s_0, transmission electron micrographs were obtained [46]. Additionally, the extracted fit parameters of dI/dV were consistent with the s_0 measurements.

3.3.1 Statistics of defect formation

One reason that Eq. 3.4 is a good description of the $G(N)$ data is because of the relatively low ion doses used in this experiment. For example, a dose of 3×10^5 ions on the G1 devices corresponds to an areal number density of about 1 per (100 nm)^2. Deviation from linear behavior could be expected for very high fluxes or long exposure times, where the radii r of the surface defects would overlap. We can approximate the onset of the nonlinear regime, using the statistical analysis from Ref. [72], which assumes that the ion irradiation is a Poisson process.

In the model, the ion impact sites are Poisson distributed within the device area A. Above a certain dose threshold, the probability that the entire surface area

is irradiated, approaches unity. In this high dose regime, increasing the dose does not lead to the formation of "new" surface modifications. Instead, new impact sites overlap with the previous impact sites.

Following the approach from Ref. [72], we can determine the dose regime where the number of distinct surface modifications increases linearly with the total ion dose. The number of distinct ion impacts sites within the area A depends on dose N as,

$$N_f = \frac{A}{\pi r^2}\{1 - \exp[-\pi r^2 (N/A)]\} \tag{3.5}$$

where r is the average radius of a defect. The results are plotted in Fig. 3.5. The solid (blue) line plots the model derived from Poisson statistics, in Eq. 3.5. The dashed (black) line plots the equation $N_f = N$, *i.e.*, each ion creates exactly one distinct modification. For the calculation shown in the figure, the radius of a defect was set to $r = 3$ nm, and the area was set to $A = 30 \times 30$ μm^2 (the approximate size of a device fabricated with the G2 mask set).

With these parameters, the Poisson model predicts that below $N \approx 10^7$, it is reasonable to assume that the number of individual surface modifications increases linearly with the ion dose. Above this threshold, the probability that an ion will impact an already irradiated area of the sample increases substantially. At very high doses, $\approx 10^8$ ions, the entire area of the sample has been irradiated. The ion impact sites overlap, and increasing the dose does not increase the irradiated area. In practice, this high flux regime could not be measured on a $G(N)$ plot, because the devices would have an immeasurably low resistance (high conductance). The non-linear threshold is at even greater N value for the G1 devices, because of their large area – all of the $G(N)$ data discussed in this thesis, are in the low N, linear regime.

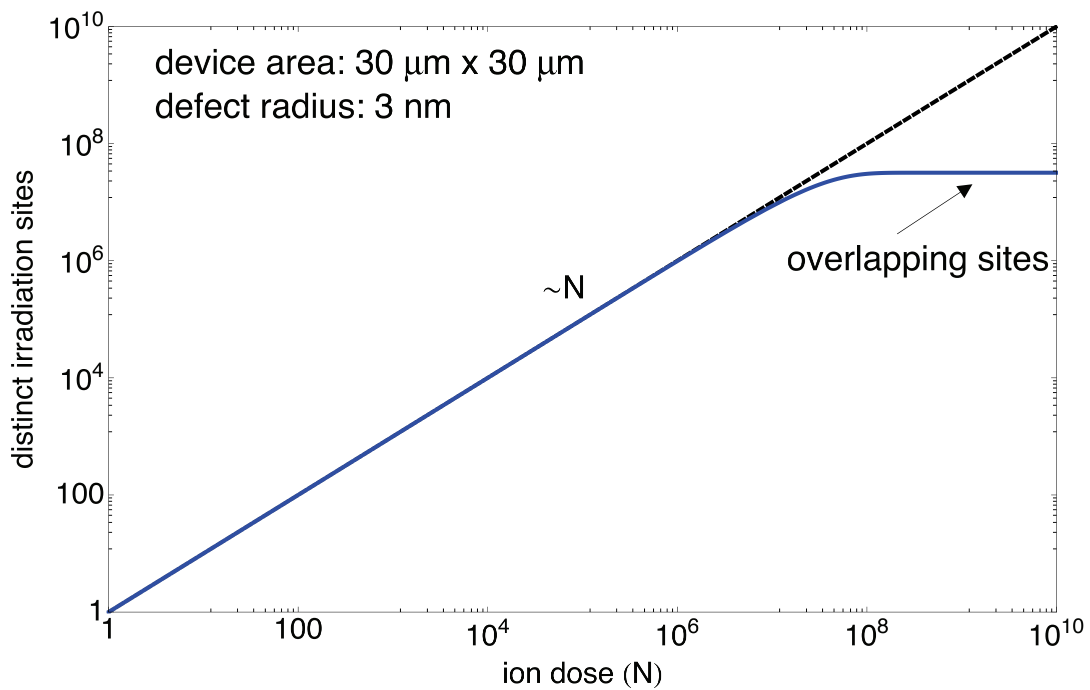

Figure 3.5: Model based on Poisson statistics for the number of distinct features created in the barrier with increasing ion dose. At low doses the number of features scales with N. At high doses, the features overlap.

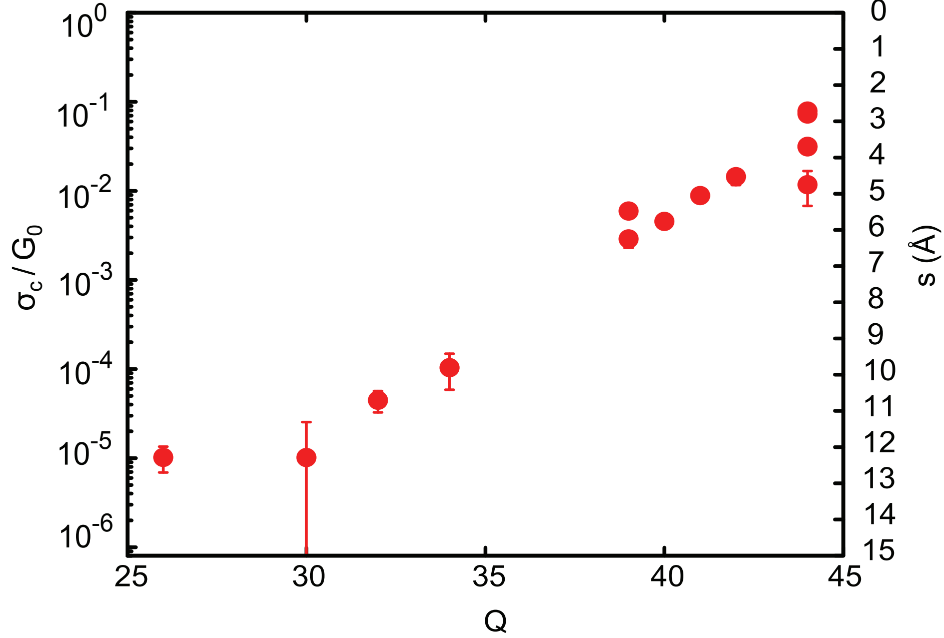

Figure 3.6: $\sigma_c(Q)$ increases by four orders of magnitude for charge states between $Q = 26$ and $Q = 44$. Electrical conductance of each ion impact site increases due to a decease in barrier thickness after charge-dependent crater formation. Right axis displays the barrier thickness s corresponding to each conductance value.

3.4 Analysis

3.4.1 Extracting of σ_c and uncertainties

The data shown in Fig. 3.6 were analyzed in the following way. A σ_c measurement can be extracted from each device. By rearranging Eq. 3.4 and expressing the results in terms of measured resistances, we write

$$\sigma_c = \frac{1}{N}\left(\frac{1}{R_{dev}} - \frac{A}{R_0 A}\right). \tag{3.6}$$

The number of ions incident on each device was determined with Eq. 3.3. The first term in Eq. 3.6 is derived from the corrected resistance measurement

of the device. The second term in Eq. 3.6 is device conductance due to the estimated conductance of an unirradiated device. This estimated initial conductance ($G_i = R_0^{-1}$) is derived from the measurement of the on-chip control device, and a pattern correction function that accounts for systematic variations in resistance between the devices on a single chip. For the G1 devices, on-chip control was the D device, while for the G2 devices A, F and H were left unirradiated as the on-chip control devices. The difference between the first and second term in Eq. 3.6 divided by the number of ion impacts represents the average conductance increase per ion. Propagation of error in σ_c can be computed directly from the function Eq. 3.6, if uncertainties in N, R_{dev}, A and R_0 are quantified. Within Fig. 3.6, error bars correspond to experimental uncertainty on the normalized conductance (left) axis.

3.4.1.1 Device resistance, R_{dev}

Using the correction procedure in Eq. 2.2, the corrected resistance R_{dev} was obtained. The procedure requires resistance measurements of a device with no barrier (ΔR_0), and measurements of the $R_\square$ resistances for the top and bottom electrodes. The square resistance of a thin film wire is defined as the resistance of the wire times normalized by the number of "squares" in the wire $R_\square = (w/l)R$, where l and w are the length and width of the wire. Two thin films with identical resistivity and thickness, will have the same $R_\square$ regardless of area. The G2 masks produce on-chip test patterns for measuring $R_\square$ with four probes.

In order to correct for the "negative resistance" error [57], spatial measurements of the wires are required. Optical micrographs of each chip were recorded and analyzed by plotting line profiles perpendicular to the wires. The profiles were then fit with Gauss error functions to quantify the width between the steps,

and the width of the step edges themselves. The procedure for fitting the line profiles is shown in Appendix D.

3.4.1.2 Pattern correction (determining the initial resistance, R_0)

Ideally, each device on a chip would have exactly the same resistance (or resistance-area product). The ability to determine the conductance added to a device by the ion impacts requires knowing the starting resistance. In reality, not all devices on a chip have the same resistance. There is typically a systematic resistance pattern. This pattern is likely caused by spatial variations in the plasma intensity over the area of the chip during the oxide formation. The pattern is also determined by the exact position of the chip during plasma oxidation. Additionally, small variations in the sizes (A) of the devices can cause the initial resistances of the devices to vary (<10 %) on a chip. The area depends on the relative alignment of the tunnel junction wires, and the position of the mask with respect to the chip during deposition.

Unirradiated chips that were fabricated immediately prior to the EBIT run allow us to measure systematic resistance variations between the unirradiated devices on a single chip. An example of the systematic resistance variation is shown in Fig. 3.7 for devices grown with the G2 masks.

Barriers of the devices in the figure were produced in a plasma with parameters $t = 3.3$ s, P = 21 W, 120 mTorr. For the devices `111221-7`, `111221-8`, `111221-9` and `111221-10` in Fig. 3.7, there was a linear increase in resistance from A to F and a linear decrease from F to H. The vertical axis is the device resistance divided by the on-chip resistance of the F device. The systematic resistance change for the devices across a single chip is well described by two lines with different slopes. A positive slope describes A-F, while a negative slope describes

F-H. The dashed purple lines are a fit to the normalized resistance trend for chip 9. The blue lines show a similar fit, for devices on chip 8. The resistance of device H on chip 10, clearly lies outside the trend $(R_H \gg R_F)$, and can be ignored for the estimation of B, C, D, E and G.

This pattern was observed in many chips prior to the EBIT run. During the run, only devices B, C, D, E, G were dosed with HCIs, leaving A, F, H as unirradiated control devices. Then, the resistance slope between A and F and the slope between F and H could be used to estimate the initial device resistances for B, C, D, E and G, before the irradiation. With a measurement of the resistances of A and F, the resistances of B, C, D, E and G can be estimated. For example on 9C, measurement of only A and F constrain $R_C/R_F = 0.69 \pm 0.09$ with 95 % confidence. Therefore, even if C had been irradiated by highly charged ions, its original value before the irradiation could have been interpolated with acceptable accuracy.

The normalized resistances on chips 7, 9, 10 are grouped closely together while, for chip 8 the A-F resistances have a different slope. From this observation, we conclude that the angular alignment during plasma oxidation was different between chips 7, 9, 10 and chip 8. However, all resistance values can be estimated accurately because of the reproducibility of the linear resistance variation. Even if the systematic resistance pattern were left uncorrected, the variation in the initial resistances shown in Fig. 3.7 would not introduce unacceptable error into a measurement of HCI induced conductance. Since conductance is the inverse of resistance, small fluctuations in the initial resistance of undosed devices result in negligibly small fluctuations in the initial conductance. Therefore, increased conductance induced by the HCIs can be measured even in a case where there is a large (*e.g.* factor of 2) systematic variation in the initial resistances across a chip.

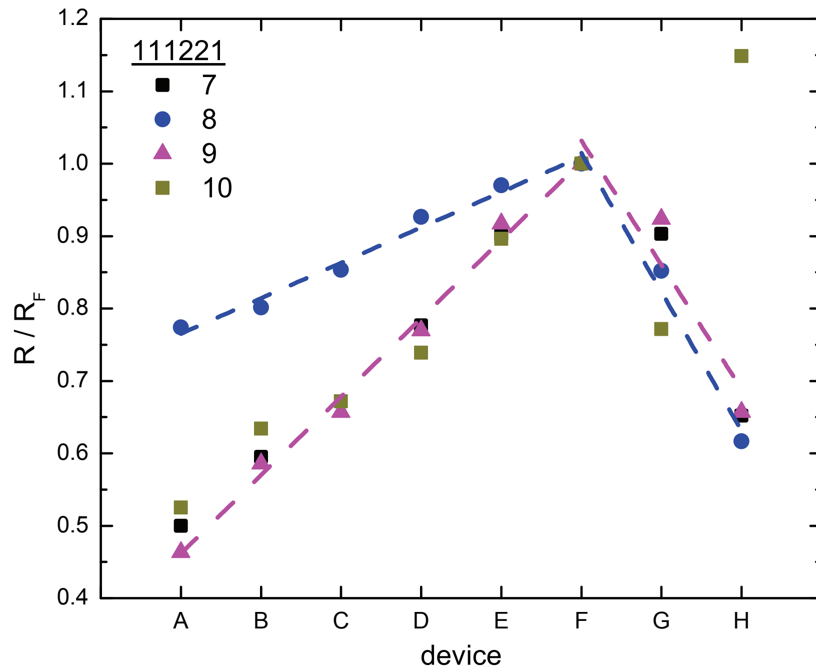

Figure 3.7: Normalized resistances on four unirradiated control chips grown with G2 masks. The dashed lines show the systematic-linear resistance patterns for chips `111221-08` and `111221-09`.

This remains true as long as the initial device resistances are large with respect to the final resistance of the HCI dosed devices. As described in Ch. 2, devices with higher starting resistance provide more dynamic range in the experiment.

3.4.1.3 Uncertainty analysis

In order to propagate error in σ_c, we substitute N from Eq. 3.3 into Eq. 3.6, and simplify the result:

$$\sigma_c = \frac{QeA_{spot}}{I_{FC}At}\left(\frac{1}{R_{dev}} - \frac{1}{R_0}\right). \tag{3.7}$$

Error propagation is carried out from Eq. 3.7 as,

$$\Delta\sigma_c = \Big[(\partial_{A_{spot}}\sigma_c)^2(\Delta A_{spot})^2 + (\partial_A\sigma_c)^2(\Delta A)^2 + (\partial_t\sigma_c)^2(\Delta t)^2 + (\partial_{I_{FC}}\sigma_c)^2(\Delta I_{FC})^2 + (\partial_{R_0}\sigma_c)^2(\Delta R_0)^2 + (\partial_{R_{dev}}\sigma_c)^2(\Delta R_{dev})^2\Big]^{1/2} \tag{3.8}$$

Here, ∂_x refers to the partial derivative with respect to an independent variable x within Eq. 3.7, and Δx is the experimental uncertainty in that quantity. Using Eqs. 3.8 and 3.7, σ_c is extracted for each irradiated device. Thus, we have a measurement and uncertainty value for σ_c from irradiated device at a given charge state.

From measurements of σ_c on n different devices, we find the most probable value of σ_C, by instrumentally weighting the measurements according to their uncertainties [38]:

$$\bar{\sigma}_c(Q) = \frac{\sum_{i=1}^{n}\sigma_{ci}/\Delta\sigma_{ci}^2}{\sum_{i=1}^{n}1/\Delta\sigma_{ci}^2} \tag{3.9}$$

The accompanying uncertainty (variance of the weighted mean) for $\bar{\sigma}_c(Q)$ is

$$\Delta\bar{\sigma}_c(Q) = \left[\sum_{i=1}^{n} \frac{1}{\Delta\sigma_{ci}^2}\right]^{-1}. \tag{3.10}$$

Uncertainty in I_{FC} arises because the beam current can change gradually during an exposure. The beam current (I_{FC}) is measured before and after the devices on a chip are dosed with HCIs. The uncertainty in the beam current is the average of these measurements and is typically ΔI_{FC} = 0.1 pA. We assign Δt = 1 s uncertainty to the HCI exposure interval, which is timed manually with a stopwatch. Uncertainty in device area A arises from the sloped edge of the tunnel junction wires (see Appendix D), and the accuracy of the microscope length measurement calibration. A conservative estimate for this uncertainty is $\Delta A/A$ = 20 %. The pattern correction function (*e.g.* the lines in Fig. 3.7) can be used to determine the uncertainty in the initial device resistance before irradiation. The accuracy of the measured device resistance can be established within $\Delta R = 0.1\ \Omega$, after the "negative resistance" correction [57]. In addition to the terms written explicitly in Eq. 3.8, a dose uncertainty term ΔN is added in quadrature to account for the possibility of non-uniformity of flux within the beam spot. This correction has relative magnitude $\Delta N/N$ = 10 %. An example of the full uncertainty analysis, is shown in the tables in Appendix E, for three chips of type G2.

3.5 Results

3.5.1 Conductance through the impact sites

As indicated by the representative data in Fig. 3.3(b) and Fig. 3.16, σ_c is always positive. The left axis in Fig. 3.6 displays σ_c values for charge states

$26 \leq Q \leq 44$ at 8 kV extraction. As discussed below, the increase in conductance is due to a reduction of the barrier thickness through charge-dependent cratering. In some cases, the experimental uncertainty expressed by the error bars is smaller than the symbol size. We describe the decreased barrier thickness $s(Q) = s_0 - d$ as a function of ion charge state Q, where s is the barrier thickness at the bottom of a crater after a Xe^{Q+} impact, s_0 is the initial barrier thickness and d is the depth of a crater (Fig. 3.3). The craters subsequently become filled with the Co of the top electrode during completion of the device.

Each defect forms a distinct channel of increased conductance within the barrier. As barrier thickness within the channel decreases toward zero $(d \approx s_0; s \approx 0)$, the conductance should vary smoothly from the tunneling regime to the metallic point contact regime [73, 74]. As s decreases, conductance through the channel will increase exponentially, and then saturate at approximately a quantum of conductance, G_0.

In general, the conductance through a single narrow channel is one conductance quantum (G_0) times the probability that an electron will be transmitted through the channel [73, 74, 75]. In the case of tunneling, the transmission probability is $\exp[-s\beta\sqrt{\phi}]$. Therefore, we model the conductance through each ion impact site as $\sigma_c = G_0 \exp[-s\sqrt{\phi}\beta]$ and invert the equation to find s in terms of the measured conductance values using Eq. 3.11. This expression avoids the unphysical divergence present in Eq. 2.11, in the limit of $s \rightarrow 0$. In the tunneling regime, conductance of each crater depends exponentially on the barrier thickness as,

$$\sigma_{\rm c}(s) \simeq G_0 \exp[-\beta\sqrt{\phi}s], \tag{3.11}$$

where $G_0 = 2e^2/h \approx 77.5$ μS and $\beta \approx 1.025$ Å^{-1}eV$^{-1/2}$. Electric current flows

through the thinnest parts of the barrier. This means that transmission through a crater is highly localized to the bottommost point of each crater. Tunneling amplitudes through regions surrounding the bottom of the crater are exponentially suppressed. Instead of the "width" or "area" the appropriate quantity to describe the absolute magnitude of conductance through such a narrow channel is the conductance quantum G_0, that appears in Eq. 3.11.

From Eq. 3.11, s can be expressed in terms of the measured tunnel conductance through each ion impact site,

$$s(\sigma_c) \simeq -\frac{1}{\beta\sqrt{\phi}} \ln\left[\sigma_c / G_0\right]. \tag{3.12}$$

In the limit that s approaches the thickness of a single atom $(d \approx s_0)$, conductance through the crater saturates at G_0 and the site behaves as a quantum point contact. The four decade span of $\sigma_c(Q)$ with no saturation in conductance demonstrates that charge state dependent cratering decreases the barrier thickness and drives a tunneling conductance increase. Additionally, all magnitudes of σ_c shown in Fig. 3.6 are below the typical conductance thresholds for the onset of metallic transport through a narrow channel [73, 74].

3.5.2 Craters versus hillocks

Scanning probe measurements of slow HCI impacts on some insulators have revealed topographically raised "hillock" features [40, 41]. However, any explanation of our conductance data (*e.g.* Fig. 3.6) requires that the ions form areas of reduced thickness within the aluminum oxide film (craters). In theory, the tunnel junction conductance data do not exclude "hillocks" from coexisting with the craters. The tunnel junction measurement is sensitive to the formation

of lowered as opposed to raised regions, because electric current in the tunnel junction flows preferentially through the thinnest parts of the barrier. An increase in thickness at localized areas of the barrier is not detectable.

One possibility is that the “hillocks” measured by other groups are the same features that we measure embedded within the tunnel junctions. In this scenario, the hillocks are composed of agglomerations of atomic defects, that become filled with cobalt from the top electrode, to increase tunneling efficiency at each ion impact site. This possibility would result in an increase in the tunnel junction conductance. However, the means of the conductance increase would be different than crater formation. Defect agglomerations within the barrier would increase the number of defect states within the energy gap of the aluminum oxide, to effectively reduce ϕ. Increase in the conductance by reduction of barrier height (ϕ) is distinguishable from a reduction of (s) because of its separate power law (exp$[\phi^{1/2}]$ versus exp$[s^{-1}]$). In our measurements, irradiated devices maintain $\phi \approx 1$ eV.

In our devices, there is no measurable lowering of ϕ after HCI irradiation [48]. On the other hand, there is always a reduction in s. We interpret a crater as a volume at the surface where material has been ejected to the vacuum so that all of the removed atoms are replaced by vacancies. This type of “pit”, “crater”, or “caldera” formation has also recently been observed with scanning probes on KBr [41], Si[76], and TiO_2 [77] target materials.

3.5.3 Crater depths

Using Eq. 3.11, the barrier thickness that corresponds to each measured σ_c value is extracted. These values are included as a linear scale along the right

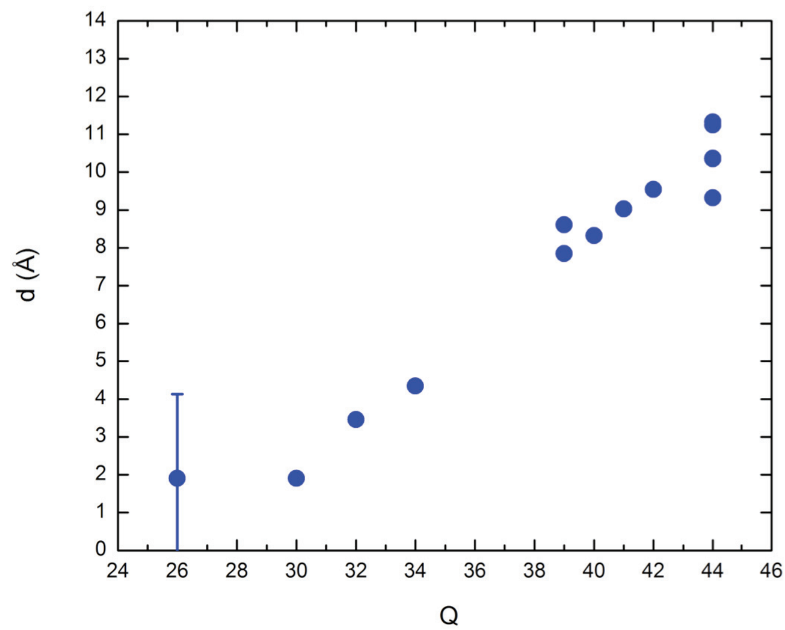

Figure 3.8: The average crater depth grows from 2 Å to 11 Å as charge state increases from $Q = 26$ to $Q = 44$, (kinetic energy $[8 \times Q]$ keV).

vertical axis of Fig. 3.6, with s decreasing from 12 Å to 3 Å as Q is increased from 26 to 44. This decrease in barrier thickness represents Q-dependent crater formation and we obtain the crater depth d as the difference between s_0 and s at each at each ion impact site. The range of crater depths obtained is 2 Å to 11 Å (Fig. 3.8).

Formation of a crater implies the removal of material. In some sense, measuring crater depth is an inverse measurement of the particles removed by potential energy sputtering. We find that our crater depths are consistent with sputter yields on other insulators [8]. Figure 3.9, compiles potential energy induced sputter yields reported for CsI, LiF, SiO_2, UO_2 and GaAs targets. The Al_2O_3 points (extrapolated from the conductance data in Fig. 3.6), are superimposed as red stars (charge states Q = 26, 36, 44).

In order to make a comparison between the tunnel junction and sputter yield measurements, the following assumptions were made. First, the shape of the craters is hemispherical with volume $V = (2/3)\pi d^3$, where $d = s_0 - s$. Also, the atomic density of the aluminum oxide was taken as the bulk, stoichiometric value of 11.7 $\times 10^{22}$ atoms cm^{-3} and aluminum and oxygen atoms are removed at the same rate. The extrapolated sputter yield data follow the trend of the measured potential sputtering data, and agree within an order of magnitude. At $Q = 44$ (51 keV of potential energy), around 300 atoms are removed. Kinetic energy between the data sets was varied, but is on the order of 10^2 keV (see Ref. [8] for details). From this comparison we conclude that our conductance data are in qualitative agreement with sputter yield measurements with HCIs.

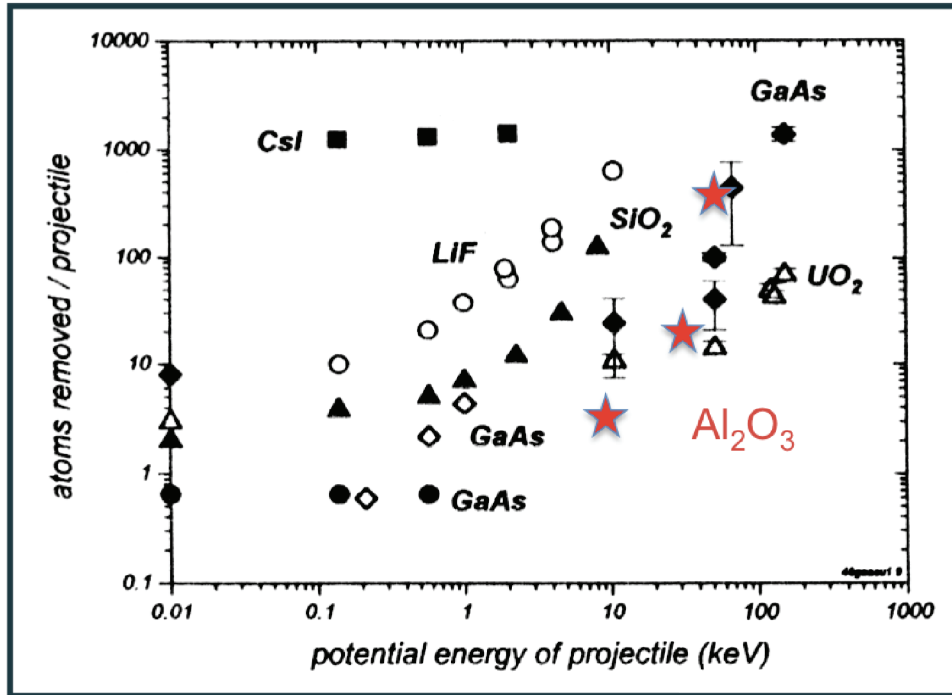

Figure 3.9: Comparison with sputter yield from Ref. [8]

3.6 Discussion

3.6.1 Heated Spike Model

3.6.2 Crater depth from the heated spike model

Using the heated spike model from Sigmund [78, 79, 80, 81], we can derive an expression for crater depth as a function of crater formation energy. Each measurement of the decrease in barrier thickness within Fig. 3.6 can be mapped to a charge-dependent crater formation energy $E_{dep}(Q)$.

Within the model, $E_{dep}(Q)$ is necessarily less than the total energy deposition. $E_{dep}(Q)$ represents a fraction of the total deposition that goes into the formation of the "crater" defect. Deposited energy can also contribute to sub-threshold heating of the lattice that does not lead to the formation of defects.

Additionally, the energy deposited into an insulator cannot be converted to heat with perfect efficiency [78].

Within the heated spike model, the ion collision forms a non-equilibrium temperature profile that cools simultaneously through heat conduction to the solid and evaporative heat loss. In particular, it is the temperature dependent evaporation of near-surface atoms from the semi-infinite cylindrical spike around a projectile's trajectory which gives rise to crater formation. After cooling, the final depth of a given crater can be expressed as

$$d(E_{\mathrm{dep}}) = \frac{\eta E_{\mathrm{dep}}(kT_0)^{1/2}}{Us_0} \exp[-U/(kT_0)], \tag{3.13}$$

where k is the Boltzmann constant, E_{dep} is the total energy deposited in the length s_0, $\eta = k(4\sqrt{2}\pi^{3/2}M^{1/2}\Lambda)^{-1}$ (Λ is the thermal conductivity of the target and M is the mass of a target atom), T_0 is the initial temperature of the spike and U is the surface binding energy per evaporated atom. The heated spike has initial thermal energy $kT_0 = (2/3)E_{dep}$ [79]. In applying this model to high Q projectiles, both sub-surface neutralization (potential) energy deposition and pre-equilibrium nuclear and electronic stopping contribute to spike formation.

Within the heated spike model, we consider heat dissipation through conduction to occur primarily through the Co layer, given its high thermal conductivity compared to the Al_2O_3 thin film. Therefore the thermal conductivity was taken to be the nominal value for Co of $\Lambda = 100$ W K^{-1} m^{-1} [82]. The target mass M was a weighted average between the masses of the Al and O species in stoichiometric Al_2O_3, and the surface binding energy was set at the experimentally determined aluminum displacement threshold of 20 eV [83]. Eqs. 3.12 and (3.13) are connected by the unperturbed barrier thickness s_0 as, $s(\sigma_{\mathrm{c}}) + d(E_{\mathrm{dep}}) = s_0$.

For each charge state, E_{dep} was obtained using the measured σ_{c} value as shown in Fig. 3.15 (discussed below). For the spike parameters described here, we find that E_{dep} increases from approximately 8 keV to 25 keV as the projectile charge state increases from $Q = 26$ to $Q = 44$.

3.6.2.1 Derivation of the crater formation energy expression

We start with Sigmund's heated spike model [78, 79, 80, 81]. Beginning with Eq. (43) in Ref. [78] crater depth is,

$$d = \frac{CU}{Nk(dE/dz)}Y, \tag{3.14}$$

where C is the heat capacity per volume, k is the Boltzmann constant, U is the binding energy of the target atoms, N is the number density of target atoms, dE/dz is the total projectile energy deposited per depth and Y is the yield of atoms evaporated from the spike. Evaporation yield was derived from the evaporated particles per unit time per area in Eq. (24a), the effective sputter time in Eq. (31), effective sputter radius in Eqs. (32) and (33), and a material constant in Eq. (39b) (equations from Ref. [78]). After substituting these equations (that also have dependences on U, C, N, and dE/dz) into the crater depth formula and simplifying the result, we obtain

$$d = \frac{(dE/dz)k}{4\pi\Lambda U}\left(\frac{kT_0}{2\pi M}\right)^{\frac{1}{2}} \exp[-U/(kT_0)], \tag{3.15}$$

where T_0 is the initial temperature of the spike, M is the mass of the target atoms, Λ is the thermal conductivity of the target material.

To obtain Eq. 3.13, we define the total energy deposited within the depth

of the film s_0 as $E_{\mathrm{dep}} = (dE/dz)s_0$ and substitute E_{dep} into the previous equation,

$$d(E_{\mathrm{dep}}) = \frac{\eta E_{\mathrm{dep}}(kT_0)^{1/2}}{Us_0} \exp[-U/(kT_0)]. \tag{3.16}$$

From kinetic gas theory we calculate the initial thermal energy of the spike [79]. To obtain the E_{dep} values corresponding to the observed craters, we find the roots of the equation $d(E_{\mathrm{dep}}) + s(\sigma_{\mathrm{c}}) = s_0$, by inserting the σ_{c} values measured for each charge state Q in Fig. 3.6. The first and second terms on the left hand side of the equation below are $d(E_{\mathrm{dep}})$ and $s(\sigma_{\mathrm{c}})$ respectively,

$$\sqrt{\frac{2}{3}} \frac{\eta}{Us_0} E_{\mathrm{dep}}^{3/2} \exp\left[-\frac{3U}{2E_{\mathrm{dep}}}\right] - \frac{1}{\beta\sqrt{\phi}} \ln\left[\frac{\sigma_c}{G_0}\right] = s_0. \tag{3.17}$$

The results of $E_{\mathrm{dep}}(Q)$ from the $s(\sigma_c)$ data in Fig. 3.6 are plotted in Fig. 3.15. Now Eq. 3.17 provides a means of going from a measurement of the tunnel conductance σ_c to the corresponding crater formation energy E_{dep}, based on the known parameters ϕ, U, s_0 and constants G_0, β. If we input these known parameters and the measured $\sigma_c(Q)$ values from Fig. 3.6, we can obtain the crater formation energy at each charge state $E_{dep}(Q)$. Thus, Eq.3.17 provides a means of going from each measurement of σ_c to E_{dep} based on known parameters, as a function of charge state Q. Error bars in Fig. 3.15 also include the propagation of uncertainty for the value $\Delta G_0 = 5\ \mu$S, to account for non-idealities in transport such as reflection. However, the results in Fig. 3.15 are only logarithmically dependent on G_0.

3.6.3 Potential energy

The total amount of potential energy available is determined by atomic binding energies (ionization energies), *i.e.*, the energy cost for removing an electron from a neutral or partially ionized atom. For Xe^{Q+}, these energies are plotted in Fig. 3.10, as compiled by Saloman [84]. The total potential energy, or *neutralization energy* (E_Q), for each charge state is equal to the sum of the ionization energies of the removed electrons. The ionization energy is defined as the energy required to increase the charge state from Q to $Q+1$. As an ion regains Q electrons during neutralization, it lowers its total potential energy by E_Q. In Fig. 3.10, E_Q and the ionization energy for each charge state are plotted with blue and red points respectively. The labels in the figure indicate the shell from which an electron was removed. For example, at $Q < 18$ electrons are removed from the O shell during ionization and Xe^{18+} is Kr-like. Xe^{44+} (a frequently used ion in the experiments) has its remaining electrons in filled K,L shells and is Ne-like. The neutralization scenario for HCIs at a surface has been discussed in detail previously [23] and is shown schematically in Fig. 3.3(a). A more detailed discussion of above-surface electron capture by HCIs above thin dielectric films, is presented in Chapter 4 of this thesis. In general, as the ion approaches a critical distance of a few nanometers from the surface, electrons from the metal are captured into highly excited states of the projectile forming a neutral "hollow atom". Only a small fraction ($< 10\%$) [85, 27] of the neutralization energy can be dissipated above the surface through Auger electron and x-ray emissions, even for the case of slow HCIs ($v < v_{\mathrm{bohr}}$). Upon entering the solid the evolving HCI is re-ionized through the "peeling off" of excited electrons [23, 25], and the ion remains far from charge state equilibrium. In the following discussion of sub-surface charge equilibration,

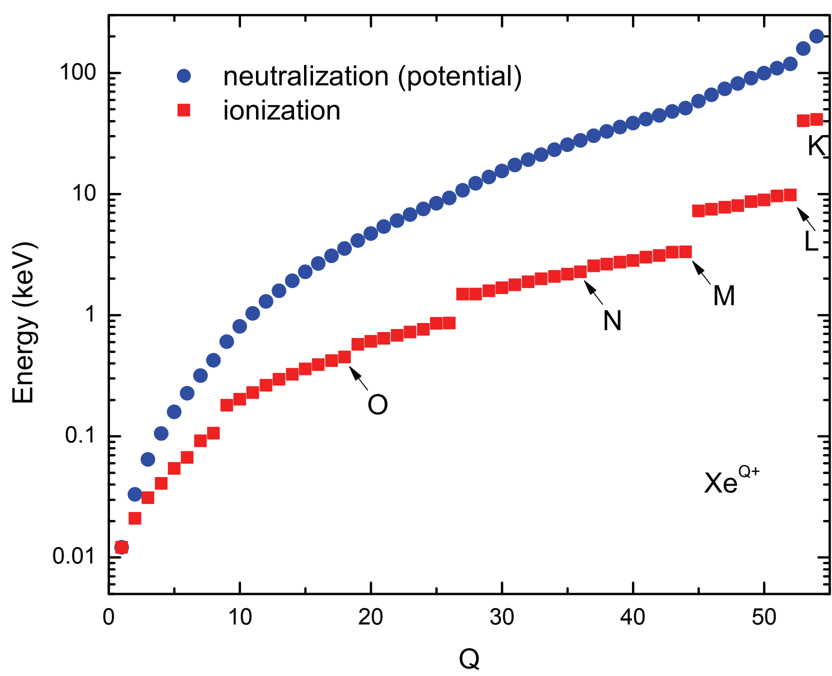

Figure 3.10: Ionization and neutralization energies for Xe. Electron shells are indicated.

we shall assume that the projectile is completely re-ionized upon penetrating the solid. This means that the ion regains its initial charge state Q, after captured electrons in outer shells are screened by the electrons in the solid.

Deposition of E_Q into a solid occurs in connection with neutralization, as the ion's charge equilibrates. The timescale of charge equilibration determines the rate at which potential energy deposition can occur. Additionally, the charge equilibration timescale in relation to the ion drift timescale determines how far the ion travels within the target material, before neutralizing. For these reasons, it is necessary to consider the charge equilibration timescale in the thin film experiment.

3.6.4 Charge equilibration timescale

As the ion penetrates the target, electrons in Rydberg states are "peeled off" and a more compact cloud of target electrons screens the highly excited projectile, forming a sub-surface "hollow atom"[18]. After this process, the re-ionized projectile regains its initial charge Q below the surface.

Starting with the Bohr stripping criterion, the equilibrium charge state is [86]:

$$Q_{eq} = Z_{ion}^{1/3} \times (v/v_0) \tag{3.18}$$

Variations of Eq. 3.18 appear throughout the literature. This formula expresses the condition for which ionic bound electrons are lost in a collision, with target nuclei and electrons, when their velocity is below v. Therefore, it approximates the equilibrium or mean charge state Q_{eq} of an ion traversing a lattice at speed v. v_0 is the Bohr velocity ($v_0 = a_0 E_H/\hbar \approx 2.187 \times 10^6$ m/s from Appendix G), and Z_{ion} is the atomic number of the ion.

As the ion neutralizes below the surface of a solid, its charge state decays toward the equilibrium value Q_{eq}. Empirically, this subsurface charge evolution follows a time-dependent exponential decay function [87]:

$$Q(x) = Q_{eq} + (Q_i - Q_{eq})\mathrm{e}^{-\alpha(x/v)}. \tag{3.19}$$

Here, Q_i is the initial charge state, and $Q(x)$ is the ion's charge state after it has traveled a distance x within the solid. De-excitation proceeds via Auger and radiative transitions, as Q approaches the equilibrium charge state. Below, two previous measurements of sub-surface relaxation are mentioned, to provide context for equilibration timescales in our experiment.

Ref. [88] reports relaxation timescale measurements based on X-ray emission of both the front and back side of a Ta foil target for Pb^{Q+} for $53 \leq Q \leq 58$. In these experiments, velocities of the ions were 0.30 a.u. $\leq v \leq$ 0.31 a.u. By detecting the x-rays emitted during M-shell filling, the authors concluded that the relaxation times varied between 68 ± 10 fs for $Q = 53$, and 22 ± 4 fs for $Q = 58$.

Ref. [45] reports velocity dependent measurements of the exit charge state of Xe^{44+} ions, after they have traveled a distance $x = 5$ nm through a carbon film. Fitting these $Q(x = 5$ nm) data as a function of v to the exponential model in Eq. 3.19, a charge equilibration time constant $\alpha = 4.7 \times 10^{14}$ s^{-1} is extracted. The authors conclude that on average, a highly charged xenon equilibrates within approximately 7 fs. The range of velocities in this experiment was 0.24 a.u. $\leq v \leq$ 0.45 a.u.

Based on these measurements, full relaxation requires at least 7 fs to 68 fs. The primary question in the HCI experiment is whether or not all of the ion's potential energy can be deposited within the thickness of the thin film. For

the data shown in Fig. 3.6, the slowest projectiles have nominal perpendicular velocities v = 576 km s^{-1} (neglecting image acceleration) and pass through the 14 Å surface film within 2.5 fs. This means that the craters formed in the film are the result of sub-surface pre-equilibrium energy deposition within a short ($<$ 2.5 fs) time window.

Applying the analysis of Ref. [45] and using its measured time constant, charge state as a function of penetration depth is plotted in Fig. 3.11. Here $Q(x)$ is shown for Xe^{Q+} for Q = 18, 36, 44 with kinetic energies $(8 \times Q)$ keV. The thickness of the film is shaded in the region $x < s$, where $s = 1.4$ nm. Based on the exponential model, projectiles with the initial charge states Q= 26, 36, and 44 decay to $Q(x = s) = 8$, 14 and 18 upon penetrating the thickness of the film. Each of these charge states pass through the film within less than 2.5 fs, and there is insufficient time for full relaxation of the subsurface hollow atom. In contrast, the Q_{eq} for each of the charge states is a penetration depth of about 10 nm.

The charge equilibration rate determines the amount of time available for deposition of E_Q into the solid, because potential energy is released in connection with neutralization.

In Fig. 3.12, the total potential energy for each charge state is represented in filled symbols (E_Q). As described previously, E_Q is the total potential energy difference between the ion of charge state Q, and a neutral atom. This potential energy is deposited along a charge equilibration length (approximately 10 nm), as the ion captures its missing electrons. At penetration depths smaller than the charge equilibration length, electron vacancies remain.

So, the amount of potential energy that can be deposited within a penetration depth x is,

$$E_Q^{film}(x) = E_Q[Q(0)] - E_Q[Q(x)]. \tag{3.20}$$

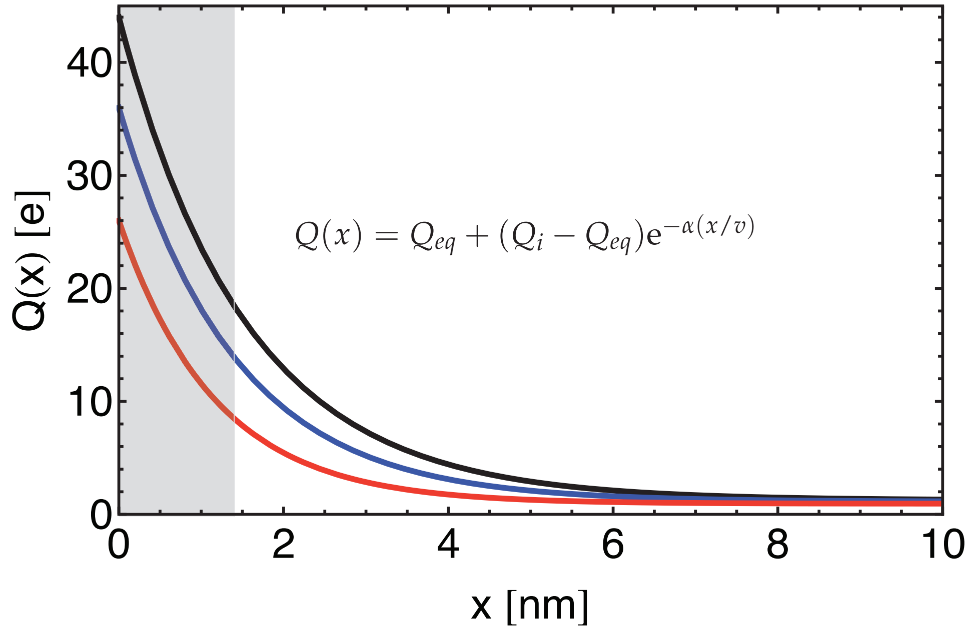

Figure 3.11: Exponential model for charge state equilibration. Initial charge states 44, 36, 26 relax toward equilibrium charge state Q_{eq} as the ion penetrates the solid. The shaded region indicates the thickness of the film.

Here, $Q(0)$ is the initial charge state of the ion, and $Q(x)$ is the charge state after the projectile has traveled through a distance x in the target (taken from Fig. 3.11). $E_Q^{film}(x = s)$ is plotted with open symbols in Fig. 3.12, and comprises more than 90 % of E_Q. The quantity $E_Q^{film}(x = s)$, can be considered the amount of potential energy deposited within the thickness of the film. It is difficult to assign a "potential energy" to the moving ion, in an excited state. However $E_Q^{film}(x)$ allows the assignment of an upper bound on the total potential energy deposited within depth x. It is clear that the projectile will not fully equilibrate to deposit the full amount E_Q within a surface film of thickness $s = 1.4$ nm. Decreasing the velocity of the ion, would increases the fraction of E_Q that is released while the ion is within the film.

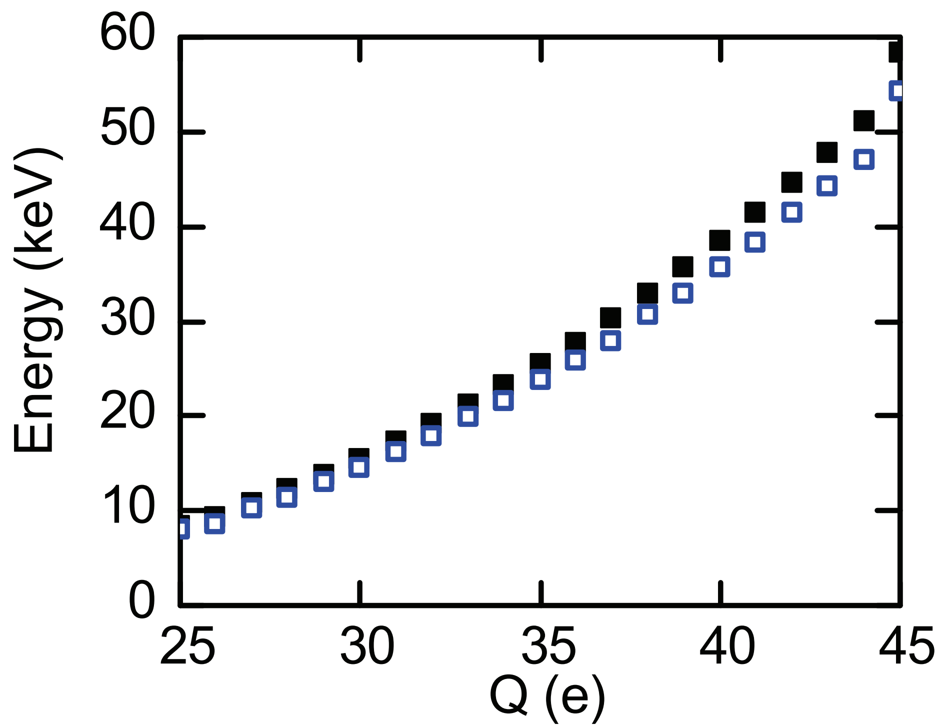

Figure 3.12: Xe neutralization energy (E_Q – ■) and neutralization energy dissipated within the 14 Å film (E_Q^{film} – □) assuming exponential charge equilibration.

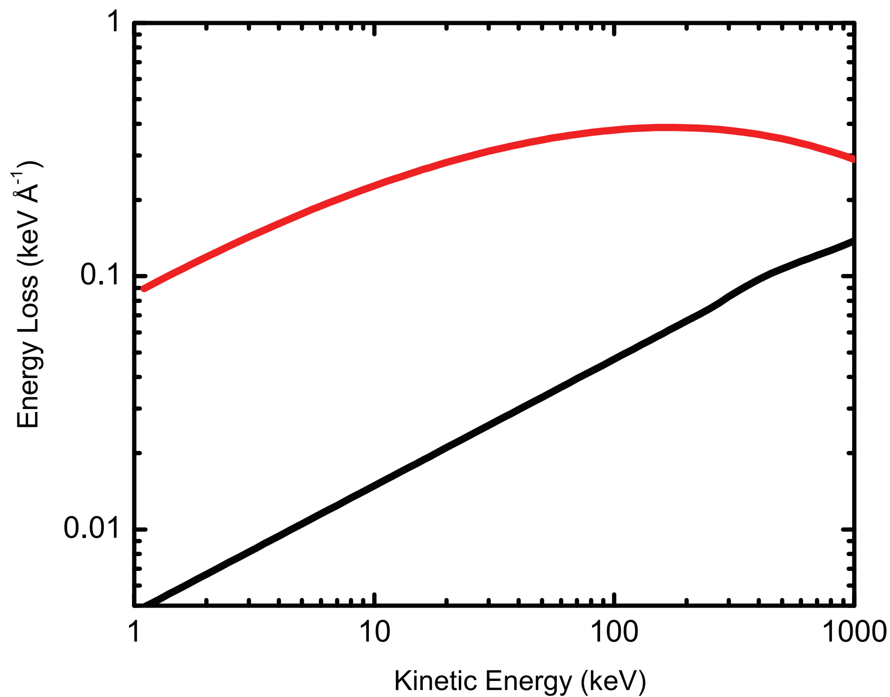

Figure 3.13: SRIM calculated nuclear (red) and electronic (black) kinetic energy loss rates for Xe^{1+} on Al_2O_3.

3.6.5 Kinetic energy

3.6.5.1 SRIM

SRIM/TRIM provides a semi-empirical model that gives a good starting place for estimating the stopping ranges and energy loss rates for a wide variety of projectile species, incident energies, and target materials [29]. Figure 3.13, displays the SRIM prediction for average kinetic energy loss per path length (dE/dz) as a function of kinetic energy, for Xe^{1+} incident on Al_2O_3 in the energy regime from 1 keV to 1000 keV. As can be seen from the figure, the nuclear stopping power, *i.e.*, momentum transfer between the ion and target nuclei is the dominant

energy loss mechanism. The position of the maximum of the nuclear stopping in Fig. 3.13 is a direct result of the mass ratio between Xe and Al/O. In comparison to the nuclear stopping, energy transfer from the Xe to the target electrons is relatively inefficient. Electronic and nuclear stopping powers are $(dE/dz)_{el}$ = 0.09 keV Å^{-1} and $(dE/dz)_{nuc}$ = 0.37 keV Å^{-1} for Xe^{+} at 350 keV in aluminum oxide. The total stopping power $(dE/dz)_t$ is the sum of the nuclear and electronic contributions. Assuming that the ion undergoes constant deceleration in the target (continuous slowing down approximation), there is simple relationship between kinetic energy loss rate and average stopping range:

$$\bar{R}_p = \int_0^E \left[\frac{dE(z)}{dz}\right]_t^{-1} dE. \tag{3.21}$$

For Xe^{1+} at 350 keV, the expected average stopping range R_p is approximately 80 nm. Note that this is about an order of magnitude larger than the charge equilibration length shown in Fig. 3.11. The ion neutralizes long before it stops.

3.6.6 Charge dependent stopping power

For low energy HCIs (KE < 1 MeV) nuclear stopping power remains the dominant kinetic energy loss mechanism, as it is for singly charged ions. In fact, the high Q can further amplify nuclear stopping power [27, 35]. Especially in insulator target materials, where free electrons cannot provide any screening of the projectile, the projectile's Coulomb interaction reaches beyond its nearest neighbors. The amount of momentum transferred from the projectile to the target nuclei is proportional to 1) the radius of interaction divided by the projectile velocity and 2) the number of target atoms within that interaction radius. Both

1) and 2) increase dramatically for slow highly charged ions. This means that a significant enhancement of kinetic energy transfer is predicted in the ion's track, before it equilibrates. Ref. [35] predicts that this effect will be especially strong for, *e.g.*, Xe^{44+} in SiO_2 at $E < 300$ keV. The stopping enhancements may even be strong enough to lead to a decrease in the average stopping range of slow HCIs in insulators (via Eq. 3.21). When Sb^+ and Sb^{25+} were implanted at 120 keV, the mean depth of the $Q = 25$ ions was significantly compressed [89]. This compression effect becomes observable for low kinetic energies and high charge states as the charge equilibration length increases with respect to the stopping range.

The model in Ref. [35] expresses the nuclear stopping term (S_n) (energy loss per path length):

$$\check{P} = \frac{QZ_2^* e^2}{2E/(1+\mu)} \sqrt{\frac{\gamma E}{\check{T}} - 1} \tag{3.22}$$

$$S_n = n \int_0^{\check{P}} 2\pi P \mathrm{d}P = \frac{\pi \mu n}{E} (QZ_2^* e^2)^2 \ln(\gamma E / \check{T}) \tag{3.23}$$

where P are the impact parameters, $\mu = M_1/M_2$ is the mass ratio between projectile and target atoms, Q is the ion charge state, $Z*_2$ is the charge of the target nuclei, $\gamma = 4\mu/(1+\mu)^2$, $\check{T}$ is the minimum transferable energy, and n is the atomic density. These formulas are valid for $\gamma E \geq \check{T}$ [35]. The salient feature in this function is its rapid increase of nuclear stopping power at low kinetic energies. In the model, stopping power increases asymptotically as kinetic energy decreases as $S_n \propto Q^2/E$.

Ref. [35] also derives a prediction for the electronic stopping, from the "effective charge" approach. Screening length of the ion nucleus by the non-

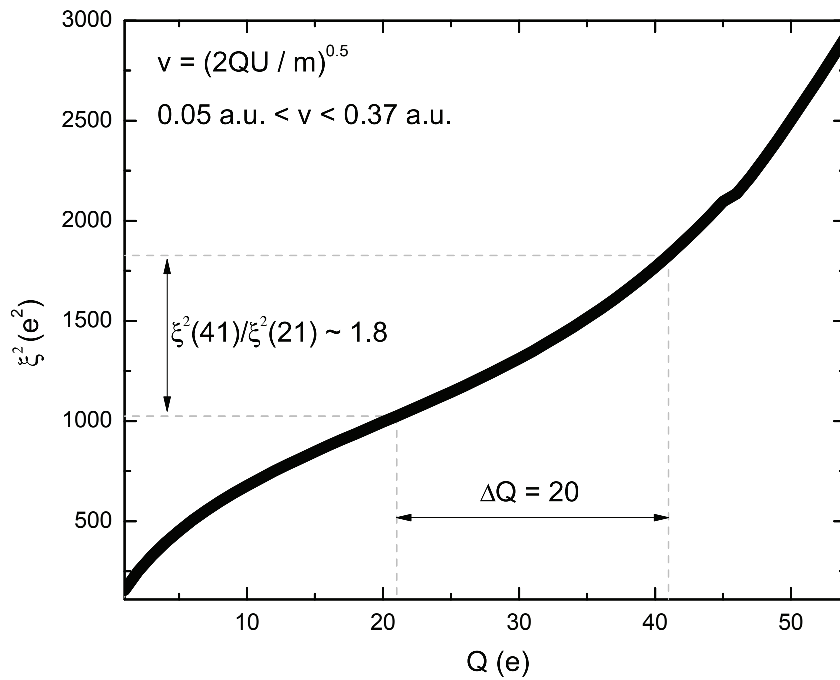

Figure 3.14: Effective charge squared is proportional to the electronic stopping power. This parameter increases by less than a factor of 2 as Q increases from 21 to 41 [35]. Parameters were taken from the experiment in [1].

stripped electrons is:

$$\Lambda_1 = a_0 \frac{2(Z_1 - Q)^{2/3}}{Z_1 - (Z_1 - Q)/7} \tag{3.24}$$

where a_0 is the Bohr radius, Z_1 is the projectile nuclear charge. This makes $(Z_1 - Q)$ the number of remaining non-stripped electrons.

The effective charge[90, 29] can be obtained assuming that the electron distribution surrounding the nucleus has the form,

$$\rho(r) = \frac{(Z_1 - Q)}{4\pi\Lambda_1^2} \frac{\mathrm{e}^{-r/\Lambda_1}}{r}. \tag{3.25}$$

Integrating with target electrons at all separations, and averaging over all impact parameters yields the effective charge:

$$\xi = Q + \frac{Z_1 - Q}{2v_f/v_0} \ln \left[1 + \left(2 \frac{v_f}{v_0} \frac{\Lambda_1}{a_0} \right)^2 \right]. \tag{3.26}$$

Here, v_f is the Fermi velocity of electrons in the target, and v_0 is the Bohr velocity. The electronic stopping power varies as ξ^2 ($[dE/dz]_{el}(Q) \propto \xi^2$). Effective charge squared ξ^2 is plotted in Fig. 3.14. This parameter shows the relative increase in electronic stopping as a function of charge state. In Fig. 3.14, ξ^2 less than doubles as charge state increases from Q = 21 to 41.

The magnitude of electronic stopping is small compared to nuclear stopping for low energy ions. In order to assign actual numerical stopping power values using the model, the electronic stopping power was anchored by the $Q = 1$ value from SRIM, and extrapolated to higher charge states, going as ξ^2. In order to determine the numerical values of stopping power, the constant α_1 was found

by inputting the $(dE/dz)_{el}$ from SRIM and ξ^2, for $Q = 1$:

$$\frac{dE}{dz}_{el} = \alpha_1 \xi^2(Q) \tag{3.27}$$

For our experimental parameters the proportionality constant between stopping power and squared effective charge turns out to be $\alpha_1 = 1 \times 10^{-3}$.

To summarize, the electronic stopping described by Eq. 3.27 has a smaller magnitude than the nuclear stopping described by Eq. 3.22 for a slow HCI impinging on aluminum oxide. Additionally, electronic stopping from Eq. 3.27 has weaker dependences on charge state and kinetic energy than does the nuclear stopping. For slow HCIs, nuclear stopping remains the dominant stopping mechanism, according to the model [35].

3.6.7 Energy Accounting

The tunneling conductance measurements in the experiment are sensitive to modifications of the dielectric barrier. Therefore, we consider the potential and kinetic energy deposited into the thickness of the ultrathin film s_0. Kinetic energy deposition can be calculated by multiplying the nuclear and electronic energy loss rates by the film thickness.

In the low kinetic energy regime ($E \approx 300$ keV), nuclear stopping is the most significant kinetic energy loss term for singly charged ions, and its magnitude is further increased when $Q \gg 1$. This increase arises from the enhancement of long range Coulomb interactions which transfer small amounts of energy to large numbers of target atoms. Electronic stopping also increases with Q, but its value makes up only 7 % of the total kinetic energy loss for the E and Q described here.

Given the $Q = 1$ stopping powers from stopping range data [91] and the SRIM code [29] as well as the predicted functional dependence of electronic and nuclear stopping on Q and E at higher charge states [35], we find that the total (nuclear and electronic) kinetic energy loss per length $(dE_{\mathrm{n}}/dz + dE_{\mathrm{e}}/dz)$ increases from 0.5 keV Å^{-1} to 0.8 keV Å^{-1} as the charge increases from $Q = 26$ to $Q = 44$. This equates to deposition of 7 keV to 12 keV kinetic energy into the thickness of the film (E_{n} + E_{e}). Both E_{n} and E_{e} as well as their combined contributions to the energy deposition are plotted in Fig. 3.15.

The validity of SRIM is often questioned for slow heavy ions stopping in insulators. Therefore, we compared the SRIM value to a stopping range experiment for 200 keV Xe ions in aluminum oxide [91]. Using the measured ranges [91], and the continuous slowing down approximation we inverted Eq. 3.21 to find the total stopping rate of $dE/dz = 0.398$ keV Å^{-1}. In comparison, SRIM gives $dE/dx = 0.453$ keV Å^{-1}. After multiplying this stopping rate times s_0, the experimental kinetic energy deposition at $Q = 1$ is plotted as the open triangle in Fig. 3.15. The SRIM value is also plotted as the open circle. The experimental and SRIM values agree within 12 %.

The crater formation energies E_{dep} in Fig. 3.15, are supplied by both the kinetic and potential energy of an impacting ion. Therefore, we seek to partition the contributions between the kinetic (energy loss through stopping) and potential (energy loss through neutralization) to gain insight in to the elastic and inelastic loss processes that HCIs undergo. In addition to the large amount of potential energy, high Q projectiles also experience enhanced stopping power via Eqs. 3.22,3.26. In order to partition E_{dep}, we use the functional dependence of stopping on Q and E for low energy ions from Refs. [35] and [36].

The crater formation energies ($E_{\mathrm{dep}}(Q)$) increase much more rapidly than

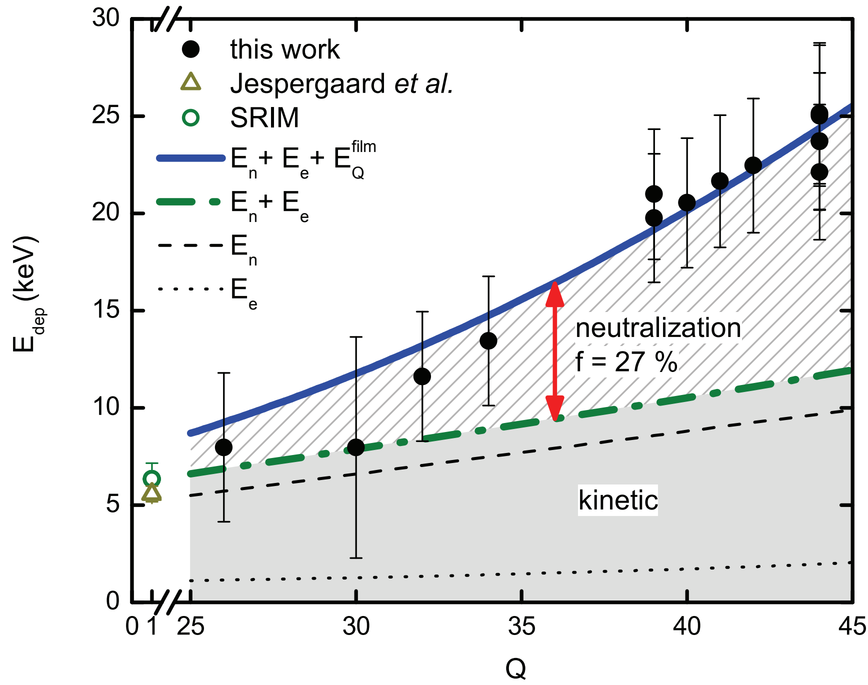

Figure 3.15: Each point represents the energy required to form a crater, determined from a heated spike model. E_{dep} includes both kinetic $(E_{\mathrm{n}} + E_{\mathrm{e}})$ and neutralization (E_Q^{film}) energy deposited within the depth of the film. Error bars were determined by propagation of uncertainty in the data and model parameters. The open circle is the kinetic energy deposition for $E = 210$ keV Xe^{1+} from SRIM [29]. Fitting the data with $E_{\mathrm{dep}} = E_{\mathrm{n}} + E_{\mathrm{e}} + f E_Q^{\mathrm{film}}$ gives the minimum fraction of neutralization energy $f = 0.27 \pm 0.02$ required for crater formation.

the total kinetic energy loss (E_n + E_e) as Q increases. Clearly, neutralization energy must be considered in order to account for the E_{dep} values. First, we estimate the amount of neutralization energy lost by the ion as it traverses the thickness of the film. Invoking an exponential charge state decay model [92, 86], we calculate the charge state for a given ion that has traveled s_0 using the measured time constant from Ref. [45]. We then subtract the corresponding neutralization energies for this charge state and the initial charge state from one another to estimate the neutralization energy (E_Q^{film}) lost while the ion is within the film. E_Q^{film} represents the available neutralization energy that can contribute to heating the spike within the thickness s_0 and comprises more than 90 % of E_Q as is displayed in Fig. 3.10. A fit to the data with the solid line $E_{dep} = E_n + E_e + fE_Q^{film}$ in Fig. 3.15 gives the fraction of available neutralization energy that contributes to formation of a crater to be $f = 0.27 \pm 0.02$.

The uncertainty on this fraction, represents the standard error of the fit. Uncertainty in f does not include a quantitative assessment of the error from the model in Ref. [35]. The fE_Q^{film} values are considered lower bounds on the total neutralization energy required to form the craters we observe in the Al_2O_3. In extracting f from the fit we assume that E_e and E_n are completely converted to heat in the collision spike. However for insulating materials, conversion of the electronic excitation to heat is not perfectly efficient [78], and its value will be smaller than the electronic stopping power integrated over the film thickness. It is important to note that the charge dependent stopping powers in Ref. [35] were derived as bounds and that the numerical value of f depends on the stopping power model.

3.6.8 Comparison with previous measurements

Schenkel and co-workers have reported that as much as 40 % of the neutralization energy from Xe^{52+} projectiles is delivered into a Si detector target [27], where the remainder is emitted to the vacuum through Auger electrons and photons. We expect our measured fraction to be smaller than the result of Ref. [27], because craters only record the energy deposition that results in irreversible change of the material. Heated regions of the spike below the energy threshold for evaporation will quench and remain solid. The energy required for this subthreshold heating is transfered to the solid, but not represented in the measurement of a crater depth. Therefore, regarding the total energy deposited to the material, f quantifies the role that neutralization energy plays in the creation of irreversible defects.

3.6.9 Decreased kinetic energy

In an attempt to measure the dramatic increase in kinetic energy deposition predicted in Eq. 3.22, we began an experiment with the G2 devices using lower ion extraction voltages. Initially, we have decreased the kinetic energy by about 40 %, from $(8 \times Q)$ keV to $(5 \times Q)$ keV. G2 devices were irradiated with xenon ions with charge states $Q = 36$ and $Q = 41$ at $(5 \times Q)$ keV.

Figure 3.16 shows a representative plot of device conductance as a function of ion dose, for the 5 kV extraction voltage, using the G2 masks. The solid (red) points are from sample `111222-04`, dosed with $Q = 41$ ions, and the open (blue) points are from the sample `111222-14`, dosed with $Q = 36$ ions. The model of Eq. 3.4 describes the data well. Fits to the conductance measurements on individual chips give slopes of 1.83 ± 0.02 μS/ion, and 84 ± 6 nS/ion for $Q = 41$ and

$Q = 36$ respectively in Fig. 3.16. As with the previous case, the slope of $G(N)$ increases with increasing ion charge state. Each line is a fit to the conductance of devices on a single chip. Increased device resistance in G2 devices provides a greater range of measurable resistances, and smaller error bars in Fig. 3.16. For devices with higher resistances, the uncertainty on R_{dev} and G are smaller for G2 than for G1 devices. Note that in Fig. 2.10, we see that the G2 masks can measure devices with smaller RA, before running into the negative resistance problem.

We determine that the most probable average conductance per ion values (from a set of 7 chips) are $\sigma_c = 86 \pm 4$ ns and $\sigma_c = 1.43 \pm 0.09$ μS for charge states $Q = 36$ and $Q = 41$ respectively. In comparison to previous data obtained at $(8 \times Q)$ keV for $Q = 41$, $\sigma_c(Q = 41)$ for the slower ions is greater by a factor of $\sim$10. Further kinetic energy dependent studies are required to assess whether this increase is due to enhancement of stopping power. For three of these devices, data analysis is shown in Appendix E.

3.7 Chapter Summary

In this chapter, I presented a basic overview of the EBIT and beamline used to carry out the HCIMM experiments. Additionally, I outlined a method of irradiating tunnel junctions with HCIs in order to detect modifications to the oxide barrier via a measurement of tunnel conductance. The HCIs form individual nanoscale crater-like defects in the thin film barrier. For sufficiently low ion doses, conductance of the devices increases linearly with the number of ions that impact the barrier.

We reported ion induced crater depths in the ultrathin dielectric films as a function of projectile charge state. From the depth scaling of the craters with

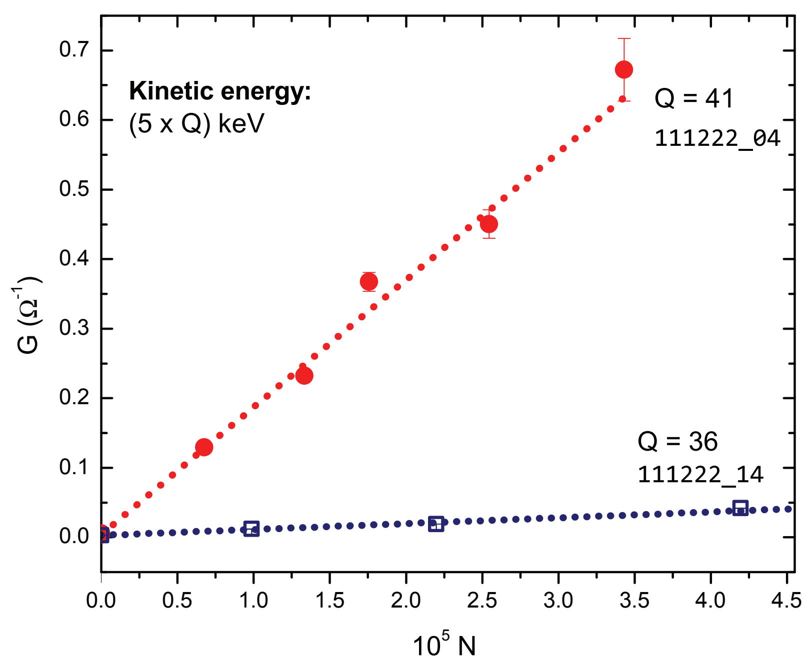

Figure 3.16: Device conductance as a function of ion dose for samples `111222-4` and `111222-14` that were dosed with Q = 41 and Q = 36 Xe^{Q+}, respectively. Devices were grown with the G2 masks

charge state, we determine the energy deposited into the thin film in HCI-surface impact increases from 8 keV to 25 keV as Q increases from 26 to 44 by invoking a heated spike model from Sigmund. With this approach we inverted Sigmund's expression for $d(E_{dep})$ to arrive at crater formation energy as a function of crater depth, for each charge state in the experiment. Accounting for both pre-equilibrium kinetic energy loss and neutralization energy, we measure that at least (27 ± 2) % of the available neutralization energy contributes to crater formation. This result represents a lower bound for the fraction of HCI neutralization energy required to form a permanent material defect.

Looking forward, it may be possible to further decrease the kinetic energy of the HCIs and observe greater pre-equilibrium enhancement of stopping power as the ion deposits its energy within the thin film. Enhancement of stopping for ions in pre-equilibrium charge states has been observed in energy loss measurements using thin foils [8], and stopping ranges measurements [89]. Counter-intuitively, Ref. [35] predicts that slower ions may result in even higher kinetic energy deposition by HCIs.

Chapter 4

Classical over-the-barrier model for neutralization of highly charged ions above thin dielectric films

4.1 Introduction

Slow highly charged ion (HCI) interactions with solids continue to be an active area of research at the interface of condensed matter and atomic physics. Due to the complex interaction between projectiles with charge states $Q \gg 1$ and the multitude of target electrons involved in the neutralization process, a complete picture for electron capture, emission and the formation of material defects remains challenging outside of a few specific target materials, *i.e.*, bulk metals [23] and bulk ionic crystals [93, 94]. For these cases, the classical over-the-barrier (COB) model gives quantitative predictions that are in good agreement with electron emission statistics [95, 96], X-ray spectra [24] and ion image acceleration measurements [97, 98]. The foundation of COB is that the first electronic trans-

mission from target to ion, occurs in a classically allowed region and populates high n states in the ion. For HCIs, filled levels in the metal become resonant with the high n states at a distance of a few nanometers outside the surface. Thus initial charge transfer takes place predominantly via fast transitions over the top of the vacuum potential barrier from the target to the projectile. Once captured by the projectile, these electrons decay to fill inner shell vacancies and promote the emission of Auger electrons and photons. The critical distance for first charge transfer (R_c) can be well approximated using classical potentials, due to the "point charge"-like nature of the ion at a relatively far distance from the target electrons. R_c sets a characteristic timescale $(\tau \approx R_c/v_p)$ for above-surface electronic processes, before ion impact. The importance of R_c is that it describes the distance between the ion and solid at the onset of the ion neutralization process.

Within COB, the basic material properties that govern the onset of above-surface neutralization are electron binding energy (work function) W, energy band gap E_G and permittivity ϵ. Deposition of a thin dielectric film on a metal surface introduces new W, E_G and ϵ for the surface layers without modifying the bulk. Thus, deposition of a thin film is an experimental means of changing the electronic structure of the surface, in order to test the role of surface versus bulk material properties during HCI neutralization. This approach was used to measure above-surface emission of Auger electrons as a function of LiF film coverage on Au(111) up to 1 ML in order to decouple the role of target binding energy and band gap in K-shell filling [2, 3]. The authors remark that even for a single monolayer of LiF coverage, the high binding energy of the LiF results in a suppression K-shell filling, suggesting that for LiF/Au(111), the target takes on the W characteristics of the thin film rather than bulk material.

In some cases however, dielectric thin film covered targets retain the metallic character of the bulk substrate. Recent results on HCI interactions with thin films show electron emission yield as a function of C_{60} film thickness on Au(111) [4]. Here, it is shown that there is a measurable increase in the total potential emission yield relative to clean Au(111) with increasing C_{60} film thickness. The film enhances rather than suppresses the efficiency of Auger relaxation relative to a clean metal surface. Within a measurement of the electron emission spectrum, the target produces high electron yields even after the deposition of approximately 5 ML of dielectric material.

These seemingly contradictory results motivate an application of COB to model electron capture by HCIs above metal surfaces covered with thin dielectric films. Until now, above-surface charge exchange for HCIs interacting with thin films has not been treated systematically with COB. In this chapter, we describe application of COB to the initial charge exchange between HCIs and target electrons in solids covered with thin films. We develop a simple physical model that describes the crossover from the thin film to bulk target regimes as a function of the film electronic properties and thickness. Adding a thin film to a bulk surface leads to new boundary conditions in the construction of the electronic potential energy landscape, and modifies the critical distance at which electrons can be captured by the ion. For the case of a metal surface covered with a thin dielectric film, we calculate ion capture distances and compare these results to bulk metal and insulator targets. New studies of highly charged ion interactions with thin films will require this type of predictive model to gain insight into the role of bulk versus surface electrons during neutralization.

The chapter is organized as follows. First, we introduce the basic framework and assumptions of the existing COB picture for electron capture by HCIs

above bulk metal and insulator targets (Sect. 2). Then, using the framework from Sec. 2, we describe how the potential of an "active electron" in the first stage of above surface neutralization is modified by the presence of a thin dielectric film at the surface (Sect. 3). In Sect. 3 we derive thickness dependent critical distances starting with parameters for ultrathin C_{60} thin films on Au(111). The dependence of critical distance on film permittivity, band gap and metal work function are then discussed. In Sect. 4, we discuss comparisons between the model and three experimental systems C_{60}/Au(111), LiF/Au(111) and Al_2O_3/Co. Finally, the results are summarized in Sect. 5.

This chapter presents the revised version of a previously published model [71]. The main improvement in the model presented here is in calculation of the ion's image potential. The model contained in this chapter solves Poisson's equation exactly for the metal-dielectric-vacuum system, matching the boundary conditions at both the metal and dielectric surfaces. The previously published version did not include the electric field boundary constraint at the dielectric-vacuum interface. As will be shown below, both versions of the model demonstrate the same qualitative behavior when calculating electron capture distances. However, some numerical results change when discussing the Al_2O_3/Co system.

4.2 Bulk targets

To define the basic framework and assumptions from COB, it is instructive to first consider the case of a HCI with initial charge state Q, at a distance R outside of an ideal metal surface following the approach and notation from Refs. [99, 16, 23]. The potential energy for an "active electron" in the region between the surface and ion has three terms: attraction between the electron and the

ion ($V_{p,e}$), attraction between the electron and its self-image (V_e^{im}), and repulsion between the electron and the target dielectric response induced by the ion ($V_{p,e}^{im}$). The last term can be considered the HCI's image charge. The potential energy for the "active electron" in the region between the ion and surface is the sum of these three terms (in atomic units, defined in Appendix G),

$$V(z) = V_e^{im}(\mathbf{r}) + V_{p,e}(\mathbf{r}, \mathbf{R}) + V_{p,e}^{im}(\mathbf{r}, \mathbf{R}). \tag{4.1}$$

If the target medium has finite electric permittivity the image terms are modified by a factor $\beta = (\epsilon - 1)/(\epsilon + 1)$,

$$V_{p,e}(\mathbf{r}, \mathbf{R}) = -\frac{Q}{|\mathbf{r} - \mathbf{R}|} \tag{4.2}$$

$$V_{p,e}^{im}(\mathbf{r}, \mathbf{R}) = \frac{\beta Q}{|\mathbf{r} + \mathbf{R}|} \tag{4.3}$$

$$V_e^{im}(\mathbf{r}) = -\frac{\beta}{4z}. \tag{4.4}$$

In these equations, the origin is set at the surface of the bulk, directly in front of the ion where $\mathbf{r}$ and $\mathbf{R}$ are position vectors for the test charge and ion, respectively.

These are classical potentials in the asymptotic limit and are valid when the ion moves slowly with respect to the Fermi velocity of the target electron and when the ion is far from the surface. For $Q \gg 1$, capture distances are much greater than the dynamic screening length, and classical potentials are a reasonable approximation.

In Fig. 4.1(a) we plot the potential for the active electron within the vacuum region along two dimensions. The ion has charge Q = 26 and is positioned near the critical distance $R = 2$ nm from the metal surface. A shallow minimum along x forms a saddle point in the potential between the ion and target electrons. The

critical distance (R_c) is defined as the ion's position where the highest value of the vacuum potential between the ion and surface falls below the Fermi level in the target (dashed line in Fig. 4.1(a)). Classical charge transfer from the metal to the ion occurs through the saddle point.

Due to the small width of the saddle, charge transfer takes place in the coordinate normal to the surface, z. Figure 4.1(b) shows a one dimensional slice of the potential profile along z. Electronic states in the target are filled up to Fermi level (E_F), and the work function (W) separates E_F from the vacuum level. As the ion moves from $R = 6$ nm to $R = 2$ nm, the maximum in the potential drops below E_F and classical charge transfer is allowed. From Eqs. 4.2, 4.3 and 4.4 the critical distance is [99],

$$R_C \approx \frac{\sqrt{2Q\epsilon(\epsilon-1)}}{W(\epsilon+1)} + \frac{\epsilon-1}{4W(\epsilon+1)\epsilon}. \tag{4.5}$$

R_c has an approximate square root dependence on charge state, and inverse dependence on W. Fig. 4.1 represents the ideal metal case $(\beta \to 1)$ and the critical distance reduces to $R_c \approx \sqrt{2Q}/W$.

4.3 Dielectric thin films on metals

In the following section, we obtain critical distances for metals covered with thin dielectric films. In comparison to the clean metal case, the presence of a dielectric thin film adds a new metal-dielectric interface and requires additional boundary conditions to be satisfied. Following the framework and assumptions introduced in the previous section, we construct the potential for an "active electron" in a metal/dielectric/vacuum system.

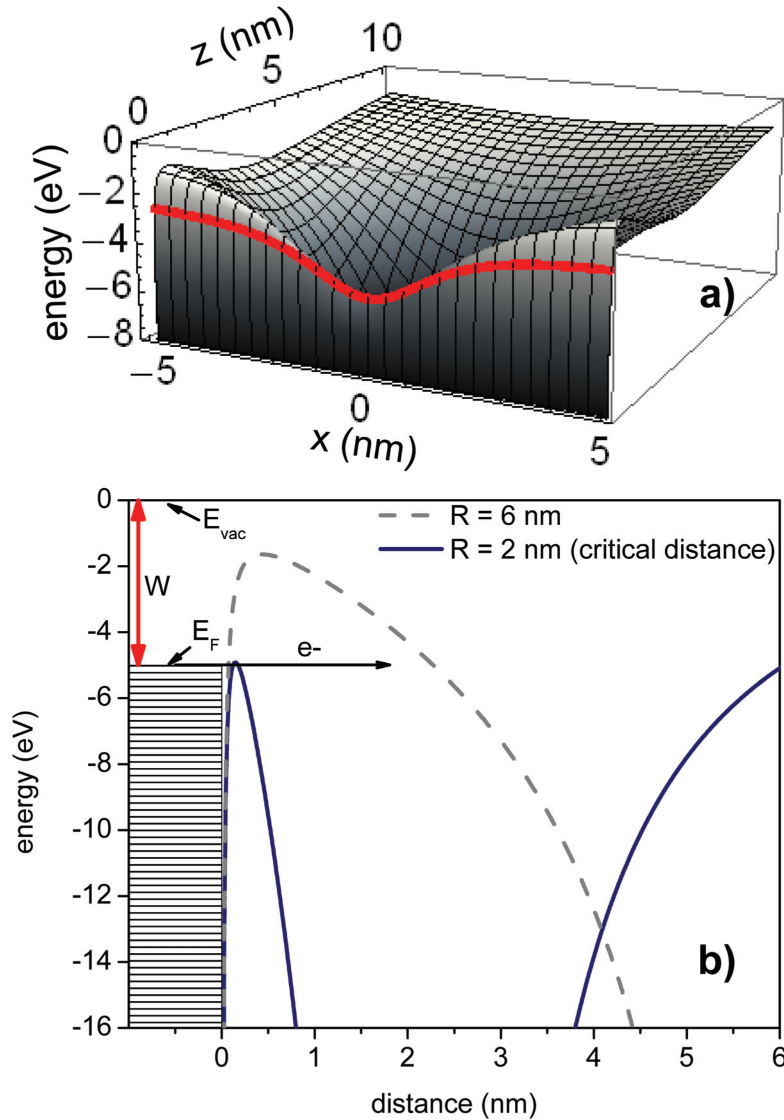

Figure 4.1: (a) 2D potential for a $Q = 26$ ion at the critical distance (R_c = 2 nm) outside a metal surface. The dashed line is the constant z where the saddle point minimum falls below E_F = 5 eV. (b) 1D potential at ion positions $R = 6$ nm and 2 nm. The work function is $W = E_{vac} - E_F = 5$ eV. Initial charge transfer occurs through the saddle point, over the vacuum barrier.

The potential is constructed as shown in the schematic in Fig. 4.2(a). The system requires an infinite series of image charges [100], to satisfy boundary conditions at both the metal-dielectric and dielectric-vacuum interfaces. As depicted in Fig. 4.2(a), both the ion and active electron induce dielectric responses within the target. For the ion, the series of image charges is denoted as Q', placed behind the metal surface. The active electron also experiences attraction due to self-image charges denoted by e' and e'' in the dielectric and vacuum respectively.

In Fig. 4.2(b), the potential energy for an active electron is plotted along z, for an ion position R, that is far from the surface. The potential is the sum of the terms V_{int}, V_i, V_{si} depicted schematically in Fig. 4.2(a). As shown in Fig. 4.2(b), the potential goes as approximately $1/R$ in the vicinity of the ion. Near the surface, electron self-image forces, and film permittivity determine the shape of the potential (discussed below).

4.3.1 Ion potential

4.3.1.1 Boundary conditions

We seek the potential energy of an electron in the dielectric, and vacuum regions as an ion of charge Q approaches the surface. To construct the potential for the test charge, we first consider the potential only due to the ion and its dielectric response in the target (neglecting the electron's self-image term). The general approach is to modify Eqs. 4.3 and 4.4 to account for the presence of a thin dielectric film. Obtaining this modified potential landscape requires a solution to

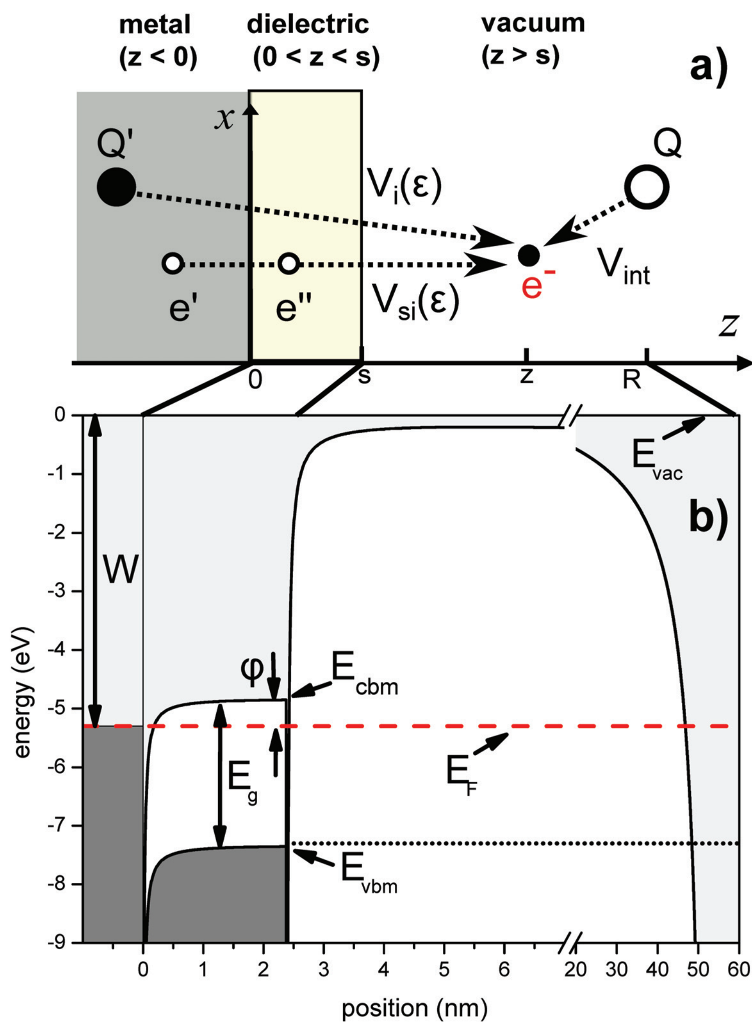

Figure 4.2: (a) Point charge representation of an active electron e^-. The potential is constructed from the superposition of interaction, self-image and electron-"ion-image" terms (V_{int}, $V_{si}(\epsilon)$, $V_i(\epsilon)$). (b) Energy profile along the normal coordinate z when the ion is >50 nm from the metal surface. The parameters are $s = 2.4$ nm for a C_{60} film on an Au(111) substrate with $\epsilon = 4$, E_g = 2.5 eV, W = 5.3 eV, $\phi = 0.5$ eV and ion charge state $Q = 24$.

Poisson's equation with the following general boundary conditions [100, 101],

$$V = 0, \text{ at the metal surface} \tag{4.6}$$

$$\Delta E_{||} = 0 \text{ and } \Delta D_{\perp} = 0, \text{ at the thin film surface .} \tag{4.7}$$

As in the clean metal case, the potential energy of an electron vanishes at the surface of the metal. $\Delta E_{||}$ and $\Delta D_{\perp}$ are the differences in electric field parallel to the surface and electric displacement normal to the surface at the interfaces. Solutions to Poisson's equation that match the boundary conditions in Eqs. 4.6 and 4.7, for metal-insulator-vacuum systems can be obtained using integral representations with the proper boundary conditions in Eqs. 4.6 and 4.7 [102]. The codes used to calulate the potentials are printed in Appendix F.

The ion's potential is constructed by solving Poisson's equation with the appropriate boundary conditions. Following the approach of Refs. [103, 102], we solve Poisson's equation in cylindrical coordinates. z is the normal (axial) coordinate and ρ, is the transverse (radial) coordinate. The electrostatic potential has the form

$$v_{vac} = Q \int_0^{\infty} \{\exp[-m|z|] + A(m)\exp[mz]J_0(m\rho)\}\, dm \tag{4.8}$$

$$v_{film} = \frac{Q}{\epsilon} \int_0^{\infty} \{B(m)\exp[-mz] + C(m)\exp[mz]J_0(m\rho)\}\, dm \tag{4.9}$$

$$v_{metal} = \frac{Q}{\epsilon_{met}} \int_0^{\infty} D(m)\exp[-mz]J_0(m\rho) dm \tag{4.10}$$

where v_{vac}, v_{film}, v_{metal} are the electrostatic potentials in the vacuum, film and metal regions, respectively. These electric potentials are expressed in atomic units where the dielectric constant is set at $e(4\pi\epsilon_0)^{-1}$ = 1 a.u. (see Appendix G).

Note that in this derivation, the origin is set at the ion's position within

the vacuum region, and $z > 0$ defines positions closer to the surface. However, with a geometric transformation, the results of Eqs. 4.8 - 4.10 can be applied to the previously considered coordinate system where the origin is the metal surface. J_0 is a Bessel function of the first kind and the co-efficients A, B, C, D are determined from boundary conditions:

$$\left(v_{vac} - v_{film}\right)_{z=s} = 0, \qquad \left(\epsilon\frac{\partial v_{vac}}{\partial z} - \epsilon_0\frac{\partial v_{film}}{\partial z}\right)_{z=s} = 0 \tag{4.11}$$

$$\left(v_{film} - v_{vac}\right)_{z=z_{met}} = 0, \qquad \left(\epsilon\frac{\partial v_{film}}{\partial z} - \epsilon_{met}\frac{\partial v_{met}}{\partial z}\right)_{z=s} = 0 \tag{4.12}$$

where s is the position of the dielectric - vacuum interface and z_{met} is the position of the dielectric-metal interface. In practice, Eqs. 4.8-4.10 are substituted into Eqs. 4.11 and 4.12 and solved symbolically. Then, the limit $\epsilon \to \infty$ is taken, causing $v_{met} \to 0$ at the surface of the metal. Physically, this means that the electric potential of a test charge goes to zero in a perfect conductor and that electric field lines are excluded (via Eqs. 4.11-4.12).

From the electrostatic potential, the potential energy of the active electron with charge e can be obtained:

$$V(z) = \int_0^e v(z)de. \tag{4.13}$$

The potential energy is referenced with respect to the vacuum energy $V_{vac} = 0$. The potential profile from the ion and its image terms is shown in Fig. 4.3. Here, the potential due to the ion (not including electron self-image), is plotted along the normal coordinate z for film thickness $s = 1.6$ nm and charge state $Q = 26$. The lines plot a range of permittivity values in the thin film from $\epsilon = 1$ (vacuum) to $\epsilon = 10^6$ (ideal conductor). As described above, the displacement vector is con-

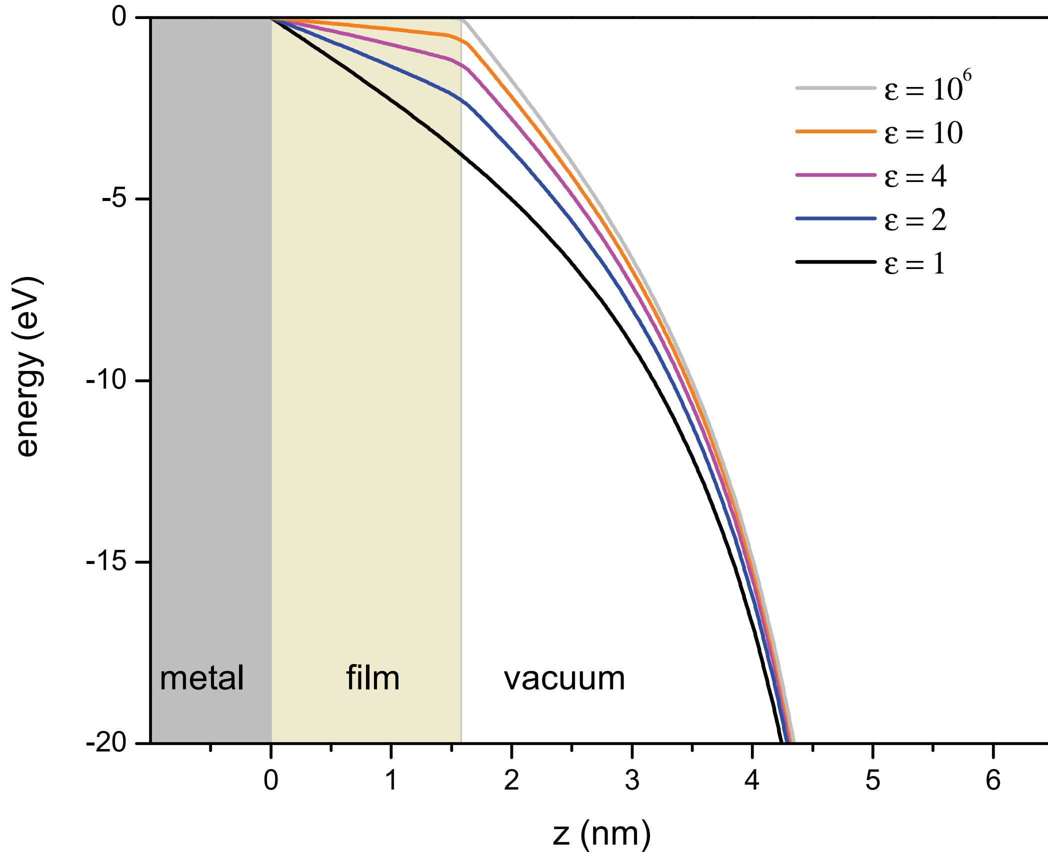

Figure 4.3: Potential that a test charge experiences when a $Q = 26$ ion is at position R = 5.8 nm outside the metal surface covered with $s = 1.6$ nm thick film. ϵ changes the field within the film.

tinuous across the insulator-vacuum interface at $z = s$ and the potential vanishes at the metal surface.

The slope of the ion's potential in the film $(0 < z < s)$, *i.e.*. the electric field, decreases with increasing ϵ. For $\epsilon = 1$, the dielectric region has the same permittivity as the vacuum region, and there is no change to the slope of the potential within the film with respect to the vacuum region. In the limit that $\epsilon \to \infty$, the film behaves as an ideal conductor, and the potential vanishes at $z = s$ satisfying Eq. 4.6.

Dielectric materials have intermediate values of permittivity between these

limits. As shown in Fig. 4.3, the permittivity of the film affects the height of the potential barriers between the target electrons and the ion. To account for time dependent effects, ϵ can be replaced with a frequency dependent dielectric function $\epsilon(\omega)$ [93]. In the discussion below, we work in the adiabatic limit and set $\epsilon(\omega)$ equal to the static permittivity.

4.3.2 Electron self-image

In measurements of electrons trapped in image potential states, it has been observed that the net result of a dielectric slab on a metal surface is that there can be localization of extra electrons near the dielectric film's surface. Additionally, electrons at the dielectric surface are trapped with considerably larger binding energy than occurs in the absence of the metal substrate. To explain this phenomenon, Cole developed an electrostatic model for image potentials at the surfaces of dielectric films on metals [104]. The system is treated with classical electrostatics for a thin homogeneous dielectric slab lying on a metal substrate. This approach is called the dielectric continuum model (DCM). The DCM appears in various forms throughout the literature [105, 106, 107, 108].

Here, we use the dielectric continuum model to determine an electron's self-image (V_{si} in Fig. 4.2(a)). Due to the discontinuity in ϵ across the dielectric-vacuum interface, the image potentials are defined piecewise between the vacuum region outside the film, and inside the film. In the vacuum region, the image potential is:

$$V_{out}(z,s) = \frac{-\beta e^2}{4(z-s)} + \frac{1-\beta^2}{4\beta} \sum_{n=1}^{\infty} \frac{(-\beta)^n}{z-s+ns}. \tag{4.14}$$

The first term is the image potential outside a semi-infinite dielectric, and the sum expresses the series of corrections due to presence of the metal substrate, and the

finite thickness of the film.

Inside the dielectric, the image potential is screened by the dielectric media as ϵ^{-1}. Additionally, within the film, the reference energy becomes the conduction band minimum of the film E_{cbm} instead of the vacuum level:

$$V_{in} = E_{cbm} - \frac{e^2}{4\epsilon z}. \quad (4.15)$$

E_{cbm} is related to the electron affinity (E_A) of the dielectric material by $E_{cbm} - E_{vac} = -E_A$. In our application of the DCM, we make the additional assumption that electrons in the valence band of the dielectric are also influenced by their image attraction to the metal. Therefore, the top of the valence band has energy $E_{vbm} = V_{in} - E_g$.

In Fig. 4.2(b), the potential energy profile is plotted along z for an ion at distance >50 nm from the surface. At this distance the energy levels in the target are unperturbed by the ion's electric field. The surface of the metal is located at $z = 0$. The metal (in the region $z < 0$) is parametrized as a continuum of filled states up to the Fermi energy E_F. The vacuum work function W is the difference between the Fermi energy (E_F) and the vacuum level.

The thin film (in the region $0 < z < s$) is represented by a continuum of filled states up to the valence band maximum (E_{vbm}). Above the valence band, the energy gap E_g separates the valence band from the conduction band minimum E_{cbm}. As described within the DCM, image forces pull down the bands in the dielectric film in close proximity to the metal surface.

4.3.3 Evaluating the critical distance, R_c'

Starting with the potential diagram in Fig. 4.2(b), we pose the question whether electrons in the dielectric or metal transit first, as the ion moves toward the surface. The metal has filled levels up to E_F, but is buried underneath the dielectric film. On the other hand, the surface of the dielectric film is exposed to the vacuum but contains more tightly bound electrons than in the metal ($E_{vbm} < E_F$).

Figure 4.2(b) displays the two relevant energy barriers between metal target electrons and the ion. First, the barrier of approximate height $\phi = E_{cbm} - E_F$, and width s defines an energy gap within the dielectric material. This barrier is defined by the portion of the dielectric's band gap that extends higher than E_F. Second, a vacuum barrier with approximate height W and width $(R - s)$ exists in the region outside the dielectric film ($z > s$).

As the ion approaches the surface, its electric field decreases the heights of both of the barriers until they fall below E_F and transport from electrons in the metal becomes classically allowed. The ion's position outside the target when this classical transport condition is met, is the critical distance R_c' for the onset of neutralization. Alternatively, electrons in the dielectric film could be captured by the ion from the valence band when the height of the vacuum barrier falls below E_{vbm} in the film. The energy barrier preventing the first electron from escaping the dielectric is the binding energy $(E_{vac} - E_{vbm})$. In the thick film limit, the target behaves as a bulk insulator, and the first electron will be captured from the valence band of the dielectric thin film.

The critical distance for a given charge state, therefore, will depend on the initial width and height of the barriers in the film and vacuum regions (for

electrons in either the film or metal). The physical parameters that set the initial height and width of these barriers are the film thickness, film permittivity, and relative alignment of E_{vbm}, E_{cbm}, E_F with respect to the vacuum level. As shown below, these parameters will also determine whether the first electron will be captured from the metal, or the thin film.

Figure 4.4(a)-(c) shows the evolution of the barrier heights in the vacuum, and in the dielectric regions, as the ion $(Q = 24)$ approaches the surface. The metal's Fermi level is plotted as a straight line in each of the plots. The valence band maximum of the dielectric, is plotted as a dotted line. The energy gap in the dielectric, and the non-conducting region of the vacuum, are denoted as white space. The continuum of filled states in the metal and dielectric valence bands is shown in dark gray, and the unoccupied states in the conduction bands are filled in light gray.

Figure 4.4(a)-(c) plots the potential profile in the vacuum and dielectric regions as the ion approaches the target and reaches distances from the metal surface of $R = 10.5$ nm, $R = 7.3$ nm and $R = 5.2$ nm. Parameters are chosen for a $s = 2.4$ nm thick C_{60} film deposited on Au(111). The energy levels were taken from Refs. [4, 109].

Ultrathin C_{60} films have a highest occupied molecular orbital / lowest unoccupied molecular orbital gap of approximately E_g = 2.5 eV and the Fermi energy of Au(111) substrate lies within the band gap ($E_F = -5.3$ eV) of the dielectric film making $\phi = E_{cbm} - E_f = 0.5$ eV [109]. The position of the valence band maximum in the absence of an external field is E_{vbm} = -7.3 eV. Electric permittivity of the film is taken to be $\epsilon = 4$ [110, 111].

As the ion approaches the surface, a maximum in the potential energy profile along z develops in the vacuum $(s < z < R)$ due to competition between

the ion's electric field and the electron's attraction toward the image plane at the surface of the film ($z = s$). This behavior is qualitatively similar to the saddle point in front of a clean metal target seen in Fig. 4.1. In Fig. 4.4, there exists a second potential maximum, that develops within the dielectric material ($0 < z < s$) due to the electron's image attraction toward $z = 0$. As the ion approaches the surface, we evaluate whether classical transport will be allowed first from the valence band of the thin film, or metal. As discussed below, the first classically captured electron comes from the metal, for the parameters plotted in Fig. 4.4.

For an ion distance at $R = 10.5$ nm, in Fig. 4.4(a), the ion's electric field decreases the height of the vacuum barrier, and bends the bands in the dielectric film to decrease the height of ϕ. At this position, electrons in the metal behind the dielectric film are still blocked by the energy gap depicted as the small white area within the film, above E_F. Additionally, a much higher and thicker barrier in the vacuum prevents classical transport from the metal. Electrons at the top of the valence band in the dielectric, are also blocked by the vacuum barrier and no classical transport is allowed.

At the distance of $R = 7.3$ nm (Fig. 4.4(b)), the top of the barrier ϕ within the film has dropped to the energy E_F. Here, only the vacuum barrier prohibits classical transport from electrons in the metal, into the vacuum. Electrons at the top of the valence band in the dielectric, are blocked by the vacuum barrier. Again, no classical transport is allowed.

As the ion arrives at $R = 5.2$ nm in Fig. 4.4(c), the barriers in both the vacuum and dielectric have fallen below E_F. The first electron to be captured by the ion originates from the metal. Electrons at energy E_{vbm} in the valence band of the dielectric cannot escape. This distance is $R = R'_c$, *i.e.*, the critical distance for electron capture by highly charged ions outside a metal covered with a dielectric

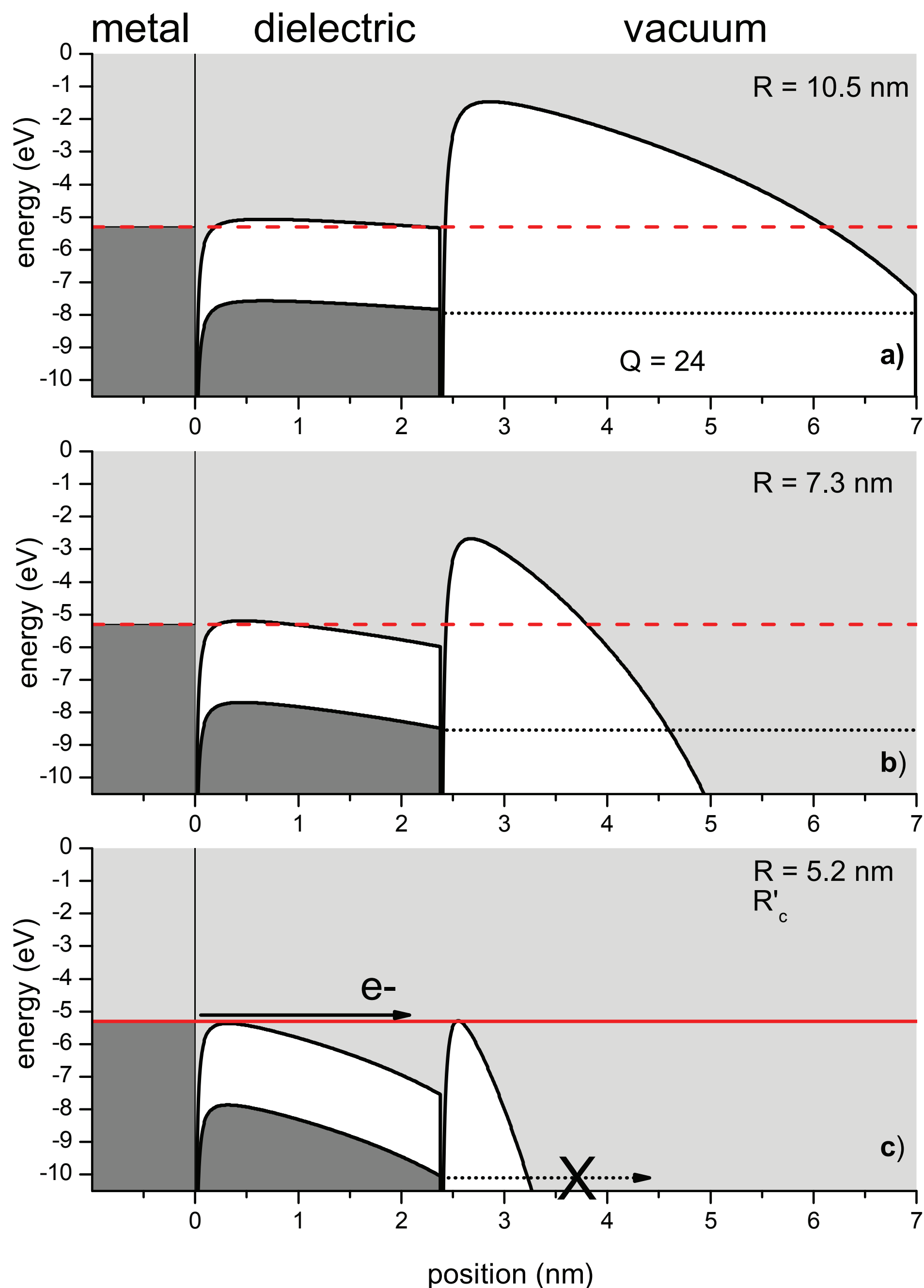

Figure 4.4: Potential profiles for an ion ($Q = 24$) at distances (a) $R = 10.5$ nm, (b) $R = 7.3$ nm and (c) $R = 5.2$ nm away from the metal surface. Film parameters are s = 2.4 nm, $\epsilon = 4$, $E_g = 2.5$ eV, initial $\phi = 0.5$ eV and $E_F = -5.3$ eV (dashed line in (a),(b) and solid line in (c)). The valence band maximum of the dielectric is plotted in each panel (dotted line). Critical distance $R = R'_c = 5.2$ nm is in (c).

thin film.

It is instructive to compare R_c' to the expected critical distance for a clean metal from Eq. 4.5 in the metallic limit ($\beta \to 1$). For a dielectric covered metal surface we find that R_c' = 5.2 nm is greater than the result expected for a clean metal of R_c = 1.9 nm. For this set of parameters, the thin dielectric film enhances the critical distance by more than a factor of 2 compared to a clean metal. In the next sections, we investigate the experimental parameters that lead to the enhancement of critical distance with the deposition of a thin film ($R_c' > R_c$). As will be discussed below, some thin dielectric films can suppress, or completely block classical transport from the metal.

A noteworthy observation about the progression shown in Fig. 4.4, is that the barrier within the dielectric film (ϕ) drops below E_F, before the barrier in the vacuum drops below E_F, as the ion approaches the surface. Therefore, at ion distances slightly greater than R_c', classical capture is limited only by the height of the vacuum barrier. The thin film parameters plotted in Fig. 4.4 lead to a regime of "vacuum limited" capture.

For thicker films, higher barrier ϕ, or higher film permittivity, over-the-barrier transport of an electron in the metal could also be limited by the barrier within the dielectric film ("film limited"). In the "film limited" regime, the vacuum barrier falls before the vacuum barrier, as the ion approaches the surface. The "vacuum limited" regime always leads to an enhancement of critical distance with respect to a clean metal target. The "film limited" regime can lead to either enhancement or suppression of R_c'.

To investigate material parameters of the thin film that influence the height of the potential maximum within the dielectric region, we vary ϵ in Fig. 4.5 for a constant ion position $R = 6$ nm. For comparison, the initial barrier height

$\phi = E_{cbm} - E_F$ (when the ion is far from the surface) is plotted as the black solid line. The valence bands within the dielectric have been removed from the plot for clarity. Inside the film $(0 < z < s)$, the ion bends the conduction band, lowering the barrier ϕ from its initial height. The magnitude of the band bending depends inversely on the ϵ of the film material. In the vacuum region outside the film, the potential maximum also varies inversely with ϵ. In this way, the ϵ of the thin film controls the barrier heights in both the thin film and vacuum regions.

The dashed orange line in Fig. 4.5 plots the potential using the same permittivity and gap parameters as those plotted in Fig. 4.4. However, in Fig. 4.5, the film thickness has been increased to $s = 4$ nm. For the dashed orange line in Fig. 4.5, the ion position is equal to the critical capture distance $R = R_c'$ and the ion can classically capture an electron from the metal.

The blue dotted line in Fig. 4.5 plots the potential inside and outside of the film for ϵ = 10. Increasing the permittivity weakens the electric field within the film as shown in Fig. 4.3, and increases the height of the barrier in the region $(0 < z < s)$. Therefore, the position $R = 6$ nm is greater than the critical distance. The solid green line shows the potential for $\epsilon = 3$, which decreases the barrier heights inside the film and in the vacuum. At $R = 6$ nm, classical transport from an electron in the metal could have been observed at $R > 6$ nm. The trend is that decreasing the permittivity of a dielectric film increases the critical capture distance. For a constant set of target material properties and film thickness we see qualitatively from Fig. 4.5 that $R_c'(\epsilon = 10) < R_c'(\epsilon = 4) < R_c'(\epsilon = 3)$.

To show more explicitly how the critical distance (R_c') depends on the film permittivity (ϵ), Fig. 4.6 plots $R_c'(\epsilon)$ for film thickness $s = 3.2$ nm and charge $Q = 36$ over the range $\epsilon = 3$ to $\epsilon = 10$. As expected, the general trend is that R_c' decreases as ϵ increases from 3 to 10. In the regions of the plot labeled i and

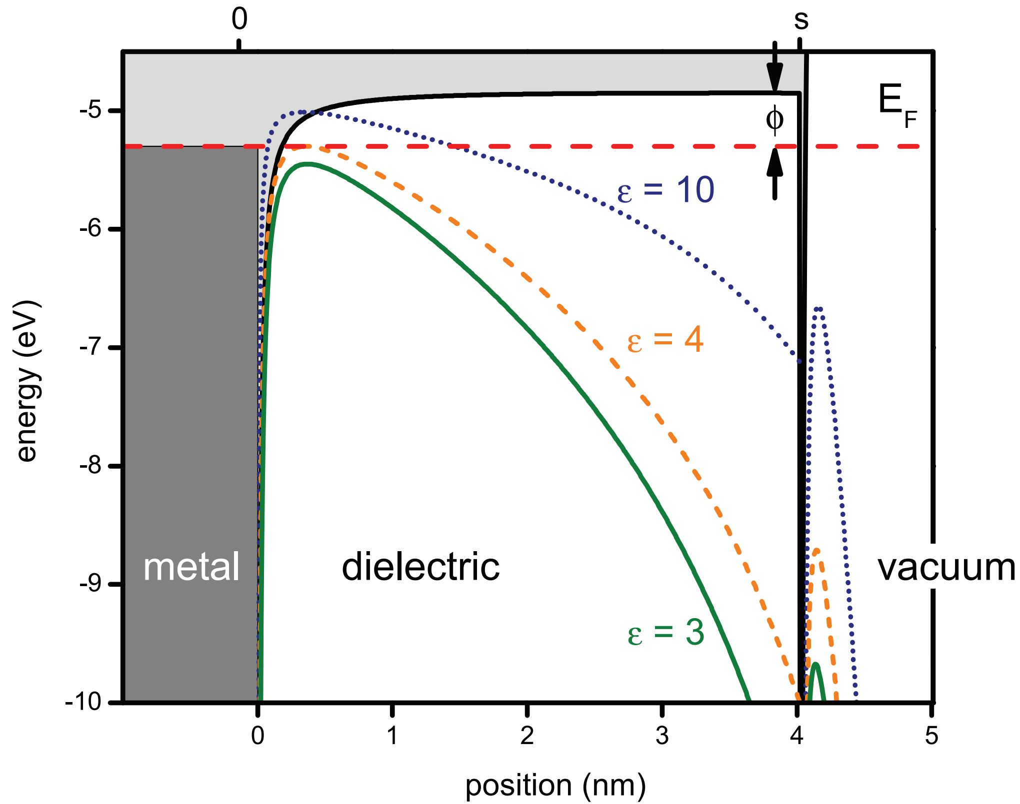

Figure 4.5: Dependence of the potential barrier maximums in the dielectric and vacuum regions on film permittivity. The solid black line plots the unperturbed barrier ϕ within the film ion distance $R > 50$ nm. The other lines are $\epsilon = 10$ (dotted), $\epsilon = 4$ (dashed), $\epsilon = 3$ (solid green) for constant ion position $R = 6$ nm.

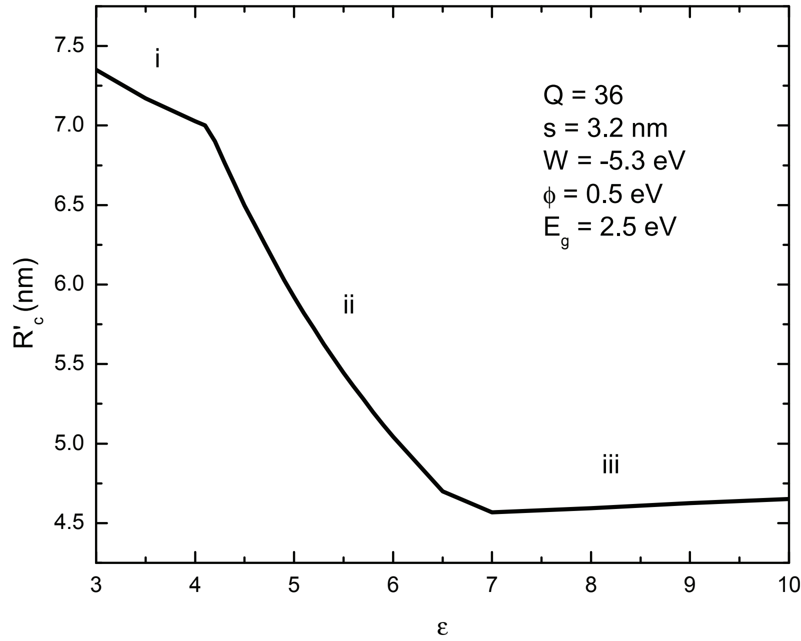

Figure 4.6: $R_c'(\epsilon)$ for $Q = 36$, W = -5.3 eV, $\phi = 0.5$ eV, $s = 3.2$ nm and E_g = 2.5 eV. The three distinct slopes represent regimes i, ii, iii (discussed below).

ii, the first captured electron originates from the metal. As permittivity increases, the electric field needed to pull down the barrier in the film (ϕ) also increases. This means that an ion of a given charge state must be in closer proximity to the target before it can exert the electric field required to pull down the barrier, ϕ. In Fig. 4.6, this is the reason that R_c' decreases with increasing ϵ. In the region of the plot in Fig. 4.6 labeled iii, the first captured electron comes from the filled states in the dielectric film. The three capture regimes (i, ii, and iii) are discussed in detail within Sec. 4.3.4.

Recall that in Fig. 4.4(c), electron capture from the metal was "vacuum limited", *i.e.*, the last potential barrier to fall below E_F before reaching the critical

distance was in the vacuum. Upon increasing the film thickness from $s = 2.4$ nm to $s = 4$ nm, the $\epsilon = 4$ line in Fig. 4.5 demonstrates "film limited" capture from the metal. This means that for ion distances slightly greater than R'_c, the potential maximum in the vacuum has already fallen below E_F. At this instant the only barrier limiting capture is within the dielectric film. The regimes of vacuum and film limited transport become significant in understanding capture distance as a function of film thickness $R'_c(s)$.

4.3.4 Critical distance as a function of film thickness

The critical distance with respect to the metal surface depends on film thickness. Figure 4.7 shows $R'_c(s)$ for different charge states in (a) and film permittivity values in (b). In both panels of Fig 4.7, the band gap, ϕ barrier, and metal work function are the nominal values for C_{60} on Au(111). The solid orange line in both (a) and (b) plots critical distance as a function of film thickness for $\epsilon = 4$ at $Q = 24$.

Vertical intercepts of the lines in Fig. 4.7 represent the clean metal limit where no film is deposited. Eq. 4.5 describes this limit when $\beta \to \infty$. Thus increasing the charge state increases the metal target capture distance $R'_c(s = 0)$ in front of a clean metal as $\sqrt{Q}$ in Fig. 4.7(a).

At each charge state in Fig. 4.7(a), the $R'_c(s)$ lines follow similar qualitative behavior, and possess distinct regimes labeled i, ii, iii. Specifically, R'_c grows in a sublinear manner up to a transition thickness labeled s_1^* on the $Q = 36$ line (regime i). This regime $(0 < s < s_1^*)$ is characterized by "vacuum limited" capture of an electron in the metal. In regime ii ($s_1^* < \mathrm{s} < s_2^*$), the slope of R'_c decreases compared to region i. Regime ii corresponds to "film limited" capture of metal

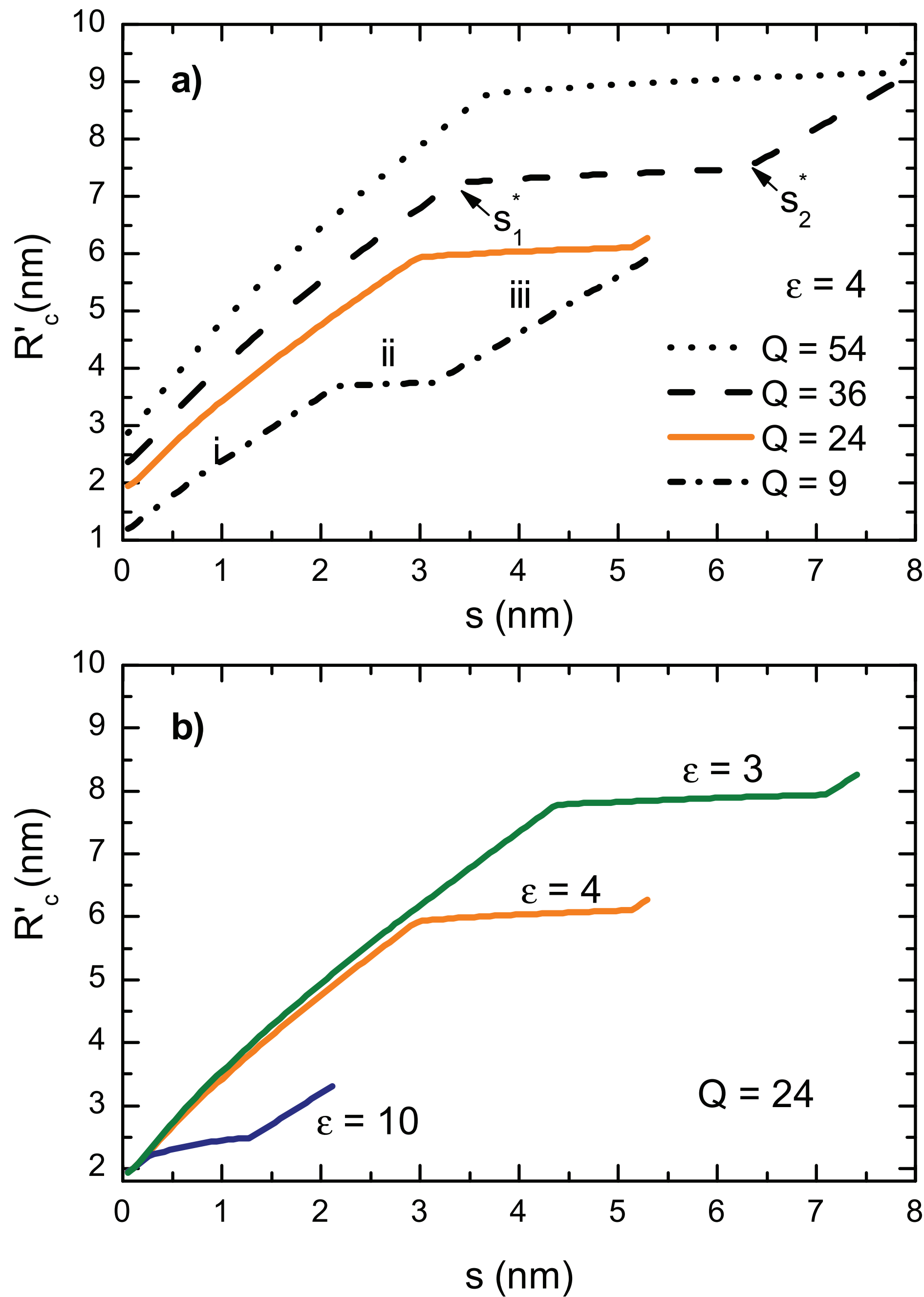

Figure 4.7: (a) $R'_c(s)$ for charge states $Q = 9$, 24, 36 and 54. The first captured electron comes from the metal substrate in i & ii and from the valence band of the dielectric film in iii. (b) R'_s for the parameters in Fig. 4.5

electrons. Regime iii is the thick film regime where $s > s_2^*$. Here, the dielectric begins to behave as a bulk rather than a thin film because the first electron is captured directly from the valence band of the dielectric material. In region iii, R'_c grows linearly as $\propto s$, due to the extension of the surface toward the ion. The vertical intercept of the lines in regime iii is also given by Eq. 4.5, where β is determined by the permittivity of the thick film. In region iii, the classical over the barrier model for bulk insulators is applicable [93].

The transition between vacuum limited (i) and film limited (ii) capture of an electron in the metal at s_1^* can be interpreted in the following way. For a constant R, increasing the film thickness will *decrease* the distance between the ion and image plane at the surface of the film ($z = s$). The strength of the image attraction in V_{out} (Eq. 4.14) scales approximately as $-1/z$, and asymptotes at $z = s$. This means that the magnitude of the image potential grows rapidly as the distance between the ion and the image plane ($z = s$) is decreased. The result is that increasing the film thickness will diminish the vacuum barrier at greater R values. At the thicknesses greater than s_1^*, the film has been extended a sufficient amount such that V_{out} pulls the maximum of the barrier in the vacuum below E_F, before barrier ϕ can be pulled below E_F by the ion's electric field.

Within Fig. 4.7, critical distance is defined as the distance between the metal surface and ion when the first electron is captured over the barrier. For the regime iii ($s > s_2^*$) the electron comes from the valence band maximum in the dielectric as opposed to the metal. Therefore, the quantity ($R'_c - s$) is constant during regime iii, even as s increases. In regime iii, the film has been extended such that the image potential in the vacuum region (V_{out}) pulls the maximum of the barrier in the vacuum below E_{vbm}, before barrier ϕ can be pulled below E_F by the ion's electric field. Electrons in the metal are blocked, when transport from the

dielectric is classically allowed.

The transition thickness s_2^* is a prediction for the film thickness at which there is equal probability of classical capture of an electron from either the metal or dielectric film. At thicknesses greater than s_2^*, electrons will be captured from the valence band of the dielectric, over the vacuum barrier, while electrons in the metal are blocked by the energy gap ϕ within the dielectric film. For $Q = 24$ in Fig. 4.7, the bulk dielectric transition thickness is $s_2^* = 5.1$ nm.

To understand the permittivity dependence of $R_c'(s)$, it is instructive to compare Fig. 4.7(b) to Fig. 4.5. In Fig. 4.5, we show the permittivity dependence of the potential maximums in the vacuum and dielectric, at a constant thickness $s = 4$ nm and ion position $R = 6$ nm. Increasing the permittivity from $\epsilon = 4$ to $\epsilon = 10$ leads to a decrease in R_c' by increasing the heights of potential barriers for a constant ion position R. Decreasing the permittivity from $\epsilon = 4$ to $\epsilon = 3$ allows an increase in critical distance. This permittivity dependent behavior is evident by looking at R_c' for a fixed s value in Fig. 4.7(b). The transition thicknesses s_1^* and s_2^* also have strong dependences on the permittivity of the layer, as shown in Fig. 4.7(b). Both s_1^* and s_2^* decrease with increasing permittivity.

Another implication of Fig. 4.7(b), is that for high ϵ values ($\epsilon > 10$ in Fig. 4.7(b)), the s_1^* thickness becomes much smaller than a typical atomic unit cell. This means that for any continuous film, $s > s_1^*$, there will be no "vacuum limited" regime for electron capture from the metal. An example of this behavior will be discussed below, for the case of Al_2O_3 film on Co.

Consider the film thickness of $s = 3.4$ nm within Fig. 4.7(a). At this thickness, the regime of R_c' will depend on the charge state of the ion. For example, $Q = 9$ is in regime iii, $Q = 24$ is in regime ii and $Q = 54$ is in regime i. We plot the potential profiles for each of these charge states in Fig. 4.8.

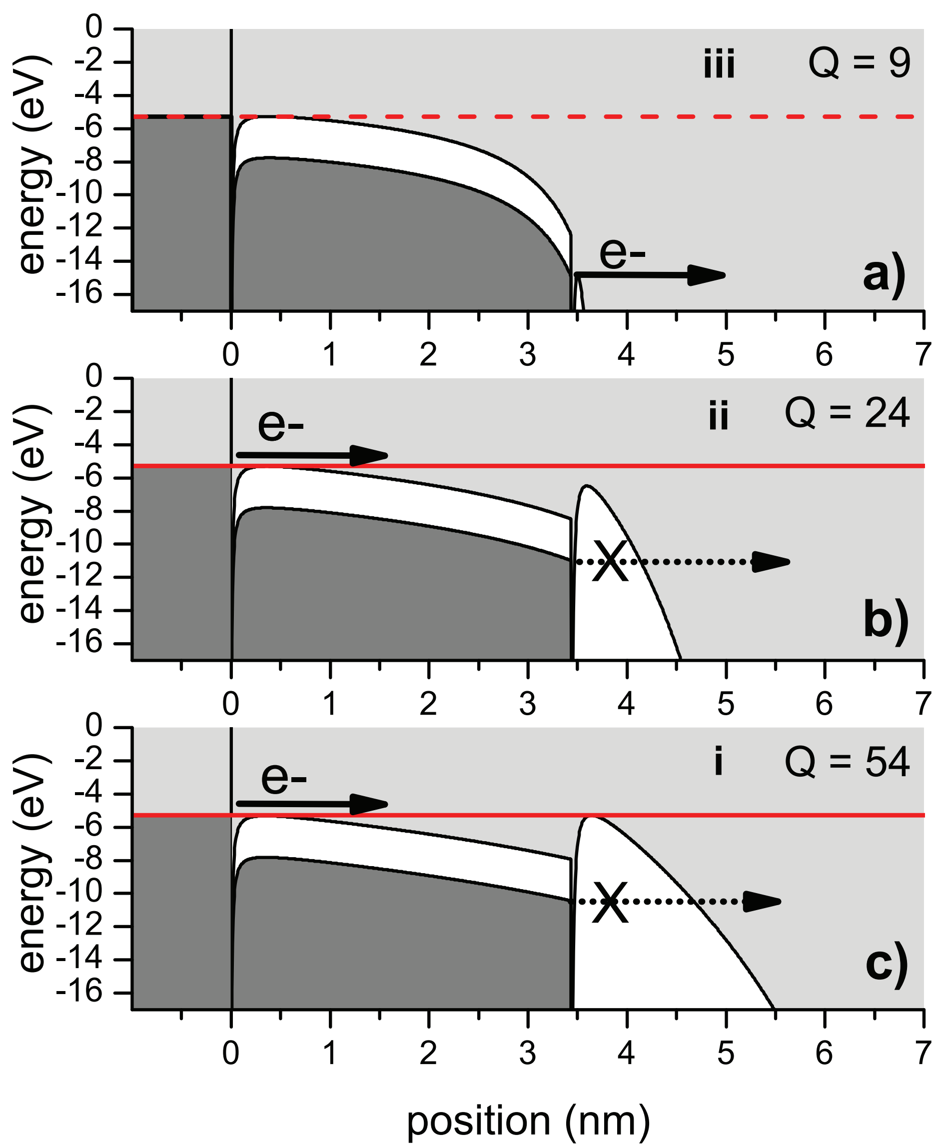

Figure 4.8: Potential plots at R_c' for charge states (a) $Q = 9$, $R_c' = 4.0$ nm (regime iii), (b) $Q = 24$, $R_c' = 6.0$ nm (regime ii) and (c) $Q = 54$, $R_c' = 8.5$ nm (regime i). The target is C_{60}/Au(111) with a film thickness of s = 3.4 nm.

For $Q = 9$ in Fig. 4.8(a), the first captured electron originates from the valence band of the dielectric at a distance R_c' = 4.0 nm from the metal. There remains a small energy gap in the dielectric blocking classical tranport from an electron in the metal, while classical transport from E_{vbm} is classically allowed. Fig. 4.8(b), exemplifies "film limited" transport from the metal. This means that at distances slightly larger than $R_c' = 6.0$ nm, the barrier height in the vacuum is less than E_F so that the only limiting energy barrier lies within the thin film. Fig. 4.8(c) shows "vacuum limited" transport from the metal. Here, the barrier in the dielectric falls below E_F before the barrier in the vacuum falls below E_F and an electron is captured from the metal at an ion distance of R_c' = 8.5 nm. The panels (a), (b) and (c) give representitive positions of the potential maximums in the vacuum and dielectric for each of the regimes.

4.3.5 Work function dependence

To further illustrate the difference between the "vacuum limited" (regime i) and "film limited" (regime ii) behaviors, we plot $R_c'(s)$ for a range of metal work functions between 4 eV and 7 eV in Fig. 4.9, leaving the barrier height and the dielectric parameters unchanged. In order to keep the height of ϕ constant, E_{cbm} changes with the metal work function. Changing the work function of the metal and leaving all other parameters constant allows a clear demonstration that only the barrier within the film limits transport from the metal in the regime ii where $s_1^* < s < s_2^*$. For film thicknesses below s_1^*, the vertical intercept of R_c' has a relatively strong $(1/W)$ dependence on work function. Additionally, s_1^* increases by approximately 2 nm as W increases from 4 eV to 7 eV. In the region ii ($s_1^* < s < s_2^*$), critical distance is *independent on the metal work function*. The lines

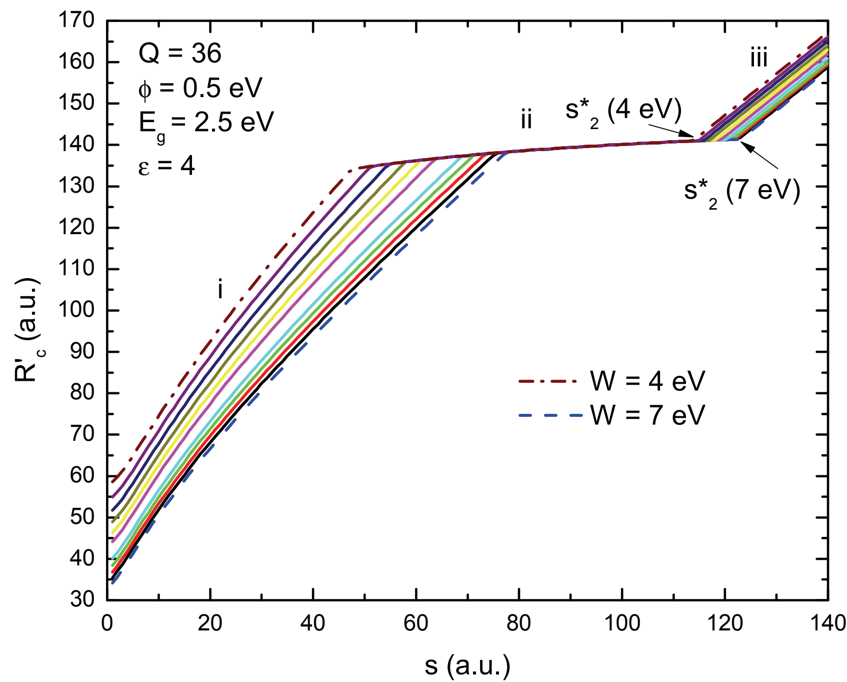

Figure 4.9: Metal work function dependence of critical distance as a function of film thickness. Each line was plotted with the parameters printed in the figure and W was varied between 4 and 7 eV.

plotted with different work functions are indistinguishable. The barrier height ϕ, permittivity and charge state determine the $R_c'(s)$ in region ii. The transition s_2^* (to capture from the dielectric) has a weak dependence on work function, *i.e.*, it increases by only a few Angstroms as W increases from 4 eV to 7 eV.

4.4 Comparison with experiment

4.4.1 C_{60}/Au(111): Electron emission yield

Critical distance may be correlated with an experimental observable such as electron emission yield, assuming that the total potential emission per incident ion is proportional to the above-surface interaction time ($\tau' = R_c'/v_p$). R_c' determines the onset of neutralization and may be proportional to the total yield of Auger electrons emitted above the surface, before impact. The experiment in Ref. [4] reports measurements of electron emission yields for Xe^{24+} incident on C_{60} covered Au(111) at an incidence angle of 40° at 70 keV. Yield due to kinetic emission is negligible in the measurement. Figure 4.10(a) is taken directly from Ref. [4]. In Fig. 4.10(a), the relative secondary electron yield is plotted as a function of C_{60} film thickness Θ, in monolayers (ML). Here, relative secondary electron yield is defined as

$$\gamma^{rel}(\Theta) = \frac{\gamma^{C_{60}}(\Theta)}{\gamma^{Au}(\Theta = 0)} \tag{4.16}$$

where γ is the number of secondary electrons emitted per incident ion, and $\Theta = s/t_{ML}$. The thickness of a C_{60} monolayer is in the range of $t_{ML} \approx$ 0.7 to 0.8 nm [4]. In Fig. 4.10(b), we plot the critical distance normalized by critical distance at $s = 0$ nm (R_c'/R_c) from 0 to 6 ML. The thickness of a single monolayer of C_{60} was taken to be t_{ML} = 0.75 nm. The quantity (R_c'/R_c) is proportional to the relative

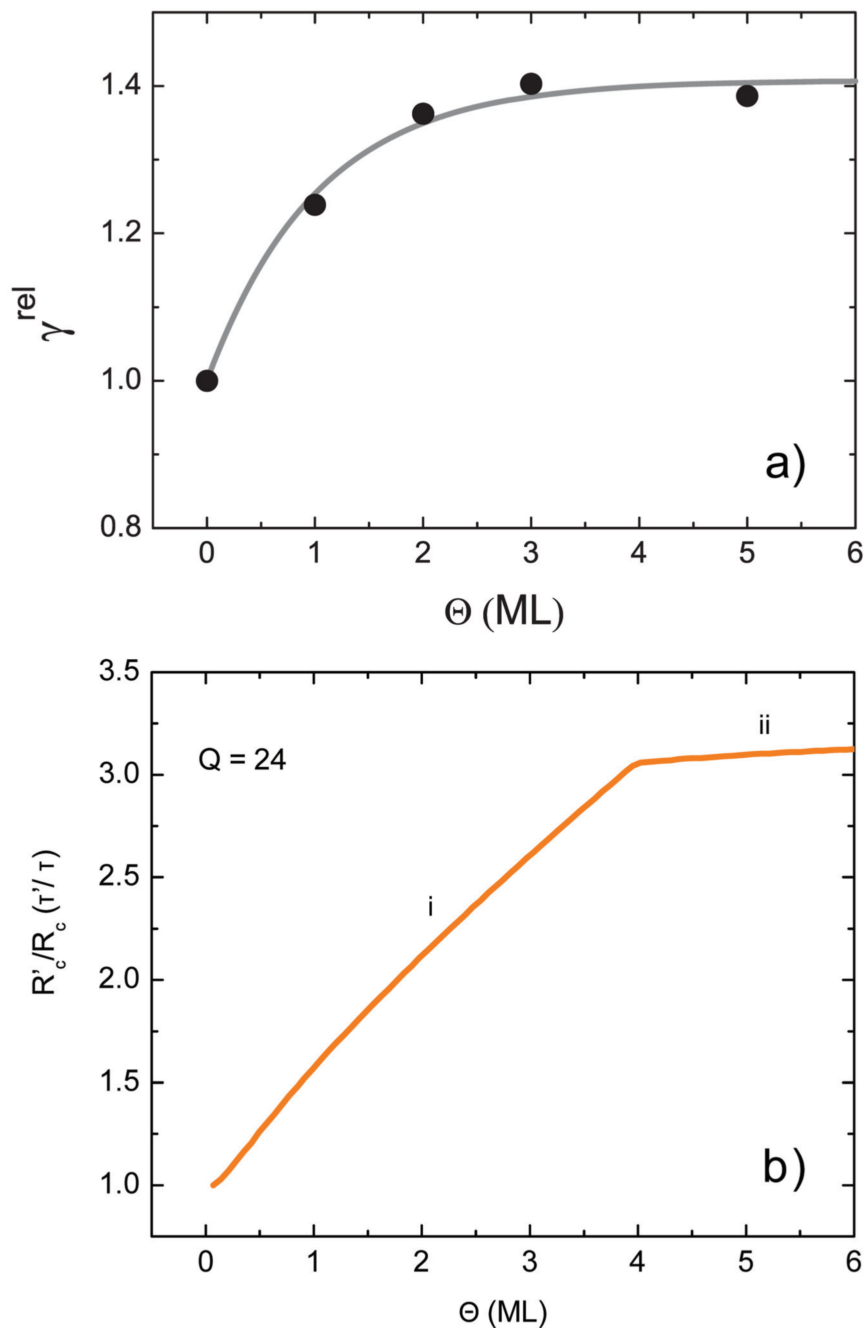

Figure 4.10: (a) Relative emission yield measurements for Xe^{24+} incident on C_{60} covered Au(111) taken from Ref. [4]. (b) Film thickness dependent critical distance (R'_c) normalized by the critical distance for a clean metal. The horizontal axis in (b) is determined by $\Theta = s/t_{ML}$ where $t_{ML} = 0.75$ nm.

increase in interaction time due to the thin film (τ'/τ). The charge state in both Fig. 4.10 (a) and (b) is $Q = 24$.

Again, the knee in the line in Fig. 4.10(b) corresponds to the transitions between regimes i and ii at $s_1^* = 3$ nm (4 ML). Comparing panels (a) and (b) in Fig. 4.10, we make several observations. First, for the film thicknesses used in the experiment, the model predicts that the first captured electron originates from the metal and not the C_{60} film. All thicknesses shown in Fig. 4.10(a) are below the thickness $s_2^* = 5.1$ nm (6.8 ML) calculated for Xe^{24+}. Second, based on the model, we expect enhanced critical distances for thicknesses below $s_2^* = 5.1$ nm. These thin film enhanced critical distances shown in (b) follow the behavior of the increase in relative yield observed in the data in (a). One possibility is that enhanced capture distances lead to enhanced yields by increasing above-surface interaction time. Third, the saturation in relative yield shown in (a) occurs at thicknesses ($s \approx 2$ nm or 2.7 ML) that are close to the calculated s_1^*. For $Q = 24$, the transition from the "vacuum limited" to the "film limited" regimes occurs at $s_1^* = 3$ nm (4 ML). It is plausible that the saturation in relative yield in the data in (a) occurs near s_1^* due to this transition.

In Fig. 4.11 we plot modeled $R_c'(s)$ for charge states $Q = 9$, 24, 36 and 54. These are the same charge states as those plotted in Fig. 4.7(a). At thicknesses greater than s_1^*, the enhancement ratio $R_c'(s)/R_c$ levels off at approximately 3 for all charge states. This behavior mimics the charge-independent saturation in relative emission yield reported in Ref. [4]. The gray line in Fig. 4.10(a) is an exponential gain curve with a characteristic thickness Θ_{ch} that saturates at a nearly *charge independent* value $\gamma_{rel}^{\infty} = 1.35$. If γ^{rel} goes with R_c'/R_c, then the Θ_{ch} should depend on Q. Specifically, we predict that higher charge states would lead to higher characteristic thicknesses in the fit to an exponential gain curve.

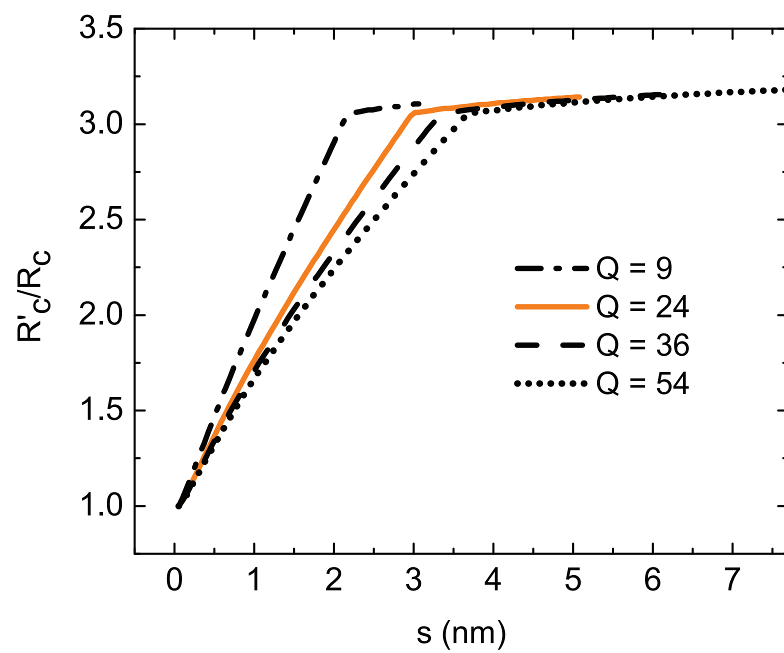

Figure 4.11: $R'_c(s)$ in regimes i and ii for $Q = 9$, 24, 36 and 54 for a C_{60}/Au(111) target.

Additionally, if R'_c/R_c were related to γ^{rel}, a drop-off in relative emission yield would be expected for films with $s > s_2^*$, as the target gains the properties of a bulk dielectric. For $Q = 24$, the model predicts this transition to occur at $s_2^* > 5.1$ nm (at least 7 ML).

4.4.2 LiF/Au(111)

Lithium fluoride in bulk is an ionic crystal with a large band gap $E_g = 14$ eV and binding energy ($E_b = E_{vac} - E_{vbm} = 12$ eV). In bulk its conduction band exists in the positive continuum, above the vacuum level. In the formalism of our model, the presence of a large band gap means that electrons in the metal would be blocked by an initial barrier ϕ whose height exceeds the typical vacuum work function of a metal.

The above-surface KLL Auger electron spectra during neutralization of O^{6+} and N^{7+} in Refs. [2, 3] imply a strong suppression of R'_c even after only 1 ML of LiF growth. The authors concluded that 1 ML of LiF is sufficient to effectively "shield" the Au substrate during the neutralization sequence. Thin LiF films cause a delay in the onset of first capture and decrease the rate of above-surface neutralization [2]. However, the large gap observed in bulk LiF develops [2, 3] only after thicknesses of about 5 monolayers (LiF has a lattice constant a = 0.402 nm [112] with cubic structure). In contrast to the bulk band gap, LiF develops the high binding energy of bulk LiF ($V_{vac} - E_{vbm} = 12$ eV) even at sub-monolayer thicknesses. Thus, the authors concluded that the large binding energy (and not the band gap) was the limiting factor in determining the onset of above-surface neutralization. In short, the binding energy of an electron in the thin dielectric film was held primarily responsible for the observed suppression in the above-surface

component in the Auger spectra.

To analyze this scenario using the model, we plot the distance between the ion and surface at the onset of neutralization (R'_c), as a function of film thickness for a $Q = 7$ projectile outside the surface of LiF/Au(111). The LiF films are parametrized as having permittivity $\epsilon = 9$ and binding energy $(E_{vac} - E_{vbm}) = 12$ eV. The solid lines in the plot represent the expected capture distances from Eq. 4.5 in the bulk metallic, and bulk dielectric limits. To investigate the role of the band gap in the suppression of electron capture, we varied the band gap of the LiF films between the bulk value $E_g = 14$ eV and a reduced value of $E_g = 6$ eV. The results for $E_g = 14$ eV, $E_g = 7.5$ eV and $E_g = 6$ eV are plotted in Fig. 4.12. In our model, we reference the barrier in the dielectric film to the Fermi energy of the metal as $\phi = E_b + E_g - E_F$. Therefore the band gaps $E_g = 14$ eV, $E_g = 7.5$ eV and $E_g = 6$ eV correspond to barrier heights in the dielectric of $\phi = 7.3$ eV, $\phi = 0.8$ eV, and $\phi = -0.7$ eV respectively.

For the smallest band gap $E_g = 6$ eV, the barrier within the dielectric film vanishes $(\phi < 0)$ eV, and the dielectric film facilitates the capture of electrons in the metal. Increasing the band gap to $E_g = 7.5$ eV, the model shows capture of electrons from the metal behind the ultrathin ($s < 0.5$ nm) LiF film. However, the film suppresses the capture of metal electrons below $s < 0.5$ nm. The onset of capture is delayed for film thicknesses comparable to 1 ML of LiF, as seen in the experiment. Finally, for the full band gap $E_g = 14$ eV we observe an even stronger suppression of R'_c. The first captured electrons come from the valence band of the LiF, and not the metal. This leads to decreased capture distances compared to a clean gold target (Fig. 4.12; short blue dashes). Consequently, the blue dashed line converges to the capture distance given in Eq. 4.5.

For comparison, the bulk dielectric and bulk metal limits for R'_c are shown

as solid black lines in Fig. 4.12. These were obtained using Eq. 4.5 with permittivities of $\epsilon \to \infty$ for the metal and $\epsilon \to 9$ for the LiF film. The effective "work function" for the dielectric is its binding energy $E_b = E_{vac} - E_{vbm}$. Again, the R_c' are plotted in Fig. 4.12 with respect to the surface of the metal at $z = 0$. This means that the distance between the ion and the metal surface at the position of capture grows linearly with s when the electron originates from the dielectric.

The most realistic scenario is the presence of a non-zero yet reduced band gap $E_g = 7.5$ eV. The presence of a non-zero, yet reduced band gap in ultrathin LiF film is supported by measurements [113, 114]. On the other hand, LiF possesses the high binding energy ($E_b = 12$ eV) at sub-monolayer coverages. In the context of our model, it is difficult to explain the experimentally observed suppression of the onset of capture without the existence of an energy gap in the thin film. Delaying the onset of capture requires a non-zero energy barrier ϕ in order to block resonant capture of electrons from the metal. Entirely removing the ϕ or band gap in the model leads to an enhancement of R_c' via "vacuum limited" capture of an electron from the metal (in contrast to Ref. [2]).

To summarize our comparison between the model and data we make the following comments. Suppression of the onset of above-surface neutralization is expected at coverages of approximately 1 ML of LiF given a reduced (but non-zero) band gap. Even a dramatically reduced LiF band gap ($E_g = 7.5$ eV; solid red line in Fig. 4.12) is sufficient to suppress the onset of neutralization. If no band gap is present in the LiF, we model an increase in the electron capture distance; there is no barrier ϕ to limit classical transport of electrons in the metal (dashed-dotted gray line in Fig. 4.12). Enhancement of R_c' at 1 ML coverage is in disagreement with the measured above-surface KLL Auger spectra for O^{7+} [2, 3]. The complete absence of a band gap within the LiF film causes an inconsistency between the

model and experiment.

A scenario consistent with both model and experiment is that even for ultrathin LiF films (around 1 ML) there exists a non-zero band gap, that is reduced with respect to the band gap in bulk LiF. In this case, above-surface neutralization begins with over-the-barrier capture of an electron from the metal, and not the LiF film. The limiting factor determining the onset of neutralization (from capture of metal electrons) is then the height of the barrier ϕ which is based on the relative alignment of E_F in the metal and E_{cbm} in the LiF film. This scenario involving initial capture of metal electrons, is different than the one proposed in the Refs. [2, 3], wherein the binding energy $(E_b = E_{vac} - E_{cbm})$ was the limiting energy barrier. Here, we propose that the capture of electrons from the metal behind the LiF film remains consistent with delayed onset of neutralization observed in the Auger spectra.

4.4.3 Al_2O_3/Co

Thin aluminum oxide films on cobalt were the experimental system studied in Ch. 3 and Ref. [1]. Al_2O_3 is considered a "high-k dielectric" with static permittivity of approximately $\epsilon = 8$ (for plasma oxidized thin films [115]). The nominal band gap of bulk aluminum oxide ($E_g = 9.9$ eV) is smaller than that of bulk lithium fluoride. As with all materials fabricated as ultrathin films, the electronic properties are sensitive to preparation conditions, *e.g.*, band gap differences may occur depending on whether plasma oxidation, thermal oxidation or atomic layer deposition are used [116]. For plasma oxidized barriers, the energy difference between the metal Fermi energy and dielectric conduction band minimum was found to be $\phi = 1$ eV. This quantity can be determined by performing

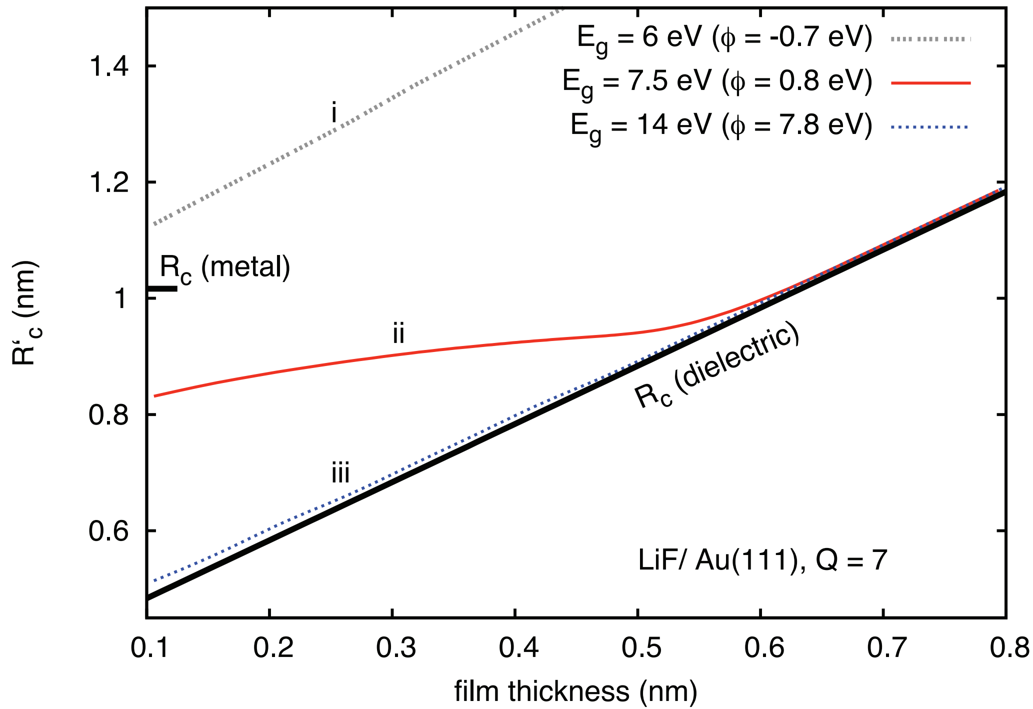

Figure 4.12: $R'_c(s)$ for $Q = 7$ outside LiF/Au(111). Electrons in the dielectric have fixed binding energy 12 eV. With (bulk) band gap $E_g = 14$ eV the first capture proceeds from the dielectric. A reduced band gap $E_g = 7.5$ eV leads to capture from the metal with suppressed R'_c below $s = 0.5$ nm. $E_g = 6$ eV facilitates capture compared to a clean metal due to $(\phi < 0)$ eV.

tunneling spectroscopy measurements of Co/Al_2O_3/Co junctions (*cf.* Ch. 2). The Fermi energy lies within the band gap of the dielectric.

Fig. 4.13 plots critical distance as a function of aluminum oxide film thickness, given the target parameters $E_g = 9.9$ eV, $\epsilon = 8$, $\phi = 1$ eV, $W = 5$ eV. The charge state in the plot is $Q = 44$ (the highest charge state used in Ref. [1]). The two distinct slopes in the $R_c'(s)$ line are regions ii (film limited capture from the metal) and iii (capture from the dielectric). The transition s_2^* occurs at a thickness of 1.3 nm.

Capture from the metal limited by the vacuum barrier does not occur within the range of thicknesses plotted. This means that the distance of first capture does not depend explicitly on the work function of the metal substrate in ultrathin films (when $s < s_2^*$). Instead, the significant quantity limiting capture of metal electrons is the relationship between E_{cbm} and E_F. The barrier in the dielectric ϕ serves as the barrier limiting the capture of electrons from the metal. Also, for all $s > 0$ nm, critical distance is suppressed compared to a clean Co target. R_c for the clean Co ($W = 5$ eV; $W = 44$) from Eq. 4.5 is indicated at $s = 0$ nm in Fig. 4.13.

Although, the capture distance is suppressed due to the presence of the film, the first captured electron does originate from the metal substrate behind the exposed dielectric film at thicknesses up to 1.3 nm. At thicknesses greater than 1.3 nm, the target begins to take on the properties of a bulk aluminum oxide target. Specifically, capture is limited by the high vacuum barrier between the valence band electrons in the aluminum oxide layer, and the ion. Target electrons in the dielectric have an effective binding energy of $(E_{vac} - E_{vbm}) = 13.9$ eV.

In the context of material modifications experiments [1], the prediction of above-surface capture of an electron from the metal may provide insight into dam-

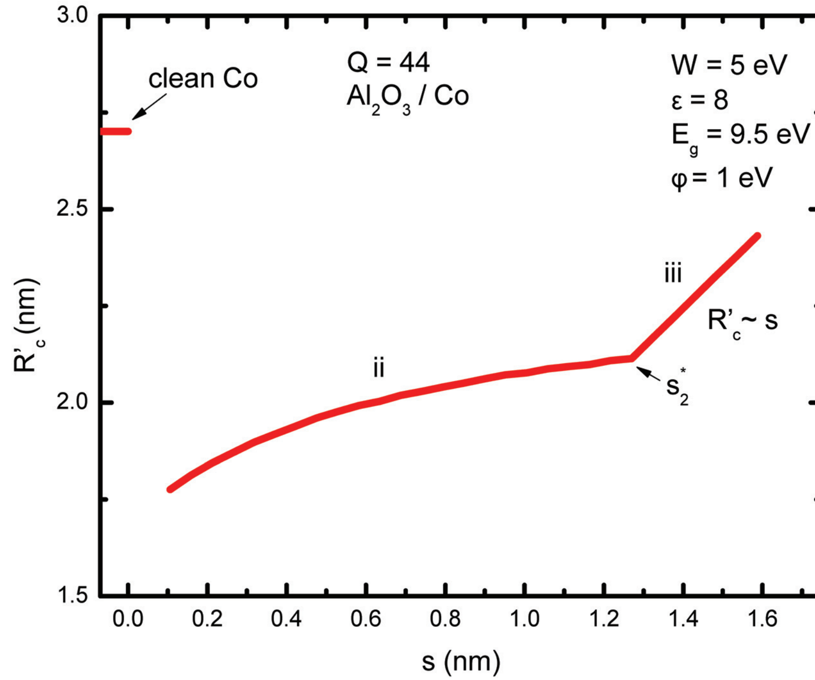

Figure 4.13: Thickness dependent critical distances for $Q = 44$ interacting with Al_2O_3 films on Co. Vacuum limited transport from the metal (i) does not occur at any s due to relatively high ϕ and ϵ parameters. Instead, barrier ϕ limits the capture of metal electrons and suppresses the capture distances R_c' (ii). The target behaves as a bulk dielectric beyond $s_2^* = 1.3$ nm.

age mechanisms. For example, the Coulomb explosion scenario [117] describing destabilization of a dielectric material via rapid charging, would not be consistent with initial removal of free charge in the metal substrate. Rather, if charge is removed from the metal instead of the dielectric film during above-surface neutralization, this suggests that modification of the thin film occurs upon ion impact. A more likely scenario is that the film suffers most damage via emission of sub-surface Auger electrons that couple to phonons in the film material to cause heating. Another possibility is that after initial capture from the metal, above-surface Auger electrons are re-radiated toward the target to deposit energy.

4.5 Summary

The results of the model for the three material systems discussed in the previous section are summarized in Table 4.1 at film thickness $s = 1$ nm, and $Q = 36$. For C_{60} on Au(111), the 1 nm film increases the distance for the onset of neutralization. Neutralization starts with electrons in the metal (in the "vacuum limited" regime i) . The relative enhancement of capture distance compared to the metal is R'_c/R_c = 1.8. In the Al_2O_3/Co system, capture still proceeds from the metal at 1 nm thickness, but the film slightly suppresses the capture distance by a factor $R'_c/R_c = 0.8$. The $s = 1$ nm film induces a "film limited" capture regime (regime ii). Here, R'_c is limited by the barrier ϕ, within the dielectric and not the vacuum work function (W). In LiF/Au(111), a film thickness $s = 1$ nm blocks capture from the metal. The first captured electron comes from the valence band of the LiF film. In this case (region iii) the captured electron starts within the target at the position closer to the ion at a position s. Therefore, the distance between the ion and captured electron is $(R'_c - s)$. In comparing capture from the dielectric film to capture from the clean metal, we examine the ratio $(R'_c - s)/R_c = 0.4$. The asterisk in the second row of Table 4.1 denotes this $R'_c \rightarrow (R'_c - s)$ correction that accounts for the initial position of the captured electron. In this calculation, we assume that the full bulk band gap $E_g = 14$ eV is present within the dielectric at all thicknesses. As discussed previously, the presence of a non-zero band gap is required to explain the delayed onset of neutralization observed in the experiment [2].

In this chapter we presented an extention of the classical over the barrier model [23] to examine the first stage of neutralization for HCIs outside dielectric thin films on metals. Classical electrostatics were used to construct the potential

film / substrate	regime	R_c' (nm)	R_c (nm)	R_c'/R_c	note
C_{60} / Au(111)	i	4.0	2.3	1.8	enhancement
LiF / Au(111)	iii	0.9*	2.3	0.4	suppression; *origin is z = s
Al_2O_3 / Co	ii	1.9	2.4	0.8	suppression

Table 4.1: Summary of critical distances at $Q = 36$ and $s = 1$ nm for three experimentally studied systems [1, 2, 3, 4]. The regimes correspond to, i: electron capture from the metal (vacuum limited), ii: electron capture from the metal (film limited), and iii: electron capture from the dielectric film. Parameters for each material system are displayed in the previous figures.

profile for an "active electron" in a metal-dielectric-vacuum system in the presence of a HCI. The inclusion of a dielectric thin film leads to a significant modification of boundary conditions. Electron self-image was treated with the well-known dielectric continuum model. Over the barrier capture distances as a function of film thickness were obtained. We find that the first resonantly captured electron can be captured over-the-barrier either from filled states in the metal or dielectric, depending on the permittivity, band gap and thickness of the film. Additionally, the thin film can either enhance or suppress the onset of neutralization. Within an $R_c'(s)$ plot we observed the following qualitative structure:

1. Regime i (vacuum limited): first captured electron comes from the metal. The onset of neutralization is enhanced with respect to the clean metal. This regime occurs for ultrathin films $s < s_1^*$ for low barrier heights ϕ and low permittivity values ϵ.

2. Regime ii (dielectric film limited): First captured electron comes from the metal. The onset of neutralization can be either enhanced or suppressed, depending on ϕ and ϵ. R_c' is independent of the metal's vacuum work function, and instead depends on the barrier $\phi = E_{cbm} - E_f$. Regime ii

occurs for thicknesses ($s_1^* < s < s_2^*$).

3. Regime iii (capture from dielectric): The dielectric film blocks the capture of metal electrons and suppresses the onset of neutralization when $s > s_2^*$. The film shields the metal electrons and the target behaves as a bulk dielectric as described in Ref. [93].

Quantitative values of the transition thicknesses s_1^* and s_2^* are given for various high charge states in the systems C_{60}/Au(111), Al_2O_3/Co and LiF/Au(111). The behavior of $R_c'(s)$ closely resembled the measured thickness-dependent enhancements in the relative emission yield reported in [4]. Agreement with the observed suppression in the onset of neutralization from the LiF/Au(111) experiment [2] required including a non-zero, reduced band gap in the model of $E_g = 7.5$ eV. It was found that even a reduced band gap was sufficient to model the suppression in above-surface Auger data from the experiment. A comparison between the model and the Al_2O_3/Co system from Ref. [1], showed that for thin films ($s \approx 1$ nm), the first captured electrons originate from the metal.

Chapter 5

Conclusions

5.1 Summary of results

5.1.1 Energy deposition

In chapter 3, we reported the ion induced crater depths in ultrathin dielectric films as a function of projectile charge state. From the depth scaling of the craters with charge state, we determine the energy deposited into the thin film in HCI-surface impact increases from 8 keV to 25 keV as Q increases from 26 to 44. Accounting for both pre-equilibrium kinetic energy loss and neutralization energy, we measure that at least $f = (27 \pm 2)$ % of the available neutralization energy contributes to crater formation. This result represents a lower bound for the fraction of HCI neutralization energy required to form a permanent material defect.

We emphasize that the uncertainty assigned to the result f does not include any propagation of uncertainty in the stopping power model from Ref. [35]. This model represents an upper bound for the pre-equilibrium kinetic energy deposi-

tion. Our approach was to bound the expected kinetic energy loss by measured values from experiment and SRIM for $Q = 1$ and extrapolate to higher charge states using Biersack's model. Comparison to the limited experimental data for highly charged Xe penetrating C foils, shows that the extrapolation is reasonable in terms of the magnitude of energy loss enhancement [45].

Stopping during slow (<25 keV / u) HCI-solid interactions represents a mechanism for kinetic energy deposition which is distinct from the observed behavior of either swift HCIs or slow singly charged ions. For swift heavy ions, most kinetic energy of the projectile is lost to the electrons in the target [29]. For slow singly charged ions, kinetic energy is transfered through a series of quasi-binary collisions that propagate momentum between adjacent target nuclei in a cascade.

However, in the case of slow HCIs, the binary collision approximation breaks down, as the $Q \gg 1$ projectile's Coulomb interaction reaches beyond its nearest neighbors. This Coulomb interaction radius is expected to be especially large in insulator targets, where there are no free charges to screen the ion [35]. The momentum transferred to the nuclei within this interaction radius is proportional to the ion's interaction time with these atoms (inversely proportional to the velocity of the ion) [35]. The result is that momentum transfer to the nuclei becomes increasingly efficient and long range at lower incident energy.

Though enhancement of pre-equilibrium stopping has been observed as an enhanced loss of KE in foil transmission experiments [45, 118], increased damage due to this increased energy loss has never been measured. Tunnel junction based measurements may be an ideal way to detect pre-equilibrium stopping power that occurs within an insulating barrier layer thinner than the charge equilibration length. By keeping Q constant in an experiment while changing KE, it would be

possible to tune only the kinetic energy deposition while keeping E_Q constant.

5.1.2 Electron capture

Chapter 4 presents a classical model for understanding the initial charge transfer between the target and ion for metal substrates covered with thin dielectric films. We found that using the parameters from recent experiments (*e.g.* $s < 5$ ML; C_{60} / Au(111)), the first captured electron comes from the metal behind the thin film. Also, the presence of a thin film enhances the distance at which the ion can capture electrons classically. As film thicknesses increase we find three distinct regimes for the onset of above-surface neutralization:

i. Charge transfer from the metal (limited by the vacuum barrier).

ii. Charge transfer from the metal (limited by the thin film barrier).

iii. Charge transfer from the valence band of the dielectric.

The model is consistent with the observation of increased electron emission yield for the target C_{60} covered Au(111), relative to clean Au(111) [4]. In the context of our model, we attribute the enhanced yield to an increase in above-surface interaction time, after first capture. The increase in interaction time enhances the yield of emitted Auger electrons.

Applying the model to LiF / Au(111), we find that the thin film suppresses the onset of neutralization even for very small thicknesses. Using a reduced band gap, we predict that a single monolayer of LiF gives first electron capture from the metal limited by the barrier within the film, and that capture distance is reduced relative to the clean substrate. This prediction is consistent with the experiments [2, 3]. The model predicts that the reduced band gap present for very thin (1 ML) films leads to first capture from the metal (not the dielectric). Therefore, we

suggest that the limiting factor in neutralization is not the LiF binding energy as proposed in Refs. [2, 3], but is instead the barrier ϕ determined by the relative alignment of the metal Fermi energy with the conduction band minimum in the dielectric.

We also suggest that by depositing thicker films, one should observe a transition corresponding to thickness s_2^* (transition to bulk dielectric), where the above-surface component of the electron emission yield would decrease. For C_{60}/Au(111) using charge state $Q = 24$ the transition to bulk dielectric behavior occurs around $s = 7$ ML.

Chapter 6

Proposals for future experiments

6.1 Calorimetry

One method of measuring energy deposition by ion impact is through a measurement of target's increase in temperature during irradiation. This technique has been employed previously for a measurement of deposited energy from Ar^{Q+} incident on Cu, for charge states up to $Q = 9$ [119].

Calorimetry is a direct measurement of the total energy deposition because excitations occurring in the solid after an ion impact are eventually converted to heat. The total input power to the target is,

$$P_t = \frac{\Delta E_{kin} + \Delta E_Q}{Qe} I \tag{6.1}$$

where ΔE_{kin} and ΔE_Q are the deposited fraction of the kinetic and potential energy, for each ion impact and the beam current incident on the detector is I. The relative retained fraction of kinetic energy $\Delta E_{kin}/E_{kin}$ was observed to be independent of the ion kinetic energy [119] for Ar^{Q+} $(1 \leq Q \leq 9)$ with kinetic energies

below 2.2 keV.

A single Xe^{44+} projectile carries 51 keV of total potential energy, and 365 keV of kinetic energy (for parameters described in Ch. 3). Assuming that ions are delivered to the target at a rate 5×10^5 s^{-1}, this would add up to a total possible input power of $P_{max} = 32$ nW. The amount retained within the solid will be smaller. To resolve a 5 % decrease in the deposited fraction of ΔE_Q, the calorimeter needs resolution of around 200 pW (given constant kinetic energy). Additionally, a simultaneous measurement of ion current incident on the calorimeter (I) is required, to count the total number of ions impinging on the target. Recent developments in ultra-sensitive calorimetry make this a feasible measurement [120].

The primary advantage of calorimetry-based measurements is that they can detect the deposited fraction of potential energy that is converted to heat in the target that does not cause a permanent modification. Relying on energy measurements from Refs. [1, 27], we deduce that around 13 % of potential energy per ion impact goes into reversible heating. With a calorimetry measurement, this fraction would be directly measurable.

By using heavier ions with higher charge states than the Ar^{9+} beams in Ref. [119], ultra-sensitive calorimetry would allow for an investigation of the dependence of the fraction of deposited energy on projectile atomic structure. One could measure the fraction of potential energy retained in the target, as a function of the number of inner-shell vacancies. K, L and M shell vacancies, for example, may open up pathways for x-ray relaxation that decrease the fraction of potential energy deposited into the solid. It is plausible that "shell effects" will become apparent within the measurement of energy deposition.

If the calorimetry measurement were accompanied by simultaneous photon or secondary electron spectroscopy, a much more detailed view of how atomic

relaxation processes affect the deposited energy might be realized. In such a measurement, kinetic energy and charge state could be tuned to determine the optimum values where energy deposition is maximized.

6.2 Measurement of pre-equilibrium stopping with tunnel junctions

An understanding of pre-equilibrium stopping enhancements at the quantitative level remains a challenge in the field [121]. This is especially true for slow HCIs stopping in insulators.

Future kinetic energy dependent measurements with HCI modified tunnel junctions may provide an indirect measurement of these pre-equilibrium stopping magnitudes. The tunnel junction technique described in Ch. 3 is capable of detecting the damage within ultrathin barrier films, where film thickness s is smaller than the charge equilibration length, for HCIs. Modifications within the barrier are formed during pre-equilibrium stopping. Biersack' s model [35] predicts an exponential increase in kinetic energy transfer to the target nuclei with decreasing kinetic energy. If this picture is correct, energy deposition within s will increase exponentially as kinetic energy decreases, leading to deeper craters and higher σ_c values. Preliminary data shown at the end of Ch. 3 indicate that a 40 % reduction in kinetic energy leads to an order of magnitude increase in the average conductance through the impact sites (σ_c). Further data are needed to establish the quantitative dependence of σ_c on kinetic energy.

Appendices

Appendix A Plasma Chamber

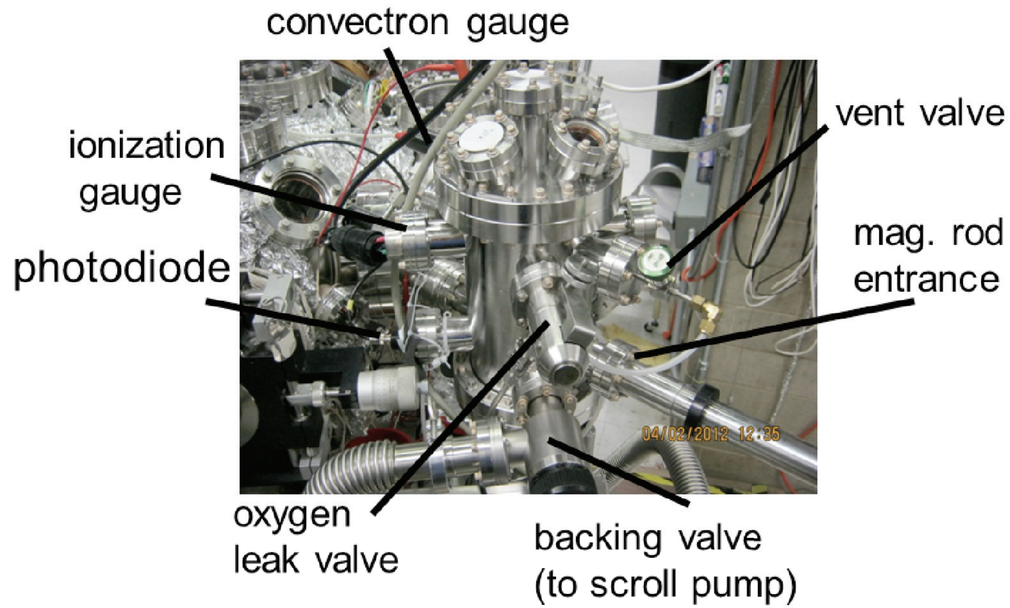

Figure 1: Sideview of the plasma chamber.

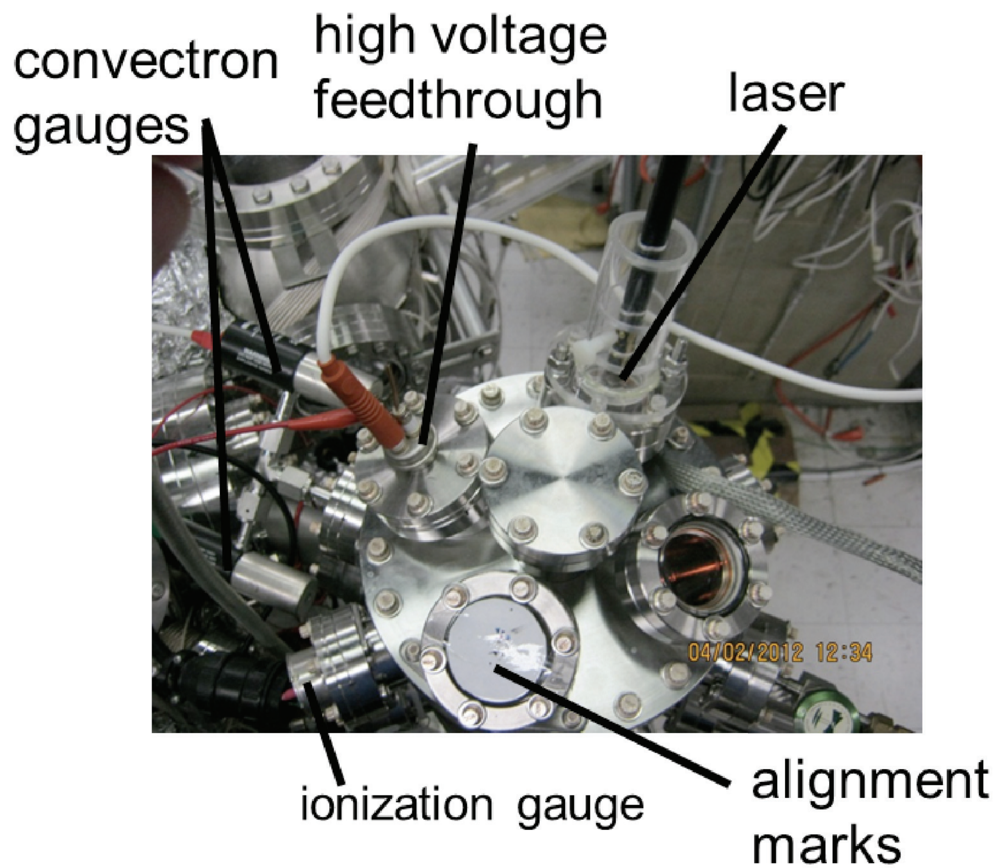

Figure 2: Top cluster flange of the plasma chamber. The laser beam spot illuminates one of the alignment marks, after being reflected from the sample in the chamber. Angular position of the sample can be adjusted with the magnetic transfer rod.

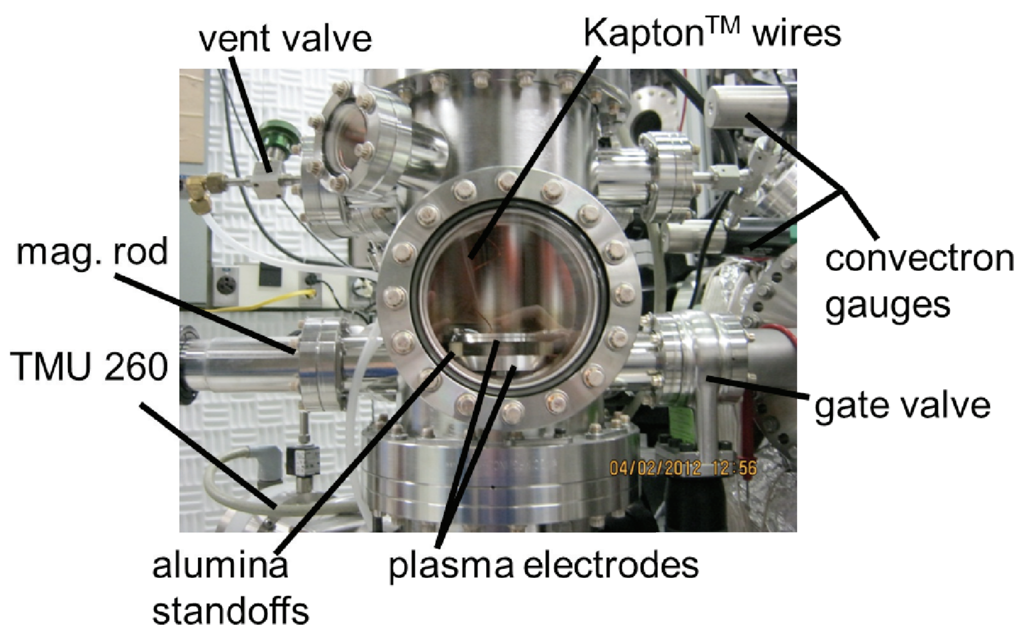

Figure 3: Plasma chamber through the 6″ viewport. The plasma electrodes are separated by alumina standoffs.

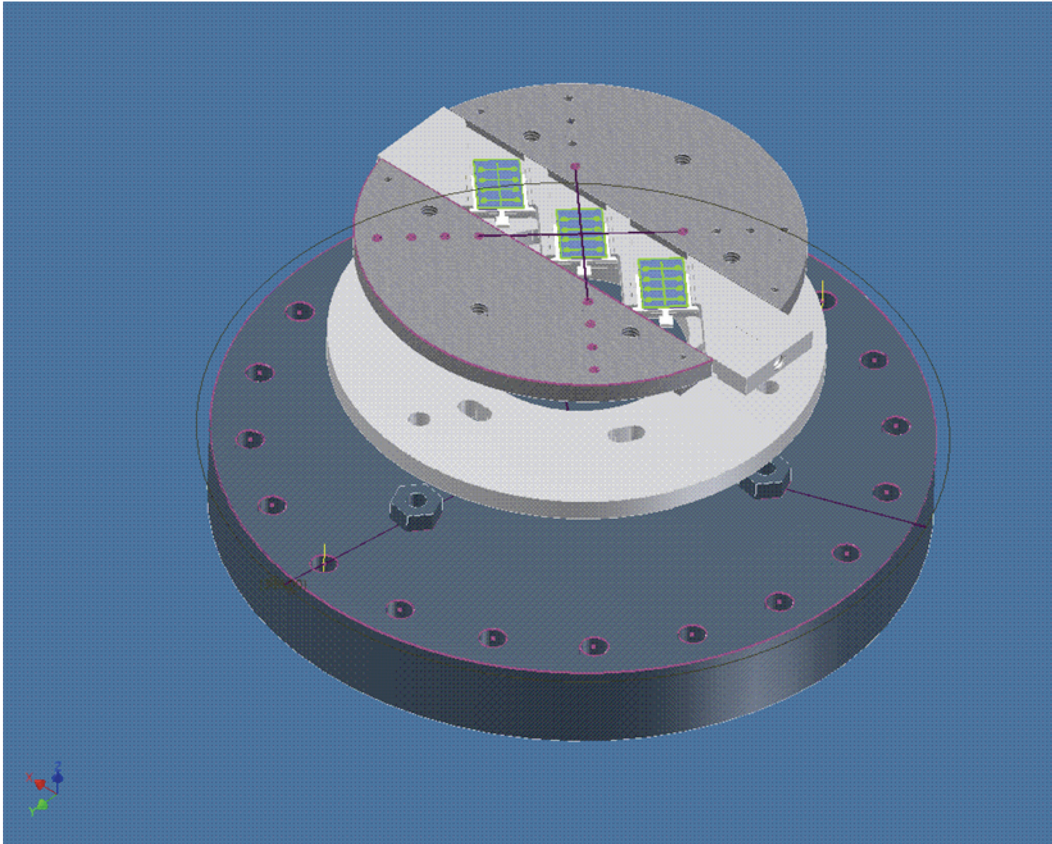

Figure 4: Schematic drawing of the bottom flange, bottom electrode and sled assembly. The top electrode and magnetic transfer rod are not shown. Each chip is 13 mm x 20 mm.

Appendix B Measuring light intensity of the discharge with the photodiode

The following procedure can be used to estimate the total light power incident on the photodiode, during the discharge. We read photovoltage from an unbiased photo diode (thorlabs SM1PD1B
`http://www.thorlabs.com/Thorcat/14000/14001-S01.PDF`) directly into an oscilloscope with input impedance 1 MΩ.

Total incident light power is $P = V_0/(R_\lambda \times R_l)$, where V_0 is the measured voltage on the oscilloscope, R_λ is the wavelength dependent responsivity [A/W] (Fig. 5) of the photodiode, and R_l is the input impedance of the scope.

To calculate an upper bound on the incident light power during the time the plasma is on, assume that all the light comes from λ = 550 nm peak. This choice leads to an upper bound for P because, this wavelength corresponds to a relatively low responsivity value R_λ = 0.3 A/W. This results in an upper bound on the power because, a large fraction of the incident light power comes from higher wavelengths that are more efficiently converted to the measured signal. The plasma has a violet color Fig. 6.

When the plasma is on, the photovoltage on the scope reads V_0 = 240 mV which is P = 800 nW of incident light power if all of the light were λ = 550 nm peak. When the plasma is off, V_0 = 84 mV.

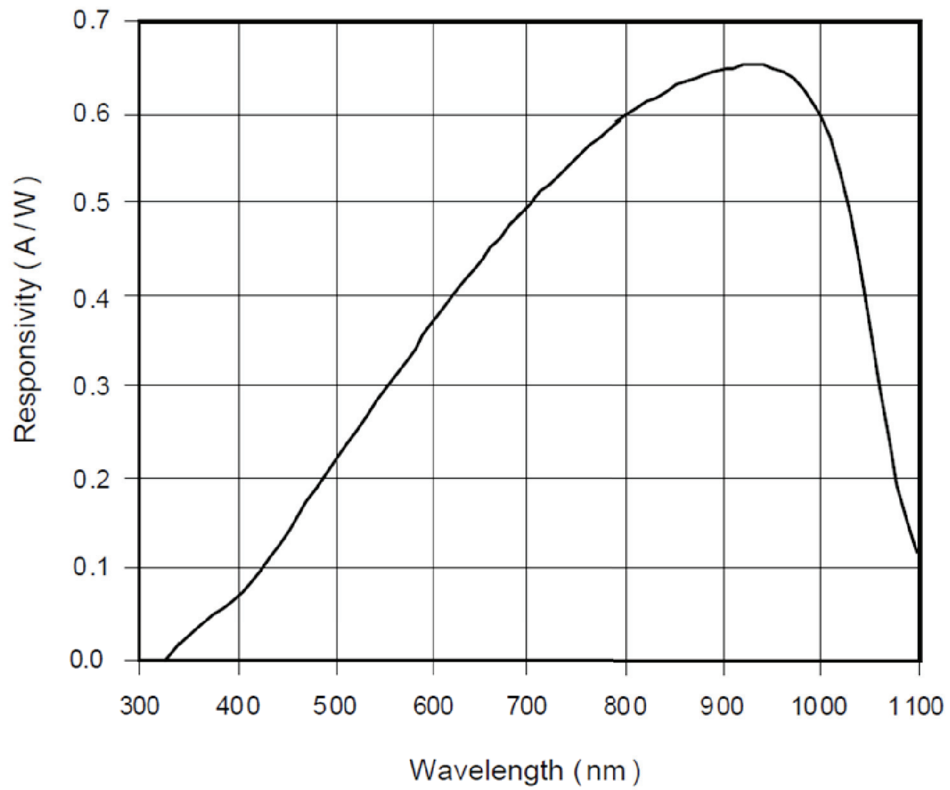

Figure 5: Specifications for wavelength dependent responsivity of the ThorLabs `SM1PD1B` photodiode (from the datasheet).

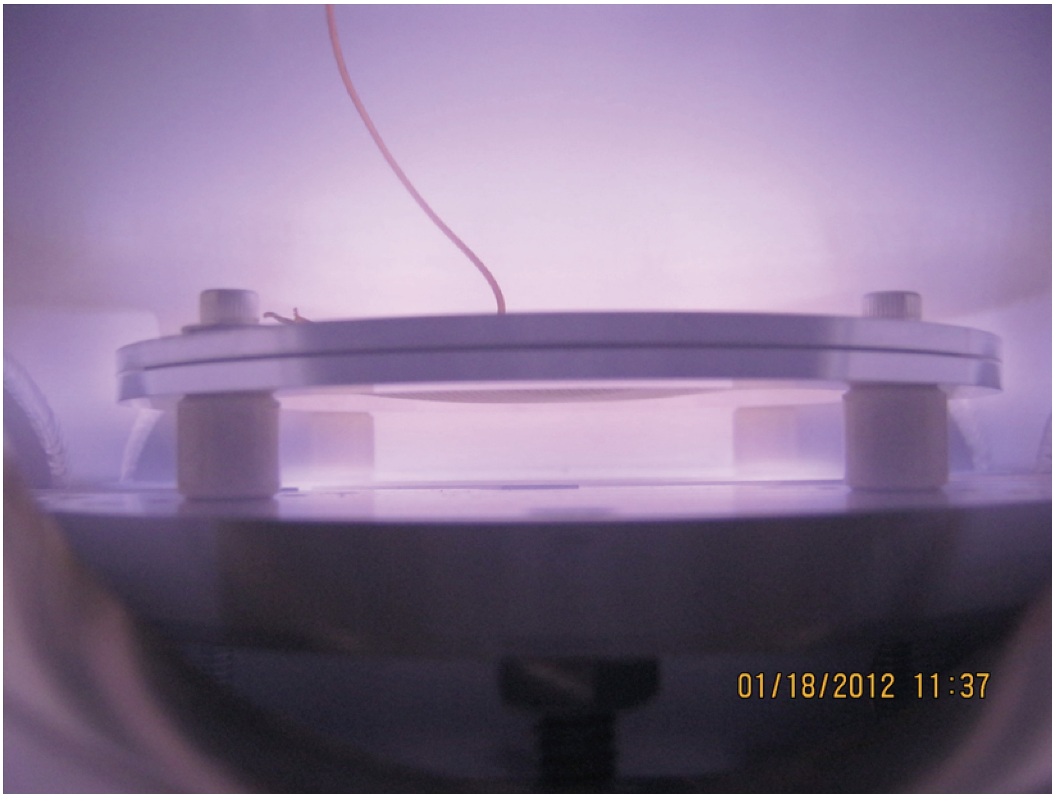

Figure 6: Photograph of an oxygen discharge at I_{set} = 40 mA, 120 mTorr, with negative bias on top electrode.

Appendix C Resistance of a tunnel junction during warm up (77 K to 300 K)

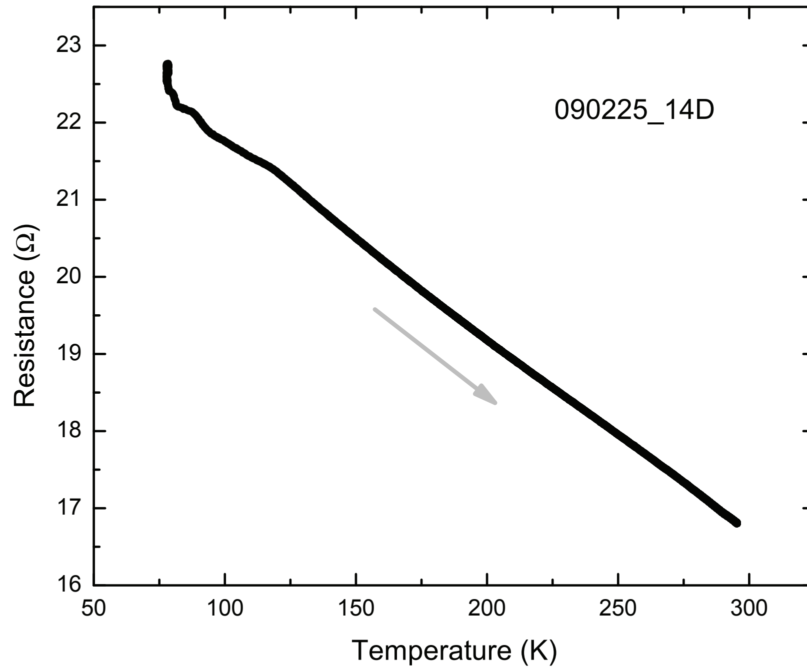

Figure 7: Resistance as a function of temperature for a tunnel juntion (sample 090225-14D)

Appendix D Fitting a micrograph line profile

Micrograph line profiles were fit with the following function,

$$f(z) = A_1 \mathrm{Erf}\left[\frac{1}{e_w(z - e_l)}\right] \times \mathrm{Erf}\left[-\frac{1}{e_w(z - e_r)}\right] + A_2 + mz. \tag{2}$$

The distance between the left and right edges of the wire (in pixels) shown in the line scane is $w = e_r - e_l$. For the micrograph shown in Fig. 8, the parameters of the fitted line are e_w = 8.76 , e_l = 60.09, e_r = 170.49, A_1 = 35.5, A_2 = 141.9, m = -6.2E-3. The slope of the step edges is captured in e_w. This slice came from a wire on a device grown with the G1 maskset.

Based on a systematic study using focused ion beam cuts, it was found that the width of the wire that carries electrical current is typically within a few percent of $e_r - e_l + 2e_w$.

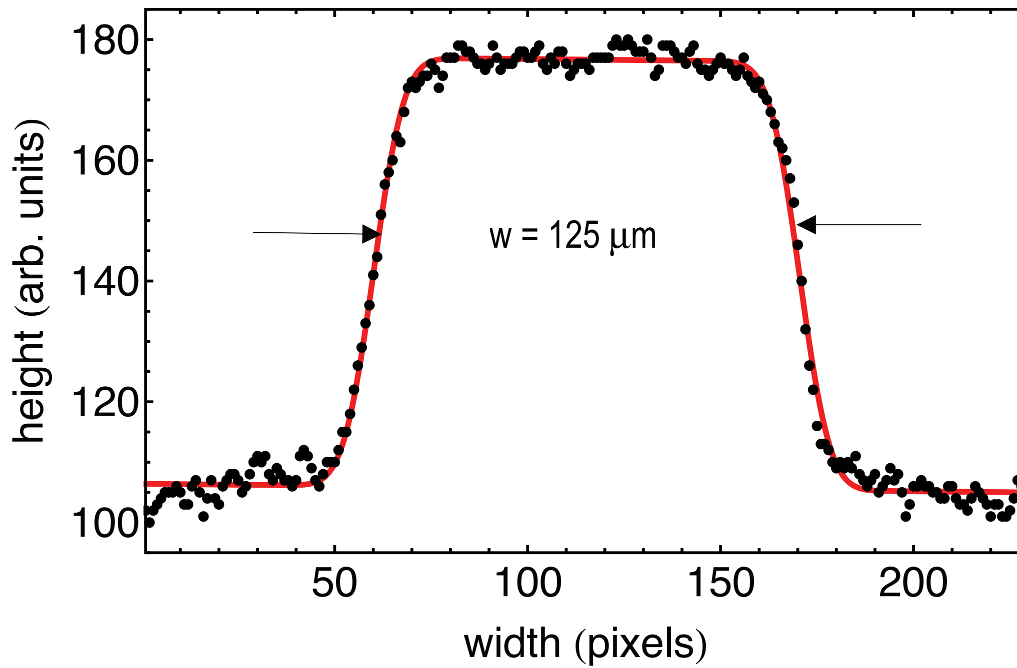

Figure 8: Micrograph line profile. The vertical axis is the arbitrary intensity of the microscope colorscale. The scale factor is 1.02 pixel μm^{-1}, making the width between the edges e_l and e_r arrows w = 125 μm.

Appendix E Data analysis

The following tables give an overview of the data analysis from three chips (`111223-3`, `111223-13` and `111223-14`). Ion beams were extracted from the EBIT at an acceleration voltage of approximately 5 kV, giving ions kinetic energy $5 \times Q$ keV. The data analysis is divided into three tables: 1) "negative resistance" correction (Table 1), 2) determining ion dose N (Table 2), and 3) calculation of the most probable values of σ_c on each chip (Table 3). The full data set for this particular EBIT run consisted of seven chips dosed with $Q = 36$ and $Q = 41$. A single value of $\bar{\sigma}_c$ was calculated for each charge state.

The data plotted in Fig. 3.6, were analyzed with a similar method to the one shown here. However, these chips were fabricated with the G1 mask set and only had four devices per chip. Only one device per chip was left unirradiated.

sample	R_b (Ω)	R_t (Ω)	$R_{b\square}$ ($\Omega/\square$)	$R_{t\square}$ ($\Omega/\square$)	H (μm)	W (μm)	A (μm^2)	ΔR_∞ (Ω)	ΔR_0 (Ω)	R_{4pt} (Ω)	R_{dev} (Ω)
3a	2043	133.5	20.43	1.34	25.34	32.64	826.93	2.93	-0.31	179.90	182.80
3b	2043	133.5	20.43	1.34	26.42	34.60	913.96	2.89	-0.32	0.06	1.49
3c	2043	133.5	20.43	1.34	25.92	35.16	911.35	2.81	-0.33	0.91	2.72
3d	2043	133.5	20.43	1.34	25.84	36.87	952.41	2.70	-0.32	5.45	7.72
3e	2043	133.5	20.43	1.34	26.37	38.04	1002.79	2.68	-0.32	0.58	2.22
3f	2043	133.5	20.43	1.34	26.53	38.12	1011.32	2.69	-0.32	2.29	4.30
3g	2043	133.5	20.43	1.34	26.40	37.64	993.38	2.71	-0.32	267.20	269.89
13a	1477	119	14.77	1.19	26.05	29.03	756.10	2.43	-0.31	388.00	390.42
13b	1477	119	14.77	1.19	26.11	29.03	757.84	2.43	-0.32	48.10	50.47
13c	1477	119	14.77	1.19	25.54	28.48	727.24	2.43	-0.33	29.00	31.33
13d	1477	119	14.77	1.19	26.05	27.49	715.85	2.54	-0.32	28.60	31.04
13e	1477	119	14.77	1.19	26.72	26.30	702.47	2.70	-0.32	92.60	95.26
13f	1477	119	14.77	1.19	26.56	25.30	671.84	2.77	-0.32	422.80	425.56
13g	1477	119	14.77	1.19	26.95	24.71	665.80	2.87	-0.32	210.40	213.25
13h	1477	119	14.77	1.19	26.93	24.71	665.18	2.86	-0.32	315.70	318.55
14a	1649	139.2	16.49	1.39	24.90	32.05	797.92	2.43	-0.31		
14b	1649	139.2	16.49	1.39	26.77	34.62	926.47	2.43	-0.32	295.40	297.81
14c	1649	139.2	16.49	1.39	27.33	35.04	957.47	2.44	-0.33	50.40	52.78
14d	1649	139.2	16.49	1.39	28.38	36.09	1024.23	2.46	-0.32	82.00	84.42
14e	1649	139.2	16.49	1.39	28.03	36.75	1030.10	2.40	-0.32	21.60	23.88
14f	1649	139.2	16.49	1.39					-0.32	347.30	350.28

Table 1: "Negative resistance" correction for 3, 13, 14. Unirradiated control devices are shaded.

Q (e)	sample	A_{spot} (mm^2)	ΔA_{spot} (mm^2)	A (μm^2)	ΔA (μm^2)	I_{FC} (pA)	ΔI_{FC} (pA)	t (s)	Δt (s)	N	ΔN	$\Delta N/N$
41	3a	0.42	0.02	826.93	186.91	2.8	0.1	0	0			
	3b	0.42	0.02	913.96	203.95	2.8	0.1	370	1	3.432E+05	8.638E+04	0.25
	3c	0.42	0.02	911.35	208.89	2.8	0.1	190	1	1.757E+05	4.518E+04	0.26
	3d	0.42	0.02	952.41	224.20	2.8	0.1	70	1	6.766E+04	1.779E+04	0.26
	3e	0.42	0.02	1002.79	234.94	2.8	0.1	250	1	2.544E+05	6.656E+04	0.26
	3f	0.42	0.02	1011.32	235.73	2.8	0.1	130	1	1.334E+05	3.478E+04	0.26
	3g	0.42	0.02	993.38	231.26	2.8	0.1	0	0			
36	13a	0.7961	0.02	756.10	79.26	3.3	0.1	0	0			
	13b	0.7961	0.02	757.84	79.27	3.3	0.1	130	1	7.080E+04	7.932E+03	0.11
	13c	0.7961	0.02	727.24	77.06	3.3	0.1	370	1	1.934E+05	2.186E+04	0.11
	13d	0.7961	0.02	715.85	73.21	3.3	0.1	490	1	2.521E+05	2.763E+04	0.11
	13e	0.7961	0.02	702.47	68.73	3.3	0.1	255	1	1.287E+05	1.359E+04	0.11
	13f	0.7961	0.02	671.84	65.00	3.3	0.1	0	0			
	13g	0.7961	0.02	665.80	62.86	3.3	0.1	0	0			
	13h	0.7961	0.02	665.18	62.86	3.3	0.1	0	0			
36	14a	0.7961	0.02	797.92	91.55	3.4	0.1	0	0			
	14b	0.7961	0.02	926.47	102.70	3.4	0.1	190	1	1.303E+05	1.532E+04	0.12
	14c	0.7961	0.02	957.47	104.60	3.4	0.1	310	1	2.198E+05	2.548E+04	0.12
	14d	0.7961	0.02	1024.23	109.33	3.4	0.1	130	1	9.859E+04	1.122E+04	0.11
	14e	0.7961	0.02	1030.10	112.27	3.4	0.1	550	1	4.195E+05	4.852E+04	0.12
	14f	0.7961	0.02			3.4	0.1	0	0			

Table 2: Error propagation for the dose N on chips 3, 13, 14. Unirradiated control devices are shaded. In addition to the uncertainty terms shown, an additional 10 % of N is added in quadrature with the other errors to account for a possible non-uniform areal density of ions within the spot.

Q (e)	sample	N	Δ N	R_{dev} (Ω)	ΔR_{dev} (Ω)	G_{dev} (S)	ΔG_{dev} (S)	R_0 (Ω)	ΔR_0 (Ω)	G_0 (S)	ΔG_0 (S)	σ_{ci} (S)	$\Delta\sigma_{ci}$ (S)	$\bar{\sigma_c}$ (per chip) (S)	$\Delta\bar{\sigma_c}$ (S)
41	3a	0.0000E+00	0.0000E+00	182.80	0.1	5.47E-03	2.99E-06	179.9	1	5.56E-03	3.09E-05			**1.9E-06**	**2.E-07**
	3b	3.4319E+05	8.6377E+04	1.49	0.1	6.72E-01	4.52E-02	226.1	1	4.42E-03	1.96E-05	1.95E-06	5.07E-07		
	3c	1.7573E+05	4.5182E+04	2.72	0.1	3.67E-01	1.35E-02	272.3	1	3.67E-03	1.35E-05	2.07E-06	5.37E-07		
	3d	6.7660E+04	1.7794E+04	7.72	0.1	1.29E-01	1.68E-03	318.5	1	3.14E-03	9.86E-06	1.87E-06	4.92E-07		
	3e	2.5442E+05	6.6565E+04	2.22	0.1	4.50E-01	2.03E-02	364.7	1	2.74E-03	7.52E-06	1.76E-06	4.67E-07		
	3f	1.3343E+05	3.4777E+04	4.30	0.1	2.32E-01	5.40E-03	401.9	1	2.49E-03	6.19E-06	1.72E-06	4.51E-07		
	3g	0.0000E+00	0.0000E+00	269.89	0.1	3.71E-03	1.37E-06	267.2	1	3.74E-03	1.40E-05				
36	13a	0.0000E+00	0.0000E+00	390.42	0.1	2.56E-03	6.56E-07	388.0	1	2.58E-03	6.64E-06			**8.9E-08**	**5.E-09**
	13b	7.0803E+04	7.9315E+03	50.47	0.1	1.98E-02	3.93E-05	395.0	1	2.53E-03	6.41E-06	2.44E-07	2.73E-08		
	13c	1.9338E+05	2.1865E+04	31.33	0.1	3.19E-02	1.02E-04	401.9	1	2.49E-03	6.19E-06	1.52E-07	1.72E-08		
	13d	2.5208E+05	2.7630E+04	31.04	0.1	3.22E-02	1.04E-04	408.9	1	2.45E-03	5.98E-06	1.18E-07	1.30E-08		
	13e	1.2873E+05	1.3586E+04	95.26	0.1	1.05E-02	1.10E-05	415.8	1	2.40E-03	5.78E-06	6.29E-08	6.64E-09		
	13f	0.0000E+00	0.0000E+00	425.56	0.1	2.35E-03	5.52E-07	422.8	1	2.37E-03	5.59E-06				
	13g	0.0000E+00	0.0000E+00	213.25	0.1	4.69E-03	2.20E-06	210.4	1	4.75E-03	2.26E-05				
	13h	0.0000E+00	0.0000E+00	318.55	0.1	3.14E-03	9.85E-07	315.7	1	3.17E-03	1.00E-05				
36	14a	0.0000E+00	0.0000E+00	0.00	0.1			297.3	1	3.36E-03	1.13E-05			**8.3E-08**	**6.E-09**
	14b	1.3034E+05	1.5318E+04	297.81	0.1	3.36E-03	1.13E-06	307.3	1	3.25E-03	1.06E-05	(filtered)	(filtered)		
	14c	2.1977E+05	2.5481E+04	52.78	0.1	1.89E-02	3.59E-05	317.3	1	3.15E-03	9.93E-06	7.19E-08	8.33E-09		
	14d	9.8590E+04	1.1219E+04	84.42	0.1	1.18E-02	1.40E-05	327.3	1	3.06E-03	9.33E-06	8.92E-08	1.01E-08		
	14e	4.1950E+05	4.8522E+04	23.88	0.1	4.19E-02	1.75E-04	337.3	1	2.96E-03	8.79E-06	9.28E-08	1.07E-08		
	14f	0.0000E+00	0.0000E+00	350.28	0.1	2.85E-03	8.15E-07	347.3	1	2.88E-03	8.29E-06				

Table 3: Error propagation for σ_c.

Appendix F Potential definitions and algorithms for calculating R_c'

The package "`num-funcs.m`" defines solutions to Poisson's equation, for a charge outside of two dissimilar dielectric media using Mathematica MathKernel. Here, we consider the solution in one dimension, in the coordinate z, normal to the surface. The problem is treated in cylindrical coordinates, so that z is the axial coordinate (normal to the surface). ρ is the radial coordinate, and is set to zero in the calculation. Details of the derivation of the potential, boundary conditions and the general integral form of the solution are provided in [102]. In the follwing code, these integrals are computed with Mathematica's NIntegrate function. Image potentials were derived as shown in Ref [103]. The potentials use atomic units. Throughout this calculation, the origin is set at the position of the ion. b is the distance between the ion and the metal surface. a is the distance between the ion and the vacuum-film interface, *i.e.*, $s = b - a$.

```
(* ::Package:: *)

Clear[a,b,b1,eps1,eps2,eps3,m,q,s];

(* Boundary conditions constrain coefficients A1, B1, C1, D1.*)

A1[a_,b_,eps1_,eps2_,eps3_]:=
(E^(-2 a m) (E^(2 a m) (eps1+eps2) (eps2-eps3)+
E^(2 b m) (eps1-eps2) (eps2+eps3)))/(E^(2 a m) (eps1-eps2)
(eps2-eps3)+E^(2 b m) (eps1+eps2) (eps2+eps3));
```

```
B1[a_,b_,eps1_,eps2_,eps3_]:=
(2 E^(2 b m) eps1 (eps2+eps3))/(E^(2 a m)(eps1-eps2)(eps2-eps3) +
E^(2 b m) (eps1+eps2) (eps2+eps3));

C1[a_,b_,eps1_,eps2_,eps3_]:=
(2 eps1 (eps2-eps3))/(E^(2 a m) (eps1-eps2) (eps2-eps3)+
E^(2 b m) (eps1+eps2) (eps2+eps3));

D1[a_,b_,eps1_,eps2_,eps3_]:=
(4 E^(2 b m) eps1 eps2)/(E^(2 a m) (eps1-eps2) (eps2-eps3)+
E^(2 b m) (eps1+eps2) (eps2+eps3));


(*electrostatic potential*)
v1[q_,a_,b_,eps1_,eps2_,eps3_]:=
(q/(eps1))*NIntegrate[(Exp[-m*Abs[z]]+
A1[a,b,eps1,eps2,eps3]*Exp[m*z]),
{m,0,\[Infinity]}]

v2[q_,a_,b_,eps1_,eps2_,eps3_]:=
(q/(eps1))*NIntegrate[(B1[a,b,eps1,eps2,eps3]*Exp[-m*z]+
C1[a,b,eps1,eps2,eps3]*Exp[m*z]),
{m,0,\[Infinity]}]

v3[q_,a_,b_,eps1_,eps2_,eps3_]:=
```

```
(q/(eps1))*Integrate[(D1[a,b,eps1,eps2,eps3]*Exp[-m*z]),
{m,0,\[Infinity]},Assumptions->z>0&&z>b];

v123[q_,a_,b_,eps1_,eps2_,eps3_]:=
-Piecewise[{{v1[q,a,b,eps1,eps2,eps3],0<z<a},
{v2[q,a,b,eps1,eps2,eps3],a<z<b},
{v3[q,a,b,eps1,eps2,eps3],z>b}}]

(* Reflection coefficients for the electron self-image term*)
k1=.;

k1[eps1_,eps2_]:=(eps2-eps1)/(eps2+eps1)

(*third region is a conductor*)
k2=-1;

sivac[a_,b_,eps1_,eps2_]:=
-(1/(2*eps1))*
Sum[(k1[eps1,eps2]*k2)^n*(-k1[eps1,eps2]/(2*z-(2*a)-(2*n*(b-a)))+
k2/(2*z-(2*b)-(2*n*(b-a)))),
{n,0,\[Infinity]}]

(*image potential outside the thin film.  this is the same as
 sivac, but it is pre-evaluated to make calculation faster *)

sivacfinal[adist_,bdist_,ep1_,ep2_]:=
```

```
-(1/(4 (adist-bdist) ep1 (ep1+ep2) (bdist-z)))
(bdist ep1
HurwitzLerchPhi[(ep1-ep2)/(ep1+ep2),1,(-adist+z)/(adist-bdist)]
-bdist ep2 HurwitzLerchPhi[(ep1-ep2)/(ep1+ep2),
1,(-adist+z)/(adist-bdist)]-
ep1 z HurwitzLerchPhi[(ep1-ep2)/(ep1+ep2),
1,(-adist+z)/(adist-bdist)]+
ep2 z HurwitzLerchPhi[(ep1-ep2)/(ep1+ep2),
1,(-adist+z)/(adist-bdist)]+
adist ep1 Hypergeometric2F1[1,
-(bdist/(adist-bdist))+z/(adist-bdist),adist/(adist-bdist)
-(2bdist)/(adist-bdist)+z/(adist-bdist),(ep1-ep2)/(ep1+ep2)]-
bdist ep1 Hypergeometric2F1[1,
-(bdist/(adist-bdist))+z/(adist-bdist),adist/(adist-bdist)-
(2 bdist)/(adist-bdist)+z/(adist-bdist),(ep1-ep2)/(ep1+ep2)]+
adist ep2 Hypergeometric2F1[1,
-(bdist/(adist-bdist))+z/(adist-bdist),adist/(adist-bdist)
-(2 bdist)/(adist-bdist)+z/(adist-bdist),(ep1-ep2)/(ep1+ep2)]
-bdist ep2 Hypergeometric2F1[1,-(bdist/(adist-bdist))+
z/(adist-bdist),adist/(adist-bdist)-(2
bdist)/(adist-bdist)+z/(adist-bdist),
(ep1-ep2)/(ep1+ep2)])


sifilm[b_,eps2_,Ecbm_]:=Ecbm-(1/(4*eps2*(-z+b)))
```

```
(* Potential energy in the vacuum and dielectric regions,
 including the self image term. *)

vacuum[Q_,a_,b_,eps1_,eps2_,eps3_]:=
-v1[Q,a,b,eps1,eps2,eps3]+sivacfinal[a,b,eps1,eps2]

film[Q_,a_,b_,eps1_,eps2_,eps3_,Ecbm_]:=
-v2[Q,a,b,eps1,eps2,eps3]+sifilm[b,eps2,Ecbm]
```

The potentials defined in "num-funcs.m" can be implemented in loops to find the critical distance as a function of various parameters. The following loop function finds the critical distance as a function of film thickness, for a series of charge states. In the loop, the ion steps incrementally toward the surface. At each step, we evaluate the heights of the potential maxima within the film and vacuum. If the potential in the vacuum drops below E_{vbm} then the first captured electron comes from the insulator. If the potential maxima in the film and in the vacuum drop below E_F, then the electron comes from the metal. The variable "flag" indicates whether the electron comes from the insulator or metal.

```
(* use the numerically integrated potentials*)
<<num_funcs.m

(* define the metal work function, film permittivity,
conduction band minimum and band gap in atomic units *)
(* 1 E_H = 27.211 eV*)
```

```
W = -(5.0/27.211);
ep = 6;
Eg = (3/27.211);
Ecbm = -(4/27.211)


(* Film thickness limits and step size *)
sinit = 1
sfin = 160
ds = 1

(* initialize the ion position arrays*)
rclist = {};
rlist = {};


Clear[s];
Clear[flag];
Clear[b1];

(* sets the spacing between successive energy points
within a single potential plot, V(z)*)

dz = 0.1;
```

```
(* initial and final charge states,
and the charge steps * )

qinit = 26;
qfin = 44;
dq = 1;


Do[


(* a value greater than the critical distance,
to start searching.  *)

   bguess = Sqrt[2*q1]/Abs[W]+3;


Do[


(* starting from bguess, step the ion toward the
surface by 0.1 a.u increments.  For each step,
add the ion's distance from the metal to rlist.
R'c will be the last value in rlist, after the
While loop returns False. *)
```

```
b1 = bguess;

   While[(Max[Table[vacuum[q1, b1 - s, b1, 1, ep, 10^6],
{z, 1, (b1 - s) - 0.1, dz}]] > W ||
Max[Table[film[q1, b1 - s, b1, 1, ep, 10^6, Ecbm],
{z, (b1 - s), b1 - 0.1, dz}]] > W) &&
Max[Table[vacuum[q1, b1 - s, b1, 1, ep, 10^6],
{z, 1, (b1 - s) - 0.1, dz}]] >
(Table[film[q1, b1 - s, b1, 1, ep,10^6, Ecbm],
{z, b1 - s, b1 - s,dz}][[1]] - Eg),


       AppendTo[rlist, b1];

   (* move the ion 0.1 a.u. forward *)
   b1 = b1 - 0.1]


(* Print whether the first captured electron comes
from the metal, or insulator*)

   If[(Table[film[q1, b1 - s, b1, 1, ep, 10^6, Ecbm],
{z, b1 - s, b1 - s,0.1}][[1]] - Eg) >
Max[Table[vacuum[q1, b1 - s,b1, 1, ep, 10^6],
 {z, 1, (b1 - s) - 0.1, 1}]],
```

```
flag="insulator wins",flag="metal wins"];



(* Print the film thickness, R'c,
whether the metal/insulator won, and the charge state.*)

Print[ToString[s]<>"\t"<> ToString[Last[rlist]]
<>"\t"<>flag<>"\t"<>ToString[q1]];

(* list of critical distances *)
AppendTo[rclist, {s,Last[rlist],flag,q1,Eg,ep}];



(* clear the variables after finding R'c *)
   Clear[flag];
   Clear[condition];
   Clear[b1];
   Clear[bguess];
   bguess = Last[rlist] + 3;
   rlist = {};,

 {s, sinit, sfin, ds}
 ]
```

```
(* Write results to a text file.*)

Export["q" <> ToString[q1]<>"_"<>"Rc_s"<>ToString[sinit]<>
"-"<>ToString[sfin]<>"_"<>"ep"<>ToString[ep]<>"_"<>
"Eg"<>ToString[NumberForm[Eg,2]]<>"W"<>ToString[NumberForm[W,2]]<>
"_"<>"phi"<>ToString[NumberForm[Ecbm-W,2]]<>".txt",rclist,"Table"]

Clear[rclist];
rclist={};,

(* do for all charge states *)
{q1, qinit, qfin, dq}
]
```

We can also plot the exact, analytically calculated potentials using Mathematica's `Integrate[]` function. The drawback when using these potentials to find the critical distance is that exact integration increases calculation time.

```
(*  Analytical potential calculation
(using Integrate[] instead of NIntegrate[]*)

Clear[a,b,b1,eps1,eps2,eps3,m,q,s];

A1[a_,b_,eps1_,eps2_,eps3_]:=
(E^(-2 a m) (E^(2 a m) (eps1+eps2) (eps2-eps3)+
E^(2 b m) (eps1-eps2) (eps2+eps3)))/
```

```
(E^(2 a m) (eps1-eps2) (eps2-eps3)+E^(2 b m) (eps1+eps2) (eps2+eps3));

B1[a_,b_,eps1_,eps2_,eps3_]:=
(2 E^(2 b m) eps1 (eps2+eps3))/
(E^(2 a m) (eps1-eps2) (eps2-eps3)+
E^(2 b m) (eps1+eps2) (eps2+eps3));

C1[a_,b_,eps1_,eps2_,eps3_]:=
(2 eps1 (eps2-eps3))/
(E^(2 a m) (eps1-eps2) (eps2-eps3)+E^(2 b m) (eps1+eps2) (eps2+eps3));

D1[a_,b_,eps1_,eps2_,eps3_]:=
(4 E^(2 b m) eps1 eps2)/(E^(2 a m) (eps1-eps2) (eps2-eps3)+
E^(2 b m) (eps1+eps2) (eps2+eps3));


(*electrostatic potential*)
v1[q_,a_,b_,eps1_,eps2_,eps3_]:=
(q/(eps1))*Integrate[(Exp[-m*Abs[z]]+A1[a,b,eps1,eps2,eps3]*Exp[m*z]),
{m,0,\[Infinity]},Assumptions->z>0&&z<a]

v2[q_,a_,b_,eps1_,eps2_,eps3_]:=
(q/(eps1))*Integrate[(B1[a,b,eps1,eps2,eps3]*Exp[-m*z]+
C1[a,b,eps1,eps2,eps3]*Exp[m*z]),
{m,0,\[Infinity]},Assumptions->z>0&&z<b&&z>a]
```

```
v3[q_,a_,b_,eps1_,eps2_,eps3_]:=
(q/(eps1))*Integrate[(D1[a,b,eps1,eps2,eps3]*Exp[-m*z]),
{m,0,\[Infinity]},Assumptions->z>0&&z>b];

v123[q_,a_,b_,eps1_,eps2_,eps3_]:=
-Piecewise[{{v1[q,a,b,eps1,eps2,eps3],0<z<a},
{v2[q,a,b,eps1,eps2,eps3],a<z<b},
{v3[q,a,b,eps1,eps2,eps3],z>b}}]



(*self-image potential*)
(* defin the reflection coefficients k1, k2*)
k1=.;
k1[eps1_,eps2_]:=(eps2-eps1)/(eps2+eps1)
(*k2=(eps2-eps3)/(eps2+eps3)*)
(*third region is a conductor*)
k2=-1;

E1[a_,b_,eps1_,eps2_,Ecbm_]:=
Piecewise[{{-(1/(2*eps1))*
Sum[(k1[eps1,eps2]*k2)^n*(-k1[eps1,eps2]/(2*z-(2*a)-(2*n*(b-a)))+
k2/(2*z-(2*b)-(2*n*(b-a)))),{n,0,\[Infinity]}],z<a},
{Ecbm-(1/(4*eps2*(-z+b))),a<z<b}}]

V[q_,a_,b_,eps1_,eps2_,eps3_,Ecbm_]:=
E1[a,b,eps1,eps2,Ecbm]+
```

```
v123[q,a,b,eps1,eps2,eps3]
```

The following script exports potentials for plotting (in a text file and as portable network graphics) using the analytically calculated potentials. This script is used to view the potential for any set of parameters. To change the coordinate system to the conventional $z = 0$ at the surface and ion at $+R$, make the transformation $z' \to (-1 \times z + \text{Max}(z))$ to the first column of the `.txt` file when plotting. The energies stay the same.

```
(*Needs[Context[],Directory[]<>"/pot_funcs.m"];*)
<<pot_funcs.m


s=10;
q1=10;
W=-(5.3/27.211);
ep = 8;
Eg = (9.5/27.211);
Ecb = -(4/27.211)


b1=.;


Do[
   Clear[p1,p2];
    p1=V[q1,(b1-s),b1,1,ep,10^6,Ecb];
p2=Piecewise[{{p1-Eg,(b1-s)<z<b1}}];


pl1=
```

```
Plot[{p1,p2,W},{z,0,b1},
PlotRange->{-1,0},Frame->True, FrameStyle -> AbsoluteThickness[1.5],
PlotRangePadding-> None, ImageSize -> {800,600},
PlotStyle -> {Directive[Blue, Thick],Directive[Blue,
Thick],Directive[Red,Dashed]},
LabelStyle -> {Black, 20,FontFamily -> "Helvetica"}];

Export[Directory[]<>"/"<>"q"<>ToString[q1]<>"_"<>"s"<>ToString[s]<>
"_"<>ToString[ep]<>"_"<>"b"<>ToString[b1]<>".png",pl1]

Export[Directory[]<>"/"<>"q"<>ToString[q1]<>"_"<>"s"<>ToString[s]<>
"_"<>ToString[ep]<>"_"<>"b"<>ToString[b1]<>".txt",
Table[{z,p1//N,p2//N},{z,1,b1,0.1}],"Table"]

Print[b1];
,{b1,s,100,10} ];
```

Appendix G Atomic units

Quantity	Fundamental constants	SI units	
atomic unit of action	$\hbar$	1.054 571 726 e-34	J s
atomic unit of charge	e	1.602 176 565 e-19	C
atomic unit of charge density	e/a_0^3	1.081 202 338 e12	C m^{-3}
atomic unit of current	$eE_h/\hbar$	6.623 617 95 e-3	A
atomic unit of electric dipole moment	ea_0	8.478 353 26 e-30	C m
atomic unit of electric field	E_h/ea_0	5.142 206 52 e11	V m^{-1}
atomic unit of electric field gradient	E_h/ea_0^2	9.717 362 00 e21	V m^{-2}
atomic unit of electric polarizability	$e^2a_0^2/E_h$	1.648 777 2754 e-41	C^2 m^2 J^{-1}
atomic unit of electric potential	E_h/e	27.211 385 05	V
atomic unit of electric quadrupole moment	ea_0^2	4.486 551 331 e-40	C m^2
atomic unit of energy	E_h	4.359 744 34 e-18	J
atomic unit of force	E_h/a_0	8.238 722 78 e-8	N
atomic unit of length	a_0	0.529 177 210 92 e-10	m
atomic unit of mass	m_e	9.109 382 91 e-31	kg
atomic unit of momentum	$\hbar/a_0$	1.992 851 740 e-24	kg m s^{-1}
atomic unit of permittivity	e^2/a_0E_h	1.112 650 056... e-10	F m^{-1}
atomic unit of time	$\hbar/E_h$	2.418 884 326 502 e-17	s
atomic unit of velocity	$a_0E_h/\hbar$	2.187 691 263 79 e6	m s^{-1}

Table 4: Relationship between selected atomic units, fundamental constants and SI units from Ref. [5]

References

[1] R. E. Lake, J. M. Pomeroy, H. Grube, and C. E. Sosolik, "Charge state dependent energy deposition by ion impact," Phys. Rev. Lett. **107**, 063202 (2011)

[2] H. Khemliche, T. Schlathölter, R. Hoekstra, R. Morgenstern, and S. Schippers, "Hollow atom dynamics on LiF covered Au(111): Role of the surface electronic structure," Phys. Rev. Lett. **81**, 1219–1222 (1998)

[3] H. Khemliche, T. Schlathölter, R. Hoekstra, and R. Morgenstern, "L-shell filling of N^{6+} and O^{7+} ions from a clean and LiF-covered Au(111) surface," Phys. Rev. A **60**, 3800–3808 (1999)

[4] E. Bodewits, R. Hoekstra, G. Kowarik, K. Dobes, and F. Aumayr, "Highly-charged-ion-induced electron emission from c_{60} thin films," Phys. Rev. A **84**, 042901 (2011)

[5] 2010 CODATA recommended values, `http://physics.nist.gov/cuu/Constants/index.html`

[6] C. K. Chow, "Square-mean-root approximation for evaluating asymmetric tunneling characteristics," J. Appl. Phys. **36**, 559–563 (1965)

[7] A. I Pikin, C. A. Morgan, E. W. Bell, L. P. Ratliff, D. A. Church, and J. D. Gillaspy, "A beam line for highly charged ions," Rev. Sci. Instrum. **67**, 2528–2533 (1996)

[8] T. Schenkel, A.V. Hamza, A.V. Barnes, and D.H. Schneider, "Interaction of slow, very highly charged ions with surfaces," Prog. Surf. Sci. **61**, 23 – 84 (1999)

[9] A. M. Lahee, J. R. Manson, J. P. Toennies, and Ch. Wöll, "Observation of interference oscillations in helium scattering from single surface defects," Phys. Rev. Lett. **57**, 471–474 (1986)

[10] M. Toulemonde, C. Trautmann, E. Balanzat, K. Hjort, and A. Weidinger, "Track formation and fabrication of nanostructures with mev-ion beams," Nucl. Instrum. Methods Phys. Res., Sect. B **216**, 1 – 8 (2004)

[11] M. L. E. Oliphant and P. B. Moon, "The liberation of electrons from metal surfaces by positive ions. part II. theoretical," Proc. R. Soc. Lond. A **127**, 388–406 (1930)

[12] M. L. E. Oliphant, "The liberation of electrons from metal surfaces by positive ions. part I. experimental," Proc. R. Soc. Lond. A **127**, 373–387 (1930)

[13] W. Heiland, "Interaction of charged particles with solids and surfaces," (Plenum Press, New York, 1991) Chap. Interaction of low-energy ions, atoms and molecules with surfaces, p. 253

[14] Homer D. Hagstrum, "Theory of auger ejection of electrons from metals by ions," Phys. Rev. **96**, 336–365 (1954)

[15] J. Los and J. J. C. Geerlings, "Charge exchange in atom-surface collisions," Phys. Rep. **190**, 133 – 190 (1990)

[16] J. Burgdörfer, "Review of fundemental processes and applications of atoms and ions," (World Scientific, 1993) Chap. 11: Atomic Collisions with Surfaces, p. 517

[17] H. Winter, "Collisions of atoms and ions with surfaces under grazing incidence," Phys. Rep. **367**, 387 – 582 (2002)

[18] A. Arnau, F. Aumayr, P. M. Echenique, M. Grether, W. Heiland, J. Limburg, R. Morgenstern, P. Roncin, S. Schippers, R. Schuch, N. Stolterfoht, P. Varga, T. J. M. Zouros, and H. P. Winter, "Interaction of slow multicharged ions with solid surfaces," Surf. Sci. Rep. **27**, 113 – 239 (1997)

[19] R. M. Papaléo, M. R. Silva, R. Leal, P. L. Grande, M. Roth, B. Schattat, and G. Schiwietz, "Direct evidence for projectile charge-state dependent crater formation due to fast ions," Phys. Rev. Lett. **101**, 167601 (2008)

[20] E. Akcoltekin, T. Peters, R. Meyer, A. Duvenbeck, M. Klusmann, I. Monnet, H. Lebius, and M. Schleberger, "Creation of multiple nanodots by single ions," Nat. Nano. **2**, 290–294 (2007)

[21] D H G Schneider and M A Briere, "Investigations of the interactions of highest charge state ions with surfaces," Phys. Scr. **53**, 228 (1996)

[22] H. P. Winter and F. Aumayr, "Hollow atoms," J. Phys. B: At. Mol. Opt. Phys. **32**, R39 (1999)

[23] J. Burgdörfer, P. Lerner, and F. W. Meyer, "Above-surface neutralization of highly charged ions: The classical over-the-barrier model," Phys. Rev. A **44**, 5674 (1991)

[24] J. P. Briand, L. de Billy, P. Charles, S. Essabaa, P. Briand, R. Geller, J. P. Desclaux, S. Bliman, and C. Ristori, "Production of hollow atoms by the excitation of highly charged ions in interaction with a metallic surface," Phys. Rev. Lett. **65**, 159–162 (1990)

[25] H. Kurz, F. Aumayr, HP. Winter, D. Schneider, M. A. Briere, and J. W. McDonald, "Electron emission and image-charge acceleration for the impact of very highly charged ions on clean gold," Phys. Rev. A **49**, 4693 (1994)

[26] S. Facsko, R. Heller, A. S. El-Said, W. Meissl, and F. Aumayr, "Surface nanostructures by single highly charged ions," J. Phys. Condens. Matter **21**, 224012 (2009)

[27] T. Schenkel, A. V. Barnes, T. R. Niedermayr, M. Hattass, M. W. Newman, G. A. Machicoane, J. W. McDonald, A. V. Hamza, and D. H. Schneider, "Deposition of potential energy in solids by slow, highly charged ions," Phys. Rev. Lett. **83**, 4273–4276 (1999)

[28] A. V. Krasheninnikov and K. Nordlund, "Ion and electron irradiation-induced effects in nanostructured materials," J. Appl. Phys. **107**, 071301 (2010)

[29] J. F. Ziegler, J. P. Biersack, and U. Littmark, *The stopping and ranges of ions in matter* (Pergamon, New York, 1985)

[30] E. Chason, S. T. Picraux, J. M. Poate, J. O. Borland, M. I. Current, T. Diaz de la Rubia, D. J. Eaglesham, O. W. Holland, M. E. Law, C. W. Magee, J. W. Mayer, J. Melngailis, and A. F. Tasch, "Ion beams in silicon processing and characterization," J. Appl. Phys. **81**, 6513–6561 (1997)

[31] C. C. Harrell, Z. S. Siwy, and C. R. Martin, "Conical nanopore membranes: Controlling the nanopore shape," Small **2**, 194–198 (2006)

[32] F. Aumayr and H. P. Winter, "Potential sputtering," Phil. Trans. R. Soc. Lond. A **362**, 77 (2004)

[33] J. M. Pomeroy, H. Grube, A. C. Perrella, and J. D. Gillaspy, "Selectable resistance-area product by dilute highly charged ion irradiation," Appl. Phys. Lett. **91**, 073506 (2007)

[34] Z. Insepov, J.P. Allain, A. Hassanein, and M. Terasawa, "Surface erosion by highly-charged ions," Nucl. Instrum. Methods Phys. Res., Sect. B **242**, 498 – 502 (2006)

[35] J. P. Biersack, "The effect of high charge states on the stopping and ranges of ions in solids," Nucl. Instrum. Methods Phys. Res., Sect. B **80-81**, 12 – 15 (1993)

[36] T. Schenkel, M. A. Briere, A. V. Barnes, A. V. Hamza, K. Bethge, H. Schmidt-Böcking, and D. H. Schneider, "Charge state dependent energy loss of slow heavy ions in solids," Phys. Rev. Lett. **79**, 2030–2033 (1997)

[37] F. Aumayr, S. Facsko, A. S. El-Said, C. Trautmann, and M. Schleberger, "Single ion induced surface nanostructures: a comparison between slow highly charged and swift heavy ions," J. Phys.: Condens. Matter **23**, 393001 (2011)

[38] Hugh D. Young, *Statistical treatment of experimental data* (McGraw-Hill, New York, 1962)

[39] J. M. Pomeroy, A. C. Perrella, H. Grube, and J. D. Gillaspy, "Gold nanostructures created by highly charged ions," Phys. Rev. B **75**, 241409 (2007)

[40] A. S. El-Said, R. Heller, W. Meissl, R. Ritter, S. Facsko, C. Lemell, B. Solleder, I. C. Gebeshuber, G. Betz, M. Toulemonde, W. Möller, J. Burgdörfer, and F. Aumayr, "Creation of nanohillocks on CaF_2 surfaces by single slow highly charged ions," Phys. Rev. Lett. **100**, 237601 (Jun 2008)

[41] R. Heller, S. Facsko, R. A. Wilhelm, and W. Moller, "Defect mediated desorption of the kbr(001) surface induced by single highly charged ion impact," Phys. Rev. Lett. **101**, 096102 (2008)

[42] Michael J. Allen, Nicholas V. Hud, Mehdi Balooch, Robert J. Tench, Wigbert J. Siekhaus, and Rod Balhorn, "Tip-radius-induced artifacts in AFM images of protamine-complexed DNA fibers," Ultramicroscopy **42 âĂŞ- 44**, 1095 – 1100 (1992)

[43] M. F. Tabet and F. K. Urban III, "Deconvolution of tip affected atomic force microscope images and comparison to rutherford backscattering spectrometry," J. Vac. Sci. Technol. B **15**, 800–804 (1997)

[44] E. L. Wolf, *Principles of electron tunneling spectroscopy* (Clarendon Press, New York, 1985)

[45] M. Hattass, T. Schenkel, A. V. Hamza, A. V. Barnes, M. W. Newman, J. W. McDonald, T. R. Niedermayr, G. A. Machicoane, and D. H. Schneider, "Charge equilibration time of slow, highly charged ions in solids," Phys. Rev. Lett. **82**, 4795–4798 (1999)

[46] J. M. Pomeroy, H. Grube, P. L. Sun, and R. E. Lake, "Magnetic tunnel junctions fabricated using ion neutralization energy as a tool," AIP Conference Proceedings **1336**, 111–114 (2011)

[47] J. M. Pomeroy and H. Grube, Nucl. Instrum. Methods Phys. Res., Sect. B **267**, 642 (2009)

[48] J.M. Pomeroy, R.E. Lake, and C.E. Sosolik, "Highly charged ion interactions with thin insulating films," Nucl. Instrum. Methods Phys. Res., Sect. B **269**, 1238 – 1242 (2011)

[49] J. M. Pomeroy, H. Grube, and A. C. Perrella, "Spatial and electronic characterization of nano-features created by highly charged ions," Radiat. Eff. Def. Solids **162**, 473–481 (2007)

[50] J. H. Moore, C. C. Davis, and M. A. Coplan, *Building scientific apparatus : a practical guide to design and construction* (Addison-Wesley, Advanced Book Program/World Science Division, London; Reading, Mass., 1983)

[51] Thermionics Inc., Hayward, CA, *3 kV Linear e-Gun: Evaporation Source Manual, RC-Series* (2003), 12-9-03, `http://www.thermionics.com`

[52] E. B. Graper, "Evaporation characteristics of materials from an electron beam gun," J. Vac. Sci. Technol. A **8**, 333–337 (1971)

[53] E. B. Graper, "Evaporation characteristics of materials from an electron beam gun ii," J. Vac. Sci. Technol. A **5**, 2718–2723 (1987)

[54] Inficon, 2 Technology Place, East Syracuse, NY, *XTM/2 Operating manual* (2001), `http://www.inficon.com`

[55] M. A. Lieberman and Allan J. Lichtenberg, *Principles of plasma discharges and materials processing* (Wiley, New York, 1994)

[56] A. E. T. Kuiper, M. F. Gillies, V. Kottler, G. W. 't Hooft, J. G. M. van Berkum, C. van der Marel, Y. Tamminga, and J. H. M. Snijders, "Plasma oxidation of thin aluminum layers for magnetic spin-tunnel junctions," J. Appl. Phys. **89**, 1965–1972 (2001)

[57] J. M. Pomeroy and H. Grube, J. Appl. Phys. **105**, 094503 (2009)

[58] R. J. Pedersen and Jr. F. L. Vernon, "Effect of film resistance on low impedance tunneling measurements," Appl. Phys. Lett. **10**, 29–31 (1967)

[59] J. M. Rowell, "Tunneling phenomena in solids," (Plenum, New York, 1963)

[60] W. F. Brinkman, R. C. Dynes, and J. M. Rowell, "Tunneling conductance of asymmetrical barriers," J. Appl. Phys. **41**, 1915–1921 (1970)

[61] M. Madec, J.-B. Kammerer, and L. Hebrard, "Compact modeling of a magnetic tunnel junction – part II: Tunneling current model," IEEE Trans. Electron Devices, **57**, 1416 – 1424 (2010)

[62] E. Merzbacher, *Quantum mechanics* (Wiley, New York, 1998)

[63] J. G. Simmons, "Generalized formula for the electric tunnel effect between similar electrodes separated by a thin insulating film," J. Appl. Phys. **34**, 1793–1803 (1963)

[64] A. C. Perrella, *Ballistic electron transport in aluminum oxide*, Ph.D. thesis, Cornell University (2004)

[65] G. Gutiérrez and B. Johansson, "Molecular dynamics study of structural properties of amorphous Al_2O_3," Phys. Rev. B **65**, 104202 (2002)

[66] S. P. Adiga, P. Zapol, and L. A. Curtiss, "Atomistic simulations of amorphous alumina surfaces," Phys. Rev. B **74**, 064204 (2006)

[67] D. G. Walmsley, R. B. Floyd, and W. E. Timms, "Conductance of clean and doped tunnel junctions," Solid State Commun. **22**, 497 – 499 (1977)

[68] R. B. Floyd and D. G. Walmsley, "Tunnelling conductance of clean and doped Al-I-Pb junctions," J. Phys. C: Solid State Phys. **11**, 4601 (1978)

[69] R. E. Lake, J. M. Pomeroy, and C. E. Sosolik, "Energy dissipation of highly charged ions on al oxide films," J. Phys.: Condens. Matter **22**, 084008 (2010)

[70] L. P. Ratliff, E. W. Bell, D. C. Parks, A. I. Pikin, and J. D. Gillaspy, "Continuous highly charged ion beams from the national institute of standards and technology electron-beam ion trap," Rev. Sci. Instrum. **68**, 1998–2002 (1997)

[71] R. E. Lake, J. M. Pomeroy, and C. E. Sosolik, "Critical capture distances for highly charged ions above dielectric covered metal surfaces," Nucl. Instrum. Methods Phys. Res., Sect. B **269**, 1199 – 1202 (2011)

[72] P. Thevenard, G. Guiraud, C. H. S. Dupuy, and B. Delaunay, "Assumption of f-centre creation in lif bombarded with high-energy particles," Radiat. Eff. **32**, 83–90 (1977)

[73] S. Ciraci and E. Tekman, "Theory of transition from the tunneling regime to point contact in scanning tunneling microscopy," Phys. Rev. B **40**, 11969–11972 (Dec 1989)

[74] H. Srikanth and A. K. Raychaudhuri, "Transition from metallic to tunneling-type conductance in metal-metal and normal-metal–superconductor point contacts," Phys. Rev. B **46**, 14713–14721 (1992)

[75] S. Datta, *Electronic transport in mesoscopic systems* (Cambridge University Press, Cambridge; New York, 1995)

[76] M. Tonna, H. Watanabe, S. Takahashi, N. Nakamura, N. Yoshiyasu, M. Sakurai, T. Terui, S. Mashiko, C. Yamada, and S. Ohtani, "Nano-crater formation on a Si(111)-(7 x 7) surface by slow highly charged ion-impact," Surf. Sci. **601**, 723 – 727 (2007)

[77] M. Tona, Y. Fujita, C. Yamada, and S. Ohtani, "Electronic interaction of individual slow highly charged ions with TiO_2(110)," Phys. Rev. B **77**, 155427 (2008)

[78] M. Urbassek and P. Sigmund, "A note on evaporation from heated spikes," Appl. Phys. A **35**, 19–25 (1984)

[79] P. Sigmund, "Energy density and time constant of heavy-ion-induced elastic-collision spikes in solids," Appl. Phys. Lett. **25**, 169–171 (1974)

[80] P. Sigmund and M. Szymonski, "Temperature-dependent sputtering of metals and insulators," Appl. Phys. A **33**, 141–152 (1984)

[81] P. Sigmund and C. Claussen, "Sputtering from elastic-collision spikes in heavy-ion-bombarded metals," J. Appl. Phys. **52**, 990–993 (1981)

[82] *CRC Handbook of Chemistry and Physics*, 91st ed., edited by W. M. Haynes (CRC Press/Taylor and Francis, Boca Raton, FL., 2011)

[83] George Philip Pells, "Radiation damage effects in alumina," J. Am. Ceram. Soc. **77**, 368–377 (1994)

[84] E. B. Saloman, "Energy levels and observed spectral lines of xenon, Xe-I through Xe-LIV," J. Phys. Chem. Ref. Data **33**, 765 (2004)

[85] D. Kost, S. Facsko, W. Möller, R. Hellhammer, and N. Stolterfoht, "Channels of potential energy dissipation during multiply charged argon-ion bombardment of copper," Phys. Rev. Lett. **98**, 225503 (2007)

[86] K. Shima, N. Kuno, and M. Yamanouchi, "Systematics of equilibrium charge distributions of ions passing through a carbon foil over the ranges Z=4–92 and e=0.02–6 MeV/u," Phys. Rev. A **40**, 3557–3570 (1989)

[87] W. Brandt, R. Laubert, M. Mourino, and A. Schwarzschild, "Dynamic screening of projectile charges in solids measured by target x-ray emission," Phys. Rev. Lett. **30**, 358–361 (1973)

[88] Z. D. Pešić, Gy. Vikor, S. Atanassova, J. Anton, S. Leontein, M. Björkhage, A. Paál, H. Hanafy, and R. Schuch, "Relaxation of slow highly charged ions hitting thin metallic foils," Phys. Rev. A **75**, 012903 (2007)

[89] T. Schenkel, C. C. Lo, C. D. Weis, A. Schuh, A. Persaud, and J. Bokor, "Critical issues in the formation of quantum computer test structures by ion implantation," Nucl. Instrum. Methods Phys. Res., Sect. B **267**, 2563 – 2566 (2009)

[90] W. Brandt and M. Kitagawa, "Effective stopping-power charges of swift ions in condensed matter," Phys. Rev. B **25**, 5631–5637 (1982)

[91] P. Jespersgaard and J. A. Davies, Can. J. Phys. **45**, 2983 (1967)

[92] R. Herrmann, C. L. Cocke, J. Ullrich, S. Hagmann, M. Stoeckli, and H. Schmidt-Boecking, "Charge-state equilibration length of a highly charged ion inside a carbon solid," Phys. Rev. A **50**, 1435–1444 (1994)

[93] L. Hägg, C. O. Reinhold, and J. Burgdörfer, "Above-surface neutralization of slow highly charged ions in front of ionic crystals," Phys. Rev. A **55**, 2097–2108 (1997)

[94] J. J. Ducrée, F. Casali, and U. Thumm, "Extended classical over-barrier model for collisions of highly charged ions with conducting and insulating surfaces," Phys. Rev. A **57**, 338–350 (1998)

[95] H. Kurz, F. Aumayr, C. Lemell, K. Töglhofer, and HP. Winter, "Neutralization of slow multicharged ions at a clean gold surface: Electron-emission statistics," Phys. Rev. A **48**, 2192–2197 (1993)

[96] H. Kurz, F. Aumayr, C. Lemell, K. Töglhofer, and HP. Winter, "Neutralization of slow multicharged ions at a clean gold surface: Total electron yields," Phys. Rev. A **48**, 2182–2191 (1993)

[97] J. Burgdörfer and F. Meyer, "Image acceleration of multiply charged ions by metallic surfaces," Phys. Rev. A **47**, R20–R22 (1993)

[98] H. Winter, C. Auth, R. Schuch, and E. Beebe, "Image acceleration of highly charged xenon ions in front of a metal surface," Phys. Rev. Lett. **71**, 1939–1942 (1993)

[99] J. Burgdörfer, C. Reinhold, L. Hägg, and F. Meyer, "Interaction of highly charged ions with surfaces," Aust. J. Phys., 527–542(1996)

[100] P. J. Jennings and R. O. Jones, Adv. Phys. **37**, 341–358 (1988)

[101] J. D. Jackson, *Classical Electrodynamics*, 2nd ed. (Wiley, New York, 1975) , Sec 4.3

[102] E. Durand, *Electrostatique: Méthods de Calcul Diélectriques*, Vol. III (Masson et Cie, Paris, 1966) , Chap. 3, Sec. 2

[103] M. Kleefstra and G. C. Herman, "Influence of the image force on the band gap in semiconductors and insulators," J. Appl. Phys. **51**, 4923–4926 (1980)

[104] M. W. Cole, "Electronic surface states of a dielectric film on a metal substrate," Phys. Rev. B **3**, 4418–4422 (1971)

[105] C. B. Harris, N.-H. Ge, R. L. Lingle, J. D. McNeill, and C. M. Wong, "Femtosecond dynamics of electrons on surfaces and at interfaces," Ann. Rev. Phys. Chem. **48**, 711–744 (1997)

[106] J. Gudde, W. Berthold, and U. Hofer, "Dynamics of electronic transfer processes at metal/insulator interfaces," Chem. Rev. **106**, 4261–4280 (2006)

[107] J. D. McNeill, Jr. R. L. Lingle, R. E. Jordan, D. F. Padowitz, and C. B. Harris, "Interfacial quantum well states of Xe and Kr adsorbed on Ag(111)," J. Chem. Phys. **105**, 3883–3891 (1996)

[108] T.-C. Chiang, G. Kaindl, and T. Mandel, "Layer-resolved shifts of photoemission and auger spectra from physisorbed rare-gas multilayers," Phys. Rev. B **33**, 695–711 (1986)

[109] F. Schiller, M. Ruiz-Oses, J. E. Ortega, P. Segovia, J. Martinez-Blanco, B. P. Doyle, V. Perez-Dieste, J. Lobo, N. Neel, R. Berndt, and J. Kroger, "Electronic structure of C_{60} on Au(887)," J. Chem. Phys. **125**, 144719 (2006)

[110] S. L. Ren, Y. Wang, A. M. Rao, E. McRae, J. M. Holden, T. Hager, KaiAn Wang, Wen-Tse Lee, H. F. Ni, J. Selegue, and P. C. Eklund, "Ellipsometric determination of the optical constants of C_{60} (buckminsterfullerene) films," Appl. Phys. Lett. **59**, 2678–2680 (1991)

[111] R. R. Zope, T. Baruah, M. R. Pederson, and B. I. Dunlap, "Static dielectric response of icosahedral fullerenes from c_{60} to c_{2160} characterized by an all-electron density functional theory," Phys. Rev. B **77**, 115452 (2008)

[112] N. W. Ashcroft and N. D. Mermin, *Solid state physics* (Holt, Rinehart and Winston, New York, 1976)

[113] D. Ochs, M. Brause, P. Stracke, S. Krischok, F. Wiegershaus, W. Maus-Friedrichs, V. Kempter, V.E. Puchin, and A.L. Shluger, "The surface electronic structure of stoichiometric and defective LiF surfaces studied with MIES and UPS in combination with ab-initio calculations," Surf. Sci. **383**, 162 – 172 (1997)

[114] S. Pulm, A. Hitzke, J. Gunster, H. Muller, and V. Kempter, "Electron emission from the interaction of He projectiles and UV photons with LiF on W(110)," Radiat. Eff. Def. Solids **128**, 151–162 (1994)

[115] S.T. Ruggiero and J.B. Barner, "Particle-size effects in single-electron tunnel systems," Z. Phys. B **85**, 333–337 (1991)

[116] J. Robertson, "High dielectric constant oxides," Eur. Phys. J.: Appl. Phys. **28**, 265–291 (2004)

[117] M. Terasawa, Z.A. Insepov, T. Sekioka, A.A. Valuev, and T. Mitamura, "Sputtering due to coulomb explosion in highly charged ion bombardment," Nucl. Instrum. Methods Phys. Res., Sect. B **212**, 436 – 441 (2003)

[118] M. A. Briere, T. Schenkel, D. H. Schneider, P. Bauer, and A. Arnau, "Non-equilibrium energy loss for very highly charged ions in insulators," Phys. Scr. **1997**, 324 (1997)

[119] U. Kentsch, H. Tyrroff, G. Zschornack, and W. Möller, "Retention of the potential energy of multiply charged argon ions incident on copper," Phys. Rev. Lett. **87**, 105504 (Aug 2001)

[120] F. Yi and D. A. La Van, "Nanoscale thermal analysis for nanomedicine by nanocalorimetry," Wiley Interdiscip. Rev. Nanomed. Nanobiotechnol. **4**, 31–41 (2012)

[121] P. Sigmund, *Ion Beam Science: Solved and unsolved problems* (Kongelige Danske Videnskabernes Selskab, Kopenhagen, 2007)